Call for a Medium-size mission opportunity in ESA's Science Programme for a launch in 2025 (M4)

THOR

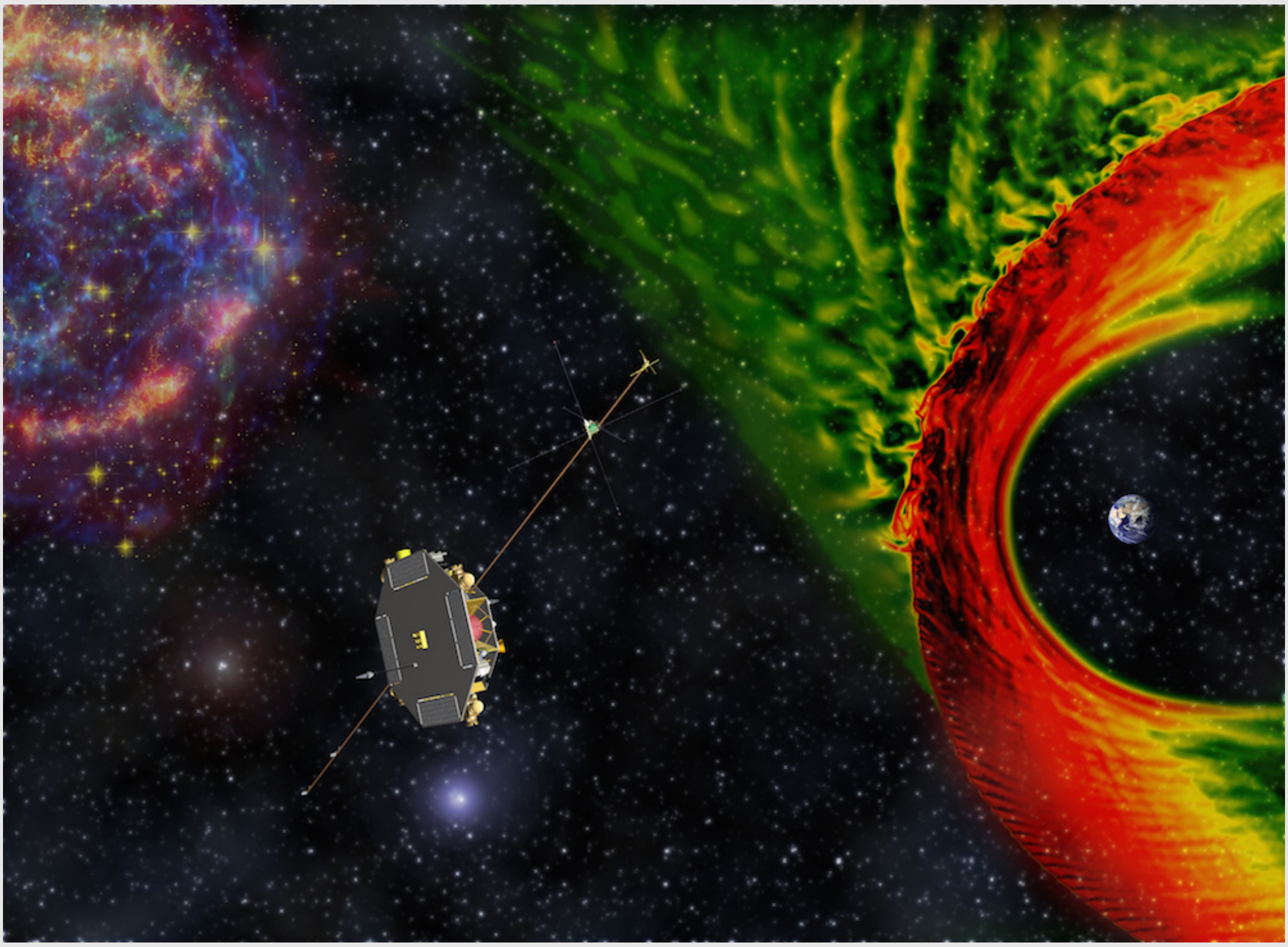

Exploring plasma energization in space turbulence

Lead proposer: A. Vaivads

15 January 2015

Turbulence Heating ObserveR – THOR

Lead Proposer

A. Vaivads (andris@irfu.se), Swedish Institute of Space Physics, Box 537 SE-751 21 Uppsala, Sweden (mob: +46 704 856 457)

The Lead Proposer would be available to support the study activities at the level of at least 20% of his time throughout the study period.

Proposal team

The coordinators of proposal writing: A. Retinò (science), J. Soucek (payload), Y. Khotyaintsev (science management), F. Valentini (numerical simulations), E. Clacey (mission profile).

The full list of the team proposing the THOR[a] mission can be found in Annex A.2

The core hardware team

The core hardware team includes the PIs, Co-PIs and Lead-CoIs of the proposed instruments.

S. Bale (SSL, Univ. Berkeley, USA)
M. Balikhin (Univ. Sheffield, UK)
J. De Keyser (BIRA-ISAB, Brussels, Belgium)
Y. Khotyaintsev (IRF, Uppsala, Sweden)
H. Kucharek (Univ. New Hampshire, USA)
B. Lavraud (IRAP, Toulouse, France)
M. Maksimovic (LESIA, Paris, France)
M. F. Marcucci (INAF-IAPS, Rome, Italy)
R. Nakamura (IWF, Graz, Austria)
Z. Nemecek (Charles Univ., Prague, Czech Republic)
C. Owen (MSSL, London, UK)
J.-L. Pinçon (LPC2E, Orleans, France)
C. J. Pollock (NASA/GSFC, Washington DC, USA)
A. Retinò (LPP, Paris, France)
H. Rothkaehl (SRS, Warsaw, Poland)
F. Sahraoui (LPP, Paris, France)
S. Schwartz (ICL, London, UK)
J. Soucek (IAP/CAS, Prague, Czech Republic)
R. Vainio (Univ. Turku, Turku, Finland)
R. Wimmer-Schweingruber (IEAP, Univ. Kiel, Kiel, Germany)

Acknowledgments

The THOR team acknowledges the support from the Swedish National Space Board and OHB-Sweden in the preparation of the proposal. Contact person of the THOR technical study at OHB-Sweden is E. Clacey (erik.clacey@ohb-sweden.se)

THOR web page

The THOR proposal has a web page http://thor.irfu.se. In addition to a description of the THOR mission there is also a lot of supplementary material, such as detailed instrument data sheets, summaries of data analysis tools and numerical simulation codes, movies of plasma turbulence simulations, etc.

Cover page

Used material: plasma turbulence surrounding a bow shock in a hybrid-Vlasov simulation (M. Palmroth), the CAD drawing of THOR (OHB-Sweden), a false color image of Cassiopeia A (Cas A) using observations from the Hubble and Spitzer telescopes as well as the Chandra X-ray Observatory. Courtesy: Walter Puccio.

[a] In Norse mythology Thor is a hammer-wielding god associated with thunder and lightning, storms and strength, as well as the protection of mankind. Thor brings order out of chaos.

	THOR mission summary
Key scientific objectives	The Universe is permeated by hot, turbulent magnetized plasmas. They are found in active galactic nuclei, supernova remnants, the intergalactic and interstellar medium, the solar corona, the solar wind, and the Earth's magnetosphere, just to mention a few. Our knowledge and understanding of the Universe is largely based on measurements of electromagnetic radiation such as light or X-rays which originate, in most cases, in hot plasmas. We believe that energy dissipation of turbulent fluctuations in plasmas play a key role in plasma heating and energization. It is remarkable that we still do not understand the underlying physical mechanisms! Understanding these mechanisms is the unique mission of THOR. THOR will address the fundamental science theme ***Turbulent energy dissipation and particle energization*** which ties in with ESA's Cosmic Vision. In particular, THOR will address the following specific science questions: • How is plasma heated and particles accelerated? • How is the dissipated energy partitioned? • How does dissipation operate in different regimes of turbulence?
Spacecraft	Sun-pointing, allowing high quality electric field and particle measurements. Slow spinner 2 rpm, to get high angular resolution particle data. Payload mass 164 kg, total dry mass 637 kg, total wet mass 949 kg. Bipropellant propulsion system. Active spacecraft potential control to improve plasma and field measurements. In comparison to earlier/upcoming missions key major improvements include: • accuracy/sensitivity of electric and magnetic field measurements, • temporal resolution of mass resolved ions (H^+, He^{++}), • temporal/angular/energy resolution of electrons.
Payload	MAG fluxgate magnetometer — B field, 0–32 Hz SCM search-coil magnetometer — B field, 1 Hz–200 kHz EFI electric field instrument — E field, 2D 0–200 kHz, 3D 0.1–200 kHz FWP field wave processor — E, B time series and spectral products ESA electron spectrometer — electron 3D distr. function CSW cold solar wind analyser — cold solar wind ion 3D distr. function IMS ion mass spectrum analyser — 3D distr. functions of H^+, He^{++}, He^+, O^+ PPU particle processing unit — ESA, CSW, IMS data products FAR Faraday cup — cold solar wind ion moments EPE energetic particle analyzer — energetic electrons and ions 3D distr. function
Mission	3 year nominal mission, extended mission possible. 1st year, 4x16 R_E, focus on bow shock and magnetosheath. 2nd year, 4x26 R_E, focus on solar wind and foreshock. 3rd year, 14x60 R_E, focus on undisturbed solar wind and interplanetary shocks. Orbit parameters can be adjusted based on the expected solar cycle development.
Radiation	34 krad for 5 mm and 137 krad for 3 mm Al shielding.
Responsibilities	ESA: spacecraft manufacturing, launch and operations; data archiving and distribution. PI teams: science payload provision, operations, data processing, calibration and analysis.
Communications	Low-latitude ESA stations Perth and Kourou, 15m X-band antenna. Average bitrate 345 kbps 1st year and 155 kbps 2nd year, 25 kbps 3rd year
Science operations	Survey data downloaded from the whole period. ~2 h of Burst data per orbit downloaded through selective downlink. Data archiving and distribution at ESA. Open Data policy from 6 month into the nominal operations.

1 Executive Summary

During the past century of exploration of the Universe, we have learned that normal ***matter in the Universe is primarily in the plasma state***. It is the hot dilute plasma (ionized gas) between galaxies and galaxy clusters, and not stars, that dominates baryonic matter. Furthermore most of the baryonic matter in the Universe is not detectable in the visible light, but instead becomes apparent only in X-rays that are generated by hot plasmas. Hot dilute plasma can also be found within galaxies, such as interstellar medium, outer atmospheres and stellar winds of stars, coronas of accretions disks. These hot plasmas may well be heated by the dissipation of the turbulence driven by large scale shear motions, shock waves, jets, and other large-scale instabilities and processes. ***Astrophysical plasmas are turbulent, and dissipation of turbulent fluctuations leads to continuous plasma heating and to acceleration of charged particles.*** Understanding basic plasma processes of plasma heating and energization in turbulent magnetized plasmas is of fundamental importance if we are ever to understand the evolution of the Universe.

Turbulent fluctuations in astrophysical plasmas reach up to scales as large as stars, bubbles or "clouds" blown out by stellar winds, or even entire galaxies. However, most of the irreversible dissipation of energy within turbulent fluctuations occurs at the very small scales – *kinetic scales*, where the plasma no longer behaves as a fluid and the properties of individual plasma species (electrons, protons, and other ions) become important. The efficiency of plasma heating, the partition of energy transferred to different particle species, the acceleration of particles to high energies—all are strongly governed by kinetic processes that determine how the turbulent electromagnetic fluctuations dissipate. Thus, plasma processes at kinetic scales will directly affect the large-scale properties of plasma.

Turbulence Heating ObserveR – THOR is the first mission ever flown in space dedicated to plasma turbulence. It will explore the kinetic plasma processes that determine the fundamental behavior of the majority of baryonic matter in the universe. THOR will lead to an understanding of the basic plasma heating and particle energization processes, of their efficiency for different plasma species and of their relative importance in different turbulent regimes. THOR will provide closure of these fundamental questions by making detailed *in situ* measurements of the closest available dilute and turbulent magnetized plasmas at unprecedented temporal and spatial resolution. THOR focuses on particular regions—pristine solar wind, Earth's bow shock and interplanetary shocks, and compressed solar wind regions downstream of shocks. These regions are selected because of their differing turbulent fluctuation characteristics, and reflect similar astrophysical environments. In addition, both spatial and temporal characteristic plasma scales in the key science regions are sufficiently large, so that the particle instruments are able to resolve the kinetic scales. *The THOR spacecraft will carry, for the first time, a comprehensive payload tailored to explore plasma energization in turbulence*, with both fields and particle instrumentation that will allow the simultaneous resolution of both the turbulent fluctuations and the signature of the resultant plasma energization. The payload consists of mature instruments with recent flight heritage. THOR will also open new paths by providing measurements that go beyond our current theoretical expectations, thus allowing the exploration of new physics and challenging our theories.

THOR science directly addresses the Cosmic Vision question "How does the Solar System work?" by studying basic processes occurring "From the Sun to the edge of the Solar System". By quantifying the fundamental processes involved, the advances made by the THOR mission will extend beyond the Solar System to plasmas elsewhere in the Universe. ***THOR will provide understanding of fundamental plasma processes with applications to very different astrophysical, solar system and laboratory plasma environments***. Due to studies involving a variety of space missions, including Cluster and THEMIS (and in the near future, missions such as Magnetospheric Multiscale, Solar Orbiter and Solar Probe Plus) we now understand many aspects of plasma turbulence, such as 3D properties of plasma turbulence owing to multi-spacecraft observations. However, how the turbulence dissipates and heats the surrounding medium and energizes particles is not at all well understood. That is the unique mission of THOR. THOR will provide the understanding of fundamental processes underlying the measurements of exciting future missions such as the L2 X-ray astronomy mission with science theme: "The Hot and Energetic Universe".

Our local space environment, near Earth's space, provide a unique opportunity for *in situ* study plasma turbulence under a wide range of physical parameters that reflect conditions in other astrophysical locales. The plasma turbulence community is one of the largest cross-disciplinary science communities. Carefully designed laboratory plasma experiments, as well as increasingly sophisticated numerical simulations will complement space experiments such as we propose to conduct with THOR. The totality of those efforts will lead to a paradigm shift in our understanding of turbulence and energization mechanisms in astrophysical plasmas and will open new horizons for studying the fundamental physics of visible matter.

2 Science case

2.1 Introduction

The turbulent plasma Universe Plasma processes are at work everywhere, from radio galaxy jets and supernova explosions (Figure 1) to the solar corona and circumplanetary space. It is for this reason that H. Alfvén coined the term *Plasma universe*[1]. The information we have on distant astrophysical plasmas is obtained from the radiation they emit and we remotely observe. Therefore, it is of crucial importance to understand plasma energization mechanisms that are behind such emissions. *Astrophysical plasmas are often in a turbulent state*[2] and major plasma energization is related to the dissipation of turbulent fluctuations. Examples of turbulent dissipation can be found in galaxies[3,4], stellar interiors [5,6],interplanetary[7–9] and interstellar [10,11] media and planetary magnetospheres [12–14]. Shocks are some of the most spectacular, visually-striking phenomena in the plasma Universe and are responsible for the acceleration of copious amounts of charged particles up to energies 10^{18} eV and maybe even as high as 10^{20} eV. Turbulence plays also a major role for particle acceleration at shocks[15]. Turbulent energy dissipation is also very important in laboratory plasmas, e.g. in fusion devices, where turbulence has detrimental effects on the confinement of the plasma.

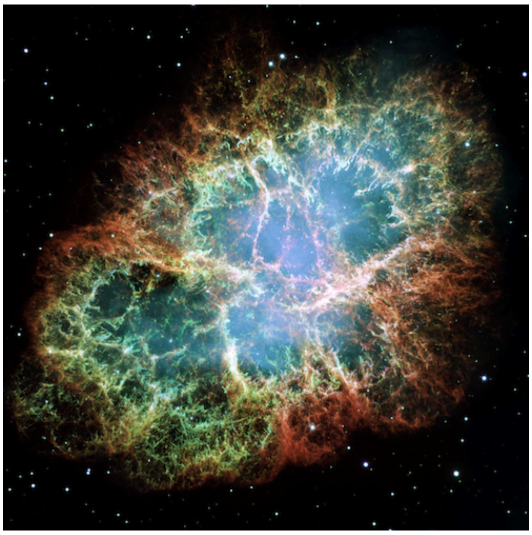

Figure 1: *A classic example of turbulence in an astrophysical object: the highly turbulent supernova remnant Crab nebula. Credit: NASA, ESA, J. Hester, A. Loll (ASU) Acknowledgement: Davide De Martin (Skyfactory).*

Despite of their importance, remote observations of turbulence and plasma energization in astrophysical plasmas lack spatial resolution and can only provide integrated, often model-dependent measurements. Solar observations have considerably increased their resolution in the last decade owing to data from Soho, Hinode and SDO missions. However, they are still not adequate for the detailed

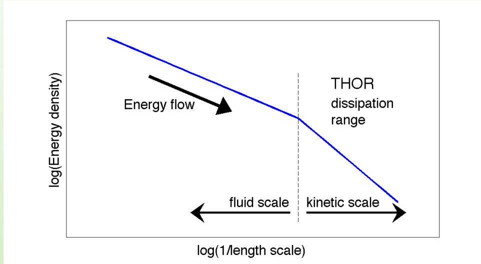

Energy injected at fluid scales in turbulent plasma cascades to kinetic scales where it is dissipated.

study of energy dissipation mechanisms. Measurements in laboratory plasmas have also improved recently in terms of diagnostic, see for example the MRX[16] or TORPEX[17] experiments, but the boundary conditions imposed by laboratory setup are often a severe limiting factor. Due to the inherent complexity of the underlying physics, understanding such mechanisms in depth from an experimental point of view requires direct measurements of plasma and electromagnetic fields. *In situ* spacecraft observations in the Solar System can provide such measurements, and the synergy between *in situ* and remote observations, e.g. from telescopes, can significatively help advancing our understanding of the Plasma Universe.

Turbulent dissipation at kinetic scales In space plasma turbulence, energy is injected in the system at large scales, often referred to as fluid scales, and it is then transferred to smaller and smaller scales by non-linear interactions which generate a variety of different turbulent fluctuations. This process is known as *turbulent energy cascade*. Energy dissipation is negligible at fluid scales while becomes important at *kinetic scales*, in the so-called *dissipation range*, where the typical scales of turbulent fluctuations become comparable with those of particles, e.g. gyroradii. Kinetic scales are very small compared to the typical size of many astrophysical systems; as an example, ion or electron gyroradii in the near-Earth space are about few hundreds of kilometers or few kilometers, respectively. In the dissipation range, energy of turbulent fluctuations is transferred into heating and acceleration of charged particles, which modifies the shape of the particle distribution functions. At lower energies, dissipation corresponds to heating, namely the increase in the temperature of the thermal (core) population. At higher energies (up to several times the thermal energy), a suprathermal tail is typically formed, while at even higher energies (up to many tens of thermal energies), a more energetic population tail is found.

The near-Earth space Most astrophysical plasmas are collisionless at kinetic scales, so that plasma physics therein is very similar to the one in solar system plasmas. Yet remote observations of kinetic

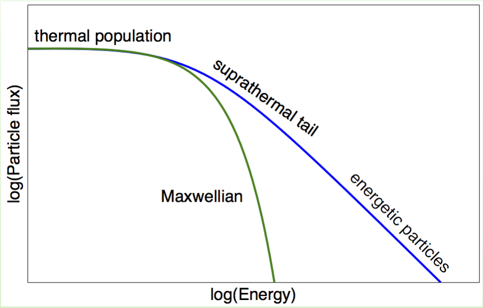

Turbulent dissipation leads to plasma heating and/or acceleration of particles to high energies, forming suprathermal and energetic tails in their distribution function.

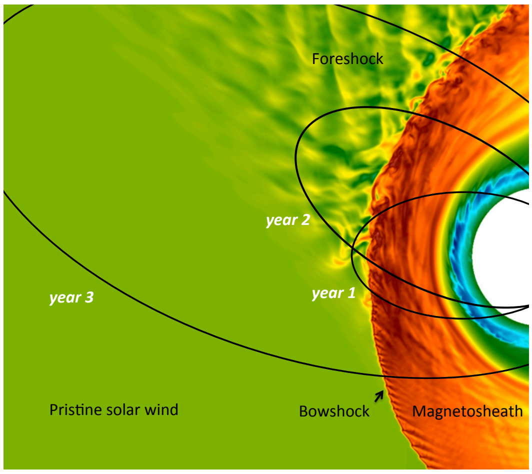

Figure 2: *Cartoon of near-Earth space based on Vlasiator numerical simulations. The coloring shows plasma density. Key turbulent regions are shown: pristine solar wind, shock and magnetosheath. THOR orbits over the three-years nominal phase are indicated (not in scale).*

scales, even for the case of high-resolution imaging of the Sun, are not accessible. In laboratory plasmas, kinetic scales are typically of the order of few centimeters or less. Manufacturing advanced plasma sensors capable of resolving such small scales is technically very challenging. The near-Earth space (see Figure 2) is a privileged laboratory for studying turbulent energy dissipation at kinetic scales because of high resolution *in situ* measurements can be performed there and transmitted to ground with high cadence. Furthermore, near-Earth turbulent regions offer the possibility of studying many different types of turbulent fluctuations over an extremely broad range of scales. Due to similarities with other solar, astrophysical and laboratory plasma regimes, see Figure 3, many of the results obtained in near-Earth space can be scaled to other plasma environments. One very important example of turbulent environment in near-Earth space is the solar wind, where the complex dynamics of the Sun's atmosphere provides the initial energy at large scales that drives the turbulence in the interplanetary space, followed by dissipation at kinetic scales. Another important example are turbulent shock regions e.g. the terrestrial bow-shock where locally generated turbulent fluctuations plays a major role for particle acceleration.

Previous and current space missions in the near-Earth space provide a large amount of *in situ* measurements, that have allowed impressive advances in characterizing turbulence at fluid scales. It was found for the the pristine solar wind that a fluid description can be used for the large scale (low frequency) physics of turbulence[7,18]. On the other hand, most of energy dissipation and particle energization is expected to occur at kinetic scales [19–22]. Yet the dissipation mechanisms at such scales are still poorly understood from an experimental point if view. Understanding such mechanisms requires *in situ* high-resolution and high-sensitivity measurements at kinetic scales in different near-Earth turbulent regions. THOR would be the first satellite ever tailored to perform such measurements.

Comparison to other missions. Many past and current spacecraft missions have studied near-

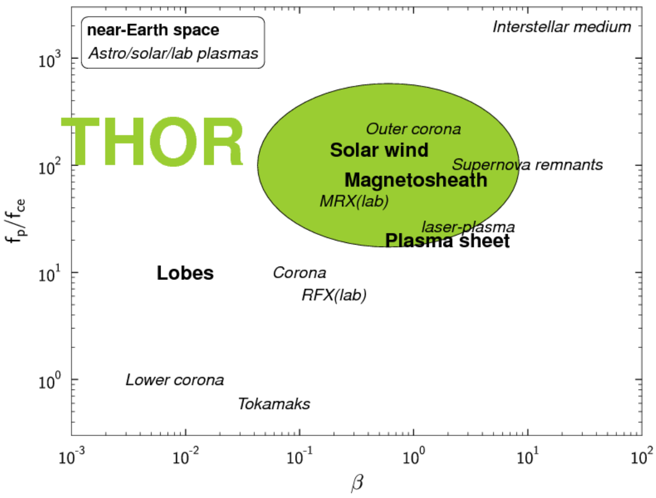

Figure 3: *Different plasma environments. Many of the astrophysical and laboratory plasma environments are very similar to near-Earth space when compared in non-dimensional parameter space.*

Earth space plasmas. None of these missions, however, has been or will be capable of reaching the sensitivity and accuracy of electric and magnetic field measurements and the high temporal, angular and energy resolutions of particle distribution functions that THOR will provide. Such measurements are required to study and fully understand turbulent energy dissipation and plasma energization at kinetic scales. A detailed comparison with current and upcoming missions in term of fulfilling THOR science requirements is shown in Table 5. As an example, the upcoming NASA Magnetospheric MultiScale mission (MMS) is tailored to study the magnetic reconnection process at large scale boundaries, such as the terrestrial magnetopause and magnetotail. MMS will also make measurements in near-Earth turbulent regions such as the solar wind and the magnetosheath, but it will have much less accurate electric and less sensitive magnetic field measurements. Furthermore, MMS particle detectors are not tailored to measure solar wind plasma and will not be able to provide plasma composition at high temporal resolution, e.g. for alpha particles that are very important for studying turbulent energization. MMS orbits are also not tailored for solar wind studies and the time spent by MMS in the solar wind will be much shorter than THOR. Future missions ESA/Solar Orbiter (SO) and NASA/Solar Probe Plus (SPP) will make measurements in the solar wind and address turbulence as one of their many goals. Yet the *in situ* instrumentation onboard such spacecraft is not tailored for studying kinetic scales, as they are lacking either sensitivity/accuracy or time resolution of measurements. Furthermore, due to their large distance from Earth, the volume of high resolution data that both SO and SPP could transmit is very limited compared to THOR. Such large data volume are required to provide meaningful statistical description of turbulent energy dissipation processes. On the other hand, due to the different orbits of THOR and both SO and SPP, the synergy between all these missions would allow to compare and address the important question of turbulence evolution as a distance from the Sun. Finally, based on mission concepts that have been in the proposal or planning stage, such as Cross-Scale[23] and EidoSCOPE[24], it has become clear and compelling that future missions need to improve sensitivity and accuracy of the electric and magnetic field measurements, as well as the resolution of particle measurements, to resolve kinetic scale plasma processes.

2.2 Dissipation mechanisms

Science question I How is plasma heated and particles accelerated by turbulent fluctuations at kinetic scales?

Most of the energy dissipation occurring in collisionless plasmas, such as those permeating the solar system and many astrophysical environments, is expected to occur at kinetic scales, that is, at scales comparable to particle gyroradii and below. A variety of fluctuations operate at kinetic scales and are associated to different heating and acceleration mechanisms as indicated by numerical simulations[25–30] and illustrated in Figure 5. Figure 4 shows an example from simulations where large-scale shear in plasma flows drive turbulent energy cascade down to kinetic scales. Electrons are accelerated to suprathermal energies at those scales by turbulent fluctuations. Yet only few *in situ* observations of dissipation and associated energization at kinetic scales are available in near-Earth plasmas[20,21,31,32], due to the lack of dedicated measurements. Consequently, the exact contribution of the different mechanisms to the overall energy dissipation is poorly known. THOR will explore all these dissipation mechanisms with the best resolution of particle and field measurements ever.

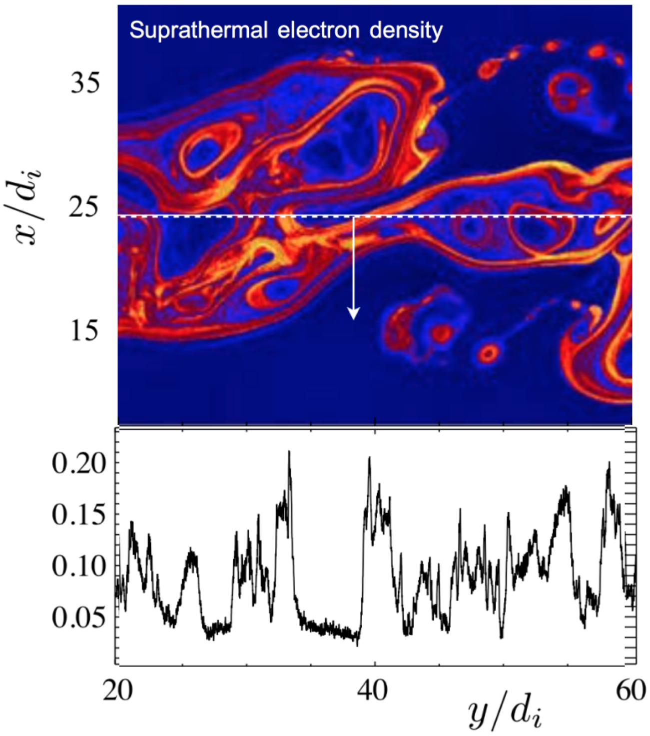

Figure 4: *Top: Two-dimensional particle-in-cell simulation of shear-flow turbulence showing electron acceleration in small-scale structures. The density of suprathermal electrons is color coded. Bottom: horizontal cut showing density of suprathermal electrons as may be seen by a virtual spacecraft*[29].

2.2.1 Uniform dissipation

Dissipation can occur at scales over large plasma volumes and operate over long timescales in regions permeated by different kind of waves, see Figure 5. Such type of dissipation is sometimes referred to as *dissipation by wave damping*. Several collisionless dissipation mechanisms related to wave damping are proposed, e.g. linear Landau and cyclotron damping[21,33–35], stochastic heating [25], trapping and heating in large-amplitude waves [36–38] and nonlinear Landau damping resulting in the generation of phase-space holes [39,40] . A number of different wave modes associated to these mechanisms, such as kinetic Alfvén waves (KAWs), fast and slow magnetosonic waves, whistler waves and electrostatic waves are at work in kinetic range and the dissipation of such fluctuations can contribute to plasma heating and particle acceleration of both ions and electrons.

Wave modes Measurable parameters such as the ratio between electric and magnetic field amplitudes, the anisotropy and polarization of field fluctuations can be used to distinguish between the different wave modes and thus to investigate the dissipation mechanisms, provided that both Doppler shift and Lorentz transformation are taken into account[41]. For example, whistler waves have been identified based on the right-hand polarization of the fluctuations[42]. KAWs have been identified based on the ratio between electric and magnetic field[43], combined with the mag-

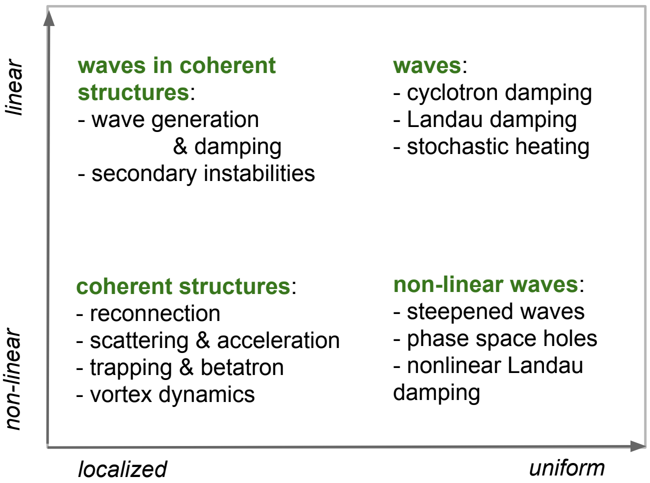

Figure 5: *Diagram illustrates dissipation mechanisms depending on the spatial uniformity and linearity of turbulent fluctuations.*

netic compressibility [41]. Yet oblique whistlers and KAWs are both right-hand polarized and their magnetic compressibility is not too different. An efficient way to distinguish between them is to measure the relative level of density and magnetic fluctuations $\delta n/\delta B$[44,45]. There are however only few observations showing an increase of compressible fluctuations in the dissipation range[41,44,46]. Such wave mode identification is limited by the low sensitivity of electric and magnetic field measurements as well as the low time resolution measurements of density at kinetic scales (**RS-2** , **RS-4**, **RS-6**).

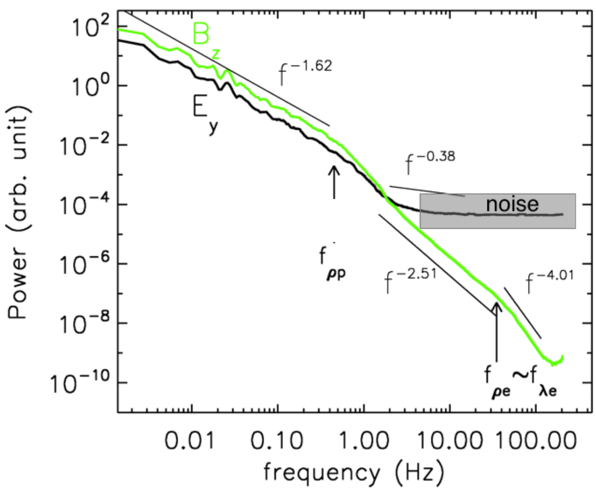

Figure 6: *(Top) Energy spectra of electric field (black) and magnetic field fluctuations (green) in the solar wind upstream of the terrestrial shock measured by the Cluster spacecraft[21]. The shaded part of the electric field spectrum is not resolved, due to instrumental noise.*

Spectral properties The energy spectrum of turbulent fluctuations usually exhibits specific scaling. The form of this scaling in the kinetic range has been used to address the underlying physics of the dissipation mechanisms. As an example, Figure 6 shows electric and magnetic field spectra measured by Cluster spacecraft in the solar wind upstream of the terrestrial shock. The figure shows that at fluid scales (low frequencies) both electric and magnetic spectra are reminiscent of the typical Kolmogorov power law spectrum, with spectral indexes slightly dependent on plasma conditions, being close to $-5/3$ or $-3/2$[9,21,43,47]. No significant dissipation is occurring there while turbulent energy is being transferred to smaller and smaller scales at a given rate[48–50]. At higher frequencies, a spectral break is observed near proton scales strongly suggesting an abrupt change in the physical processes occurring in that range[9,19–21,51]. A different power-law spectrum is found below proton scales, indicating the presence of a nonlinear cascade which could include dissipative effects. Such steepening is in agreement with numerical simulations of KAW turbulence[35], which are also reproduced in other Cluster observations[9] showing the very same scaling $\sim k_\perp^{-2.8}$ as in the numerical simulation, see Figure 7, bottom panel. At even smaller scales, approaching the electron range, the spectrum shows a faster decay consistent with a steeper power law[21] or exponential decay[9,22,52], which could be associated to different dissipation mechanisms. Such spectral scalings at kinetic scales are consistent with dissipation of KAWs via Landau damping[9,21,52,53], in agreement with simulations[35,54]. Other observations of KAWs suggest instead energization through stochastic heating[25]. Recent Cluster observations, however, also indicate the presence of right-hand polarized whistler waves around electron scales[42]. When such waves are observed, turbulent spectra show spectral peaks rather than steepening of the spectrum. Most of such spectral measurements in the solar wind have been however strongly limited by the low sensitivity of electric and magnetic field instruments compared to the level of fluctuations there (**RS-2**). Other important spectral properties that can be used to distinguish dissipation mechanisms at kinetic scales are electric and magnetic field anisotropies, velocity anisotropies and magnetic helicity[34,35,55,56] for which it is very important to measure the relative scaling in the parallel and perpendicular directions $(k_\parallel, k_\perp)$ down to electron scales. Spectral anisotropy of the magnetic field at kinetic scales has been observed in the undisturbed solar wind[53,57–59] as well as in the magnetosheath[60,61], yet measurements at those scales were performed very close to the noise level of magnetometers so that uncertainties are high, in particular close to electron scales (**RS-2**). Current magnetic field sensitivity allows to cover those scales only if the turbulent fluctuations are of sufficiently high amplitude[62]. Magnetic helicity spectra have also been used[63–65] to e.g. provide evidence of Alfvén-cyclotron waves and suggest cyclotron mechanism for plasma heating in the solar wind[63]. The spectral anisotropy of electric field turbulence remains on the other hand almost fully unexplored due to the lack of accurate electric field measurements so far[60].

At frequencies higher than those corresponding to the ion kinetic scale (above 1 Hz in Figure 6) the electric spectrum flattens and it becomes dominated by noise (**RS-2**). Moreover, at even smaller scales (higher frequencies) plasma waves become more and more electrostatic, which emphasizes even more the need to measure accurately the electric field.

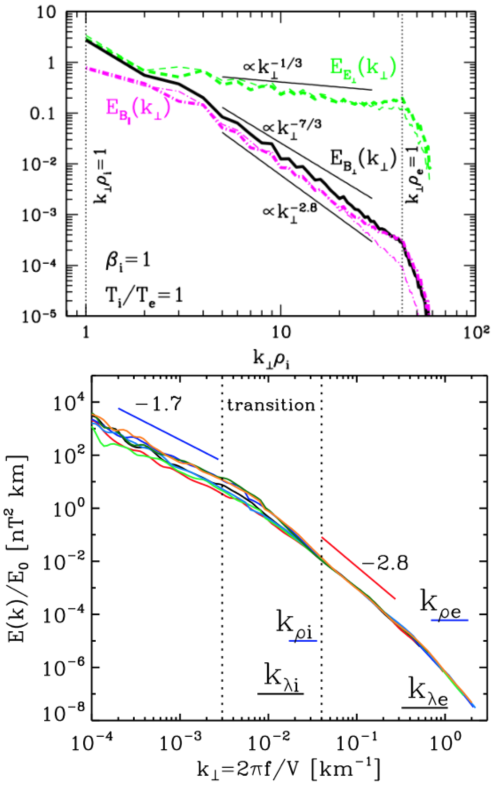

Figure 7: *Upper panel: Development of scaling and variance anisotropy of turbulence in kinetic range as seen in gyrokinetic simulations* [35]. *Lower panel: several solar wind turbulent spectra for different plasma conditions; the range of ion and electron scales is shown* [9]

Effects on plasma All the observations discussed above could not fully identify dissipation mechanisms because the connection between observed wave modes and dissipation mechanisms was based almost exclusively on electric and magnetic field data and on the comparison with numerical simulations. Evidence of heating and acceleration from particle measurements during wave damping at kinetic scales is scarce[51,66] and this aspect is basically unexplored from observational point of view due to the lack of high temporal, angular and energy resolution measurements of particle distribution functions, while most of the information comes from numerical simulations. Wave damping dissipation of different wave modes results in different modifications of particle distribution functions, e.g. formation of anisotropies, beams and high-energy tails. Recent Hybrid Vlasov-Maxwell numerical simulations of solar wind turbulence[28,67,68] have shown the behavior of ion distribution functions around the ion scales. When the turbulent activity reaches its maximum, the shape of the three-dimensional velocity distribution f shows evident non-Maxwellian features, such as temperature anisotropy along or across the local magnetic field and particle beams mainly aligned to the local magnetic field (Figure 8). Landau Damping, cyclotron resonance are expected to produce heating in parallel, perpendicular directions respectively. Such features are the smoking gun of wave-particle interaction processes and wave damping dissipation mechanisms and indicate that measuring ion distributions with high angular and energy resolution is crucial to understand particle heating and acceleration. Moreover, resolving the sharp velocity gradients of f generated along the turbulent cascade is crucial in establishing whether or not plasma collisionality can be locally enhanced in presence of fine velocity structures, this being highly relevant for the plasma heating problem. (**RS-8**, **RS-10**). Particle-in-cell simulations have also shown the development of large electron parallel temperature anisotropy, and, possibly, the formation of electron beams[27,69]. Such large anisotropy is localized within regions that extend less than 0.1 ion gyroradii, and are smoothed out when averages of particle measurements are done over larger regions, see Figure 30. Therefore, it is crucial to characterize electron distribution functions with high temporal, energy and angular resolution (**RS-9**, **RS-10**). THOR will perform such measurements and will allow assessing quantitatively the effect of wave damping on plasma heating and acceleration.

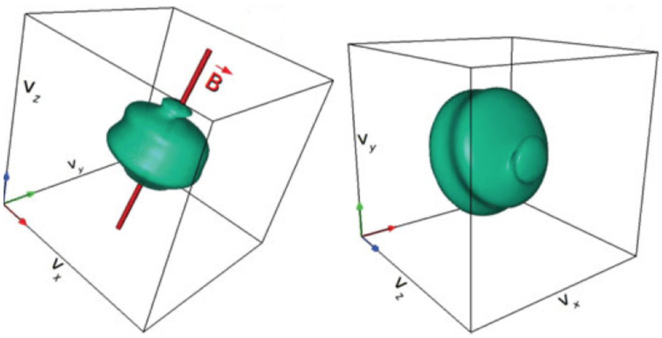

Figure 8: *Proton velocity distribution function, taken at a single point in Vlasov turbulence. The distribution is strongly non-Maxwellian, manifesting anisotropy, resonances and the production of a plasma beam, aligned with the local magnetic field (red tube).*

2.2.2 Localized dissipation

Dissipation can occur at kinetic scales within coherent structures that are localized both in space and time and have scales comparable to particle gyroradii, such as thin current sheets, magnetic islands, isolated flux tubes and small-scale vortices [70–72]. Such structure are usually associated to strong electric currents (Figure 9a) where non-Maxwellian features of particle distribution functions are also observed (Figure 9b), and they are sites of strong dissipation and particle energization. Figure 4 shows an example of electron acceleration in thin current sheets and magnetic islands forming on scales from ion to electron scales within turbulence. Localized dissipation occurring within coherent structures is often referred to as *intermittent*.

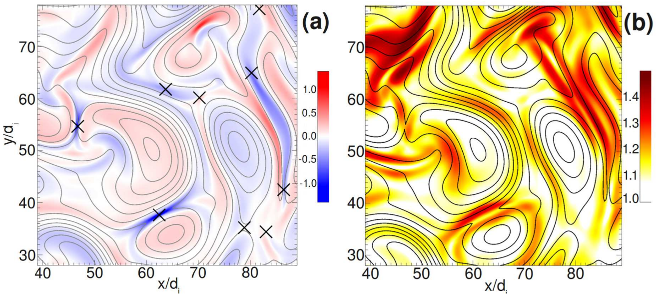

Figure 9: *(a) Shaded contours of current density j_z and magnetic potential a_z (isolines) in the $x-y$ plane. Possible reconnection sites are indicated by crosses (b) shaded contour of the proton temperature anisotropy together with the in plane magnetic field lines (black). The comparison between these two plots indicates that kinetic deformations of the particle velocity distributions are concentrated around coherent structures that are located near the peaks of j_z.*

Reconnecting current sheets One major mechanism of intermittent dissipation is magnetic reconnection. Reconnection is a fundamental plasma physics phenomenon and one of the major causes of energy dissipation and transport in astrophysical plasmas [73]. In turbulence, reconnection occurs in a large number of small-scale current sheets that form between coherent magnetic structures as natural consequence of turbulence development, as indicated by many numerical simulations [34,70,74–76], see Figure 9, left panel. Strong plasma heating and particle acceleration at scales comparable to the kinetic scales of reconnecting current sheets are expected from numerical simulations [77–80]. Recent Cluster observations revealed, for the first time, *in situ* evidence of reconnection in ion-scale current sheets forming in the solar wind downstream of the terrestrial quasi-parallel shock [20,31], see Figure 10. Small-scale reconnection events have also been observed in the undisturbed solar wind [32,81] and within coronal mass ejections [82]. Such observations indicated the importance of turbulent reconnection as energy dissipation mechanism [20,83].

Yet, besides these few studies, there has been no systematic observational study of how efficient is reconnection for plasma heating and particle acceleration due to the limited quality of electric field and particle measurements on available spacecraft. High-quality electric field measurements are necessary to estimate the typically small reconnection electric field that is the key parameter of the reconnection process (rate) and it is used for estimation the dissipation rate through $\mathbf{E}\cdot\mathbf{J}$ [20,31] (**RS-3**,**RS-6**, **RS-7**). Heating of electrons in thin reconnecting current sheets has been demonstrated for one case downstream of the terrestrial shock, also suggesting the acceleration of suprathermal ions, see Figure 10. No such observations have been reported so far for the case of the undisturbed solar wind and of other turbulent environments. High temporal resolution particle measurements are required to quantitatively assess heating and acceleration mechanisms in thin current sheets (**RS-6**, **RS-7**, **RS-8**, **RS-9**, **RS-10**). THOR will provide such measurements and quantitatively address the question of dissipation during turbulent reconnection.

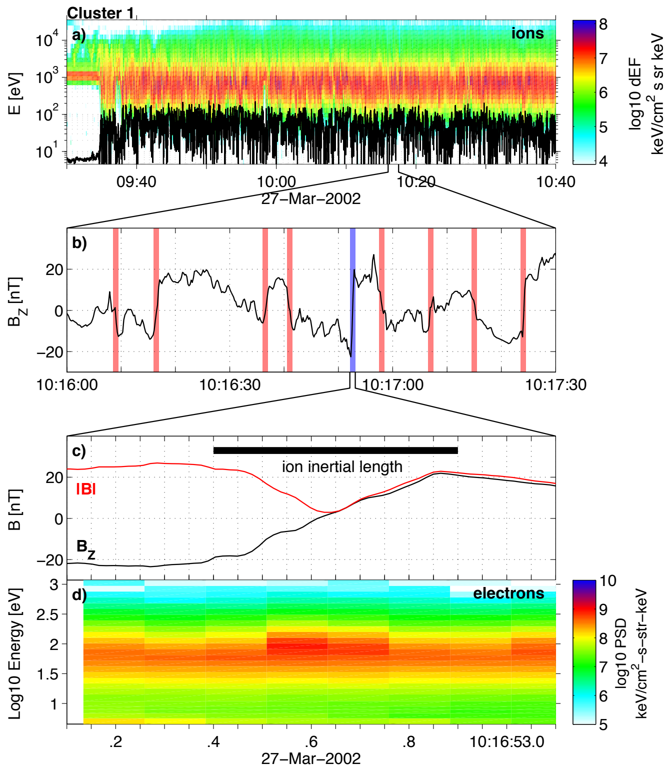

Figure 10: *Reconnecting current sheets in magnetosheath turbulence [31].*

Shocklets and vortices Important intermittent dissipation at kinetic scales can also occur due to mechanisms other than reconnection, such as interaction with shock-like structures (often referred to as shocklets) and non-linear processes within vortex-like structures. One example where shocklet formation on kinetic scales is of key importance for plasma heating and particle acceleration is the quasi-parallel shock [38,84,85], see Figure 11. Understanding the intricate feedback of ion dynamics within shocklets on the resulting variability in the shock structure is required to find a definitive solution to the *injection problem*, the formation of a seed population of suprathermal ions on which Fermi acceleration can act to accelerate particles to very high energies [86]. Another example, vortex formation, is very pronounced in plasma environments exhibiting a velocity shear. Numerical simulations show that, as shear-flow instabilities set in, turbulent vortex formation and secondary instabilities develop down to the smallest kinetic scales [29], see Figure 4. Such simulations show that plasma heating and particle acceleration occur at those scales[29,87]. Only very few *in situ* observations of vortex structures exist[88–90], however plasma measurement resolution has not been sufficient to study plasma heating and particle acceleration within those vortices at kinetic scales (**RS-6**, **RS-7**, **RS-8**, **RS-9**, **RS-10**).

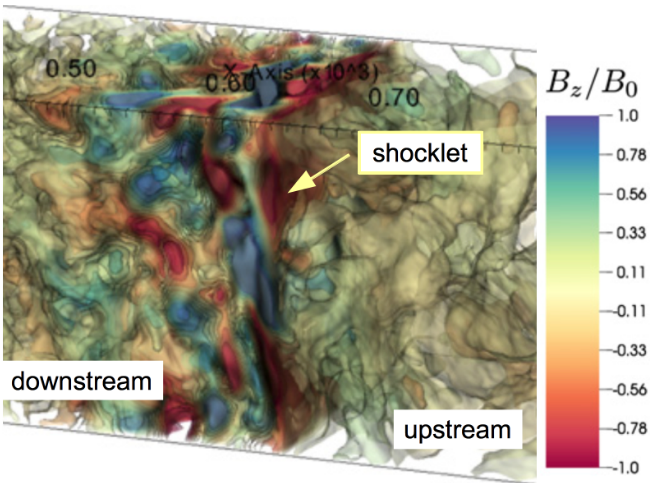

Figure 11: *Three-dimensional particle-in-cell simulation of quasi-parallel shock turbulence showing the presence of shocklets at kinetic scales* [91].

Wave-particle interaction within coherent structures Numerical simulations indicate that wave-particle interaction may also occur within coherent structures, e.g. current sheets may sometimes be dissipated through Landau damping[30]. This suggests that both coherent structures and wave-particle interaction within the structures themselves may be responsible for localized dissipation. Yet, no *in situ* observations discerning between these two possibilities have been reported due to limitations in particle measurements (**RS-6**, **RS-7**, **RS-8**, **RS-9**, **RS-10**).

2.3 Energy partition

Science question II: How is the dissipated energy partitioned between heating and acceleration of electrons, protons and heavier ions?

The second science question that THOR will answer is where the energy dissipated by major turbulent fluctuations at kinetic scales is channeled in terms of both energy ranges and particle species. Answering this question is very important for understanding the behavior of many astrophysical plasmas. As an example, equipartition of high-energy cosmic rays with the thermal gas in clusters of galaxies is invoked to explain observations of nonthermal radiation in a wide range of wavelengths[92]. Remote observations in the solar corona suggest that the magnetic energy dissipated during flares into the acceleration of high-energy particles is higher than that going into plasma heating[93,94]. On the other hand an important fraction of magnetic energy dissipated in the corona is expected to go into thermal plasma and account for coronal heating. Remote observations also indicate that the energy spectrum of cosmic rays is dominated by ions, 99% of which are protons and alpha particles. Assessing energy partition between energy ranges and species from *in situ* measurements is crucial to understand how solar system plasma energization works and can help understanding the energization mechanisms lying behind the electromagnetic radiation measured from distant astrophysical objects during key phenomena.

Many signatures exist in the turbulent solar wind and shock regions indicating that plasma is continuously being energized. As an example solar wind observations of ion temperature over many astronomical units are not consistent with an adiabatic behavior[95,96] indicating that solar wind plasma is being continuously locally heated , see Figure 12. Yet, solar wind electrons and protons show different temperatures e.g. electrons are cooler than protons in the fast wind while hotter in the slow wind[97] suggesting that different heating mechanisms are at work for electrons and ions respectively. Furthermore heavier ions (alpha particules in particular) seem to be preferentially heated with respect to protons, the temperature ratio being more than mass proportional[98]. Non-maxwellian features of distribution functions such as beams and energetic tails are also found both in the solar wind and in planetary, interplanetary and termination shock regions[97,99–102], indicating that both heating and acceleration are at work. Most of these signatures have been provided by large-scale observations of turbulent fluctuations and particle distribution functions, while major turbulent dissipation is expected at kinetic scales. Yet high-resolution coordinated field and particle measurements in solar wind and shock regions resolving kinetic scales are scarce. THOR mission will provide such measurements and allow to resolve energy partition in turbulent plasma dissipation.

2.3.1 Partition among species

There are very few *in situ* measurements at kinetic scales in the solar wind and shock regions assessing how energy is distributed among plasma species for different turbulent dissipation mechanisms. Available observations are basically based on magnetic and electric field measurements in combination with expectations from theory and simulations[21,25,32] while observations of particle distributions are scarce[31]. Most of the information comes from numerical simulations e.g. gyrokinetic[55], hybrid[103], particle-in-cell[27,104,105] and Vlasov codes[106,107]. All these numerical simulations are able to reproduce only specific scales and particle species at a time, while understanding dissipation at kinetic scales require resolving simultaneously elec-

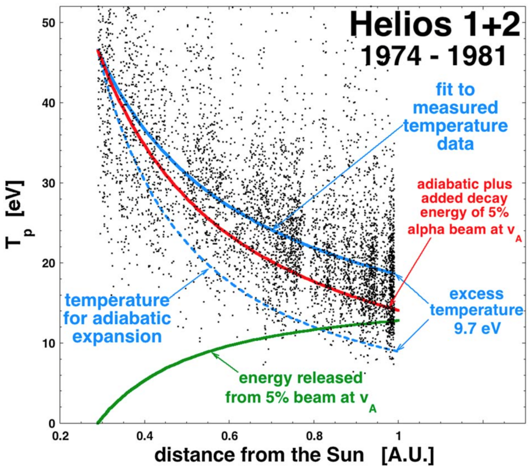

Figure 12: *Non-adiabatic heating of protons in fast solar wind. Hourly averaged measurements of the proton temperature are in black with a blue curve showing a power law fit. The dashed-blue curve is the expected proton temperature for adiabatic expansion without in situ proton heating. The green curve is the expected energy added to the protons by the decay of the alpha- proton relative drift. The red curve is the expected temperature of the solar wind protons with the energy of the green curve added*[96].

trons, protons and heavy ions each at their own kinetic scales. At present, simulations are not capable to reproduce such physics in detail. Yet it is expected that simulations will open in next decade new pathways to understand turbulence and its dissipation and the observations provided by THOR will be timely to provide validation of such new simulations.

Important electron and ion heating and acceleration at kinetic scales can occur through damping of a number of wave modes such as kinetic Alfven, fast and slow magnetosonic, whistler and electrostatic waves[33,97], as discussed in Section 2.2. How the dissipated energy is distributed between electrons and ions depends on the specific dissipation mechanisms as well as on plasma conditions such as amplitude of turbulent fluctuations, plasma β , plasma composition etc. Different mechanisms also produce different features in the distribution functions e.g. parallel or perpendicular anisotropies with respect to the magnetic field that can be used as evidence of a specific mechanism. As important example, kinetic Alfven waves (KAWs) can be dissipated at proton scales via Landau damping, stochastic heating resulting in proton heating in parallel, perpendicular direction respectively, as well as in electron heating[25,108]. On the other hand, solar wind observations suggest that KAW turbulence is only slightly damped at the proton scales and that most of energy is dissipated below proton scales into parallel electron heating by electron Landau damping[21]. Numerical simulations of dissipation of turbulent fluctuations at electron scales suggest that heating is directed mainly to electrons, such that they are 20% hotter than the protons[27]. Simulations also show that electrons are heated predominantly in the parallel direction.

Solar wind observations indicate that heavier ions (alpha particles in particular) seem to be preferentially heated with respect to the protons, the temperature ratio between the two species being more than mass proportional[98]. As an example, dissipation of KAWs via stochastic heating seems to have a greater efficiency for heavier ions, pointing out the privileged alpha particles channel for heating and energy dissipation in the solar wind[109]. Preferential turbulent heating and acceleration of alpha particles can also be produced by dissipation of cyclotron waves[110], see Figure 13. Such waves can also be efficient to energize oxygen ions and produce highly complex velocity distribution functions and temperature anisotropies[111,112]. Wave damping also plays an important role for mass-dependent heating and acceleration of heavier ions in shock regions. An example is the observation of oxygen ions around quasi-parallel shocks. Such ions can be in many cases explained as escaping from the magnetosphere, yet it's not understood if they can also be related to local acceleration by quasi-parallel shock fluctuations[113].

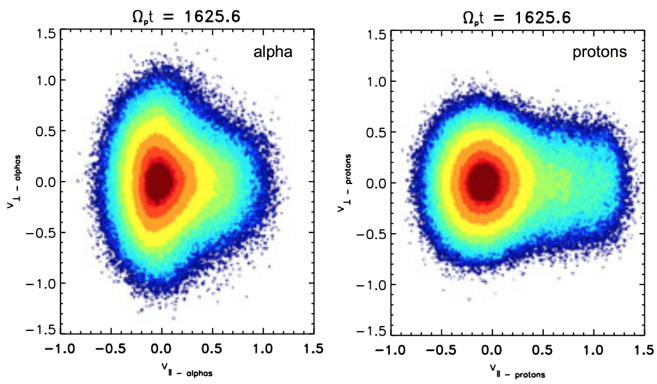

Figure 13: *Snapshots of the ion velocity distributions of He^{++} ions and protons when the system was initialized with a broadband spectrum of Alfvén-cyclotron waves* [110].

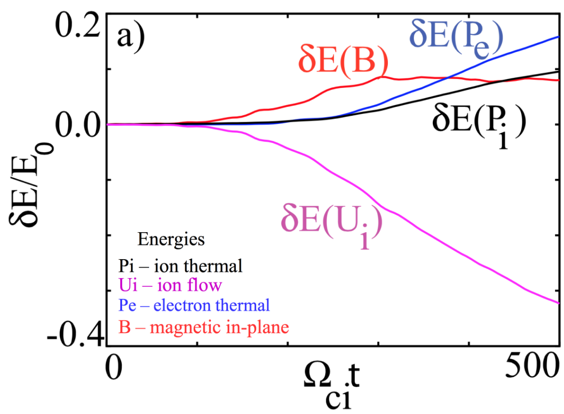

Figure 14: *Time evolution of δE from their initial value for electron thermal energy, ion thermal energy, in-plane magnetic field energy, and ion flow energy. δE is defined to be the change in the energy for each component from its initial value*[29].

Important heating and acceleration of electrons and ions is also expected within coherent structures such as reconnecting current sheets, magnetic islands, vortex-like structures etc. Yet the energy partition between electrons and ions in such localized dissipation is not fully understood. Figure 14 the time history of the changes in the energy budget for a kinetic simulation of shear-flow turbulence where a large number of dissipating small-scale coherent structures is formed. About 30% of the initial energy in the flow has been converted into other forms, with about 25% of such energy going into ion heating and 50% into electron heating. The simulation also shows that electrons are mainly heated in the direction parallel to the magnetic field, consistent with expected heating due to parallel electric fields generated in the reconnection process[29]. Such type of dissipation has been observed *in situ* and electron heating was found in small-scale current sheets, yet it was not possible to measure electron temperature anisotropy and no quantitative comparison with ions was possible due to the lack of measurements of ion distribution functions[31] (**RS-6**, **RS-7**, **RS-8**, **RS-9**, **RS-10**).Numerical simulations show that heating and acceleration signatures occur for protons, alphas around thin current sheets having scales comparable to the proton, alpha inertial lengths respectively, see Figure 15 top[114]. Simulations also show that the increase in temperature is more efficient for alphas than for protons, see Figure 15 bottom[115]. At present, there are no *in situ* simultaneous measurements of both proton and heavy ion distribution functions within kinetic scale current sheets that can be used to assess the energy partition between protons and ions during localized dissipation, in particular due to the fact that heavy ions, e.g. alpha particles, have been very seldom measured at time resolutions comparable with their kinetic scales (**RS-6**, **RS-5**, **RS-8**, **RS-10**).

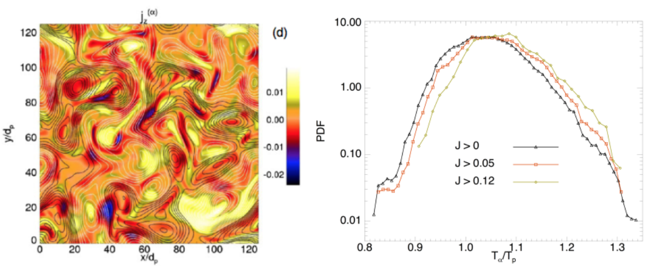

Figure 15: *Left: contour plots (shaded colors) of the out-of-plane alpha particle current density. Magnetic field lines are indicated by black/white lines. Right: distribution of the alpha-to-proton temperature anisotropy(right) for three different thresholds of the total current (proton + alphas)*[114,115].

Energy partition between species at kinetic scales is basically unexplored from *in situ* measurements. THOR measurements of electrons, protons and heavy ions at temporal resolution comparable with their kinetic scales and at high energy and angular resolution will allow to solve this key issue.

2.3.2 Partition between heating and acceleration

Understanding energy dissipation at kinetic scales requires also assessing how energy is distributed between thermal and non-thermal components. Figure 16 shows typical components of particle distribution functions for collisionless plasmas. The thermal component is represented by a maxwellian distribution; particle heating typically corresponds to an increase of the temperature of such distribution. The suprathermal component refers to energies several time larger than the thermal energy while the energetic component to energies many times larger. Both suprathermal and energetic component are typically approximated by power-law distributions. It is very little understood from *in situ* measurements how the energy dissipated by turbulent fluctuations is distributed between these different energy ranges, and most of the knowledge comes from numerical simulations.

Mechanisms of uniform dissipation such as linear Landau and cyclotron damping and stochastic heating produce heating and suprathermal acceleration e.g. beams[97] but in some cases they can lead also to the formation of energetic particles in the form of power-law tails[116,117]. Localized dissipation within coherent structures at kinetic scales such as thin reconnecting current sheets and small-scale magnetic islands seem on the other hand efficient to both heat plasma and create energetic particles[77,78,80,118,119]. Thermal, suprathermal and energetic particles can be found at different spatial locations within the turbulence, suggesting different heating and acceleration mechanisms at work[80], as shown in Figure 16. Energetic particles typically constitute a small fraction of the energy partition (∼few %) during dissipation within coherent structures[29] although in some cases the total energy density of the energetic particles can be comparable with the remaining magnetic energy suggesting that, at least in some cases, equipartition between energetic particles and magnetic field is energetically accessible[118].

Another example where partition between thermal and non-thermal ranges is important is the case of diffusive shock acceleration (DSA) at quasi-parallel shock[120,121]. Such mechanism is responsible for the formation of power-law spectra of energetic particles, however thermal particles must be pre-accelerated to supra-thermal energies first for the DSA acceleration to take place. How this pre-acceleration, the so called injection, occurs is far from being understood. Numerical simulations strongly suggest that dissipation of electromagnetic fluctuations at kinetic scales is responsible for it[121] although how much turbulent fluctuations dissipate into heating or supra-thermal particle acceleration is not understood.

Energy partition among energy ranges at kinetic

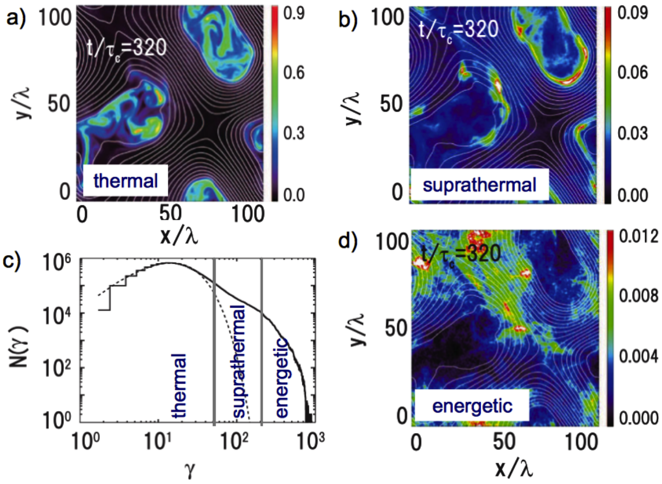

Figure 16: *Numerical PIC simulations of thermal, suprathermal and energetic particle acceleration in turbulent plasma*[80]*. Plasma heating and particle acceleration occurs at kinetic scales but in different locations.*

scales is basically unexplored by *in situ* measurements. THOR simultaneous measurements of electrons and ions distribution functions in thermal and supra-thermal range and, in some cases, energetic range at temporal resolution comparable to kinetic scales will allow to understand how energy dissipation is channeled in different energy ranges (**RS-5**, **RS-8**, **RS-9**, **RS-10**, **RS-11**).

2.4 Different regimes of turbulent plasma

Science question III: How does dissipation operate in different regimes of turbulence?

The third science question that THOR will answer is how dissipation operates at kinetic scales in different turbulent regimes. This will allow understanding which turbulent fluctuations and dissipation mechanisms are dominant under specific plasma conditions and how plasma energization works in solar system plasmas. The near-Earth space provides an excellent laboratory to test this, thanks to the different regions sampled by THOR along its orbit (**RS-12**), see Figure 2. These regions are characterized by different values of typical plasma parameters e.g. amplitude of turbulent fluctuations, plasma β, plasma composition, homogeneity, collisionality, Mach number, system size etc. Key regions are the pristine fast and slow solar wind, interaction regions between flows, shocks and associated sheath regions. Such near-Earth regions are representative of a number of astrophysical turbulent environments, so that the identification of dominant dissipation mechanisms by THOR would help understanding dissipation in distant objects where *in situ* measurements are not available.

2.4.1 The pristine solar wind

The pristine solar wind plasma can be divided in two main components of different solar origin: fast and slow. Their relative occurrence in near-Earth space depends on the level of solar activity. Around solar maximum, that is expected during THOR mission, slow wind dominates with a minor presence of shorter fast streams. Fast and slow wind are characterized by different bulk speed, density, temperature, composition and magnetic field. Slow wind is typically colder and denser than the fast wind. Moreover, turbulence in slow wind is more developed and has higher intermittency, resulting in a larger number of small-scale structures[7]. Another important difference is that the slow wind plasma is generally more collisional than fast wind. All these differing parameters result in small-scale turbulent fluctuations being associated with different dissipation mechanisms at kinetic scales for the slow and fast wind.

Uniform dissipation mechanisms, such as wave damping due to Landau and cyclotron resonances and stochastic heating, have been invoked to explain pristine solar wind heating[21,22,25], as discussed in 2.2. On the other hand, both fast and slow wind are highly intermittent, with formation of small scales structures where localized dissipation, e.g. due to reconnection in thin current sheets, is likely to take place[7,32]. It is not yet demonstrated from observational point of view which dissipation scenarios dominate in the pristine solar wind and how they depend on plasma parameters such as, e.g., the amplitude of fluctuations or plasma beta. Some observations even suggest that the same magnetic energy spectrum can be associated to either kinetic Alfvén waves (KAWs) or coherent structures[21,30,32].This dependence of dissipation mechanisms on different plasma parameters requires a specific investigation of kinetic turbulence in fast and slow solar wind. THOR will sample repeatedly the pristine solar wind, performing high sensitive and accurate electromagnetic and high resolution particle measurements in both slow and fast wind (**RS-12**, **RS-2**, **RS-3**, **RS-4**, **RS-5**, **RS-6**, **RS-8**, **RS-9**, **RS-10**). This will allow understanding the connection between the nature of turbulent fluctuations and dissipation in pristine solar wind.

The pristine solar wind can be important for understanding energy dissipation in other distant turbulent environments where *in situ* measurements are not available, e.g. weakly collisional plasmas such as intracluster plasma in galaxy clusters, accretion disks and the interstellar medium[33,123–125]. The interstellar medium has a plasma composition similar to that of solar wind (mainly hydrogen and helium)[126] and is suggested to be turbulent by remote observations[122]. Turbulent dissipation occurs there, with intermittent heating in vortex-like structures is one key mechanism invoked for star formation process[127]. Turbulent dissipation is also important for the amplification of magnetic fields and for the re-acceleration and diffusion of cosmic rays. Remote observations in the interstellar medium do show a typical Kolmogorov-like spectrum in the inertial

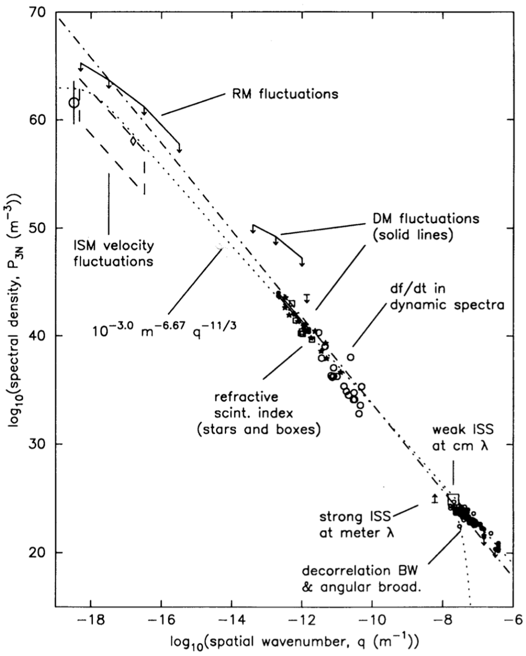

Figure 17: *Inferred three-dimensional electron density power spectrum vs. wavenumber. Dotted line shows Kolmogorov spectra* [122]

range as in the solar wind, see Figure 17, yet no remote measurements can unambiguously resolve the kinetic scales, although some measurements seem to suggest a -2 spectral exponent below the ion gyroscale[128]. The resolution of such remote measurements is expected to improve thanks to new observatories, e.g., LOFAR and SKA. THOR *in situ* measurements in the pristine solar wind at kinetic scales will be very important to support and complement such new remote measurements.

2.4.2 Interaction regions between flows

Interaction regions between flows are regions of strong turbulence in astrophysical plasmas and are associated to important plasma transfer, mixing, and energization. One example of such flow interaction regions are shear-flow boundaries where Kelvin-Helmholtz (KH) instability develops. Such large scale instability can drive turbulence at small scales and has been observed *in situ* within planetary magnetospheres[88,129,130] and at the heliopause[131]. KH instability is also expected to occur in pristine solar wind due to the interaction of strongly twisted magnetic flux tubes originated in the solar corona and carried away by the wind[132,133]. Energy dissipation associated to Kelvin-Helmholtz turbulence plays an important role for understanding plasma heating and particle acceleration in the solar wind, as well as for understanding the interaction between the Sun and the planets, the so-called space weather. Other examples of flow interaction regions are the boundaries between fast and slow wind streams, the so-called corotating interaction regions (CIRs), where turbulent fluctuations can be important for several energization mechanisms, e.g. scattering of energetic particles[134]. Recent results, on the other hand, indicate that typical signatures of large-scale turbulence, such as spectral slopes and entropy changes, are not evident within CIRs suggesting that driving of turbulence by shear could be less important than expected[135]. More observations of CIRs, particularly at kinetic scales, are needed to clarify this issue and assess the importance of turbulence and associated energy dissipation within CIRs.

Recent large-scale kinetic simulations of shear-flow turbulence[29,87], see Figure 4, show that localized dissipation in small-scale current sheets and magnetic islands is dominant with respect to dissipation by wave damping. The major electron heating mechanism is parallel heating by parallel electric field produced by small-scale reconnection events. Thin current sheets at ion scales have been observed around Kelvin-Helmholtz vortices[136]. Yet, the lack of high temporal and energy resolution particle measurements made it impossible to measure the expected particle anisotropies. It is not yet established from observational point of view if localized dissipation within coherent structures is indeed the dominant dissipation mechanisms within flow interaction regions and more detailed measurements are needed to solve this problem (**RS-6**, **RS-7**, **RS-8**, **RS-9**, **RS-10**). Simulations also indicate that the properties of shear-flow turbulence at kinetic scales can be different between two-dimensional and three-dimensional turbulence. Accurate measurements of turbulence anisotropies at kinetic scales for the case of shear-flow turbulence are needed to understand how dissipation depends on the properties of such turbulence (**RS-3**,**RS-6**,**RS-7**). THOR will explore plasma interaction regions both at interplanetary boundaries, such as corotating interaction regions, and at the magnetopause boundary between the solar wind and the Earth's magnetosphere (**RS-12**) and will allow understanding energy dissipation within such regions.

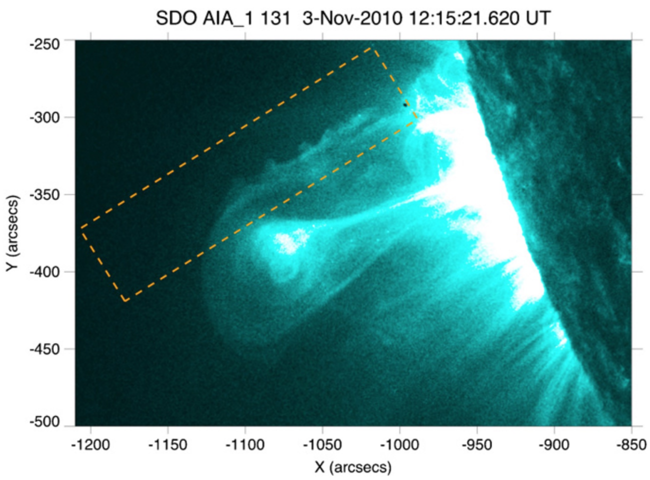

Figure 18: *Fast coronal mass ejecta erupting from the Sun, with KH waves detected on its northern flank, the SDO/AIA image* [137]

Observations with inflow interacting regions in near-Earth space can be important to understand energy dissipation mechanisms in distant environments. One such example is energy dissipation in the solar corona in presence of shear flows. Kelvin-Helmholtz vortices have been observed through remote measurements in the solar corona at the surface of a fast coronal mass ejection[137], see Figure 18, but no assessment of energy dissipation is possible through such measurements. Such energy dissipation scenario is also important for other astrophysical environments where shear flows are expected, such as astrophysical jets and accretion disks. In accretion disks, the large-scale magnetorotational instability[138] is thought to generate MHD turbulence that is eventually dissipated at kinetic scales, producing plasma heating and particle acceleration in the disk. Remote measurements of the radiation coming from such distant objects are even less detailed than in the solar corona, and the exact energization mechanisms are unknown.

2.4.3 Shocks and associated sheath regions

Shock are sources of turbulence and regions of important energy dissipation and particle acceleration in astrophysical plasmas[139]. Three major regions are associated to shocks and are important for energy dissipation: the upstream region (foreshock), the shock itself and the downstream region of shocked plasma (sheath region). Shock turbulence strongly depends on the large-scale properties of the shock, such as e.g. the angle between the upstream magnetic field and the normal to the shock surface θ_{Bn}, the system size and the Mach number. Figure 19 shows large-scale kinetic simulation of the terrestrial bow shock. This shock is the most studied due to the availability of many *in situ* observations, such as those by Cluster spacecraft that allowed the detailed three-dimensional magnetic field characterization of turbulent fluctuations down to ion scales. Yet a deeper understanding of energy dissipation and plasma energization mechanisms related to these fluctuations has not been possible due to the lack of accurate electric field measurements as well as high temporal, angular and energy resolution particle measurements.

The quasi-parallel shock ($\theta_{Bn} < 45^\circ$) is the shock region where the strongest turbulence is observed, as indicated by Figure 19, top-left panel where amplitude of magnetic fluctuations is shown. Strong energy dissipation and particle energization due to turbulence is expected there. In the foreshock of quasi-parallel shocks, an important source of turbulence is represented by low-frequency waves generated by reflected ions[91,100,140]. Earlier observations indicated that basic wave generation mechanism is related to the cyclotron resonance of such ions with the waves themselves, yet many important details of the wave and ion beam generation processes remain unexplained[100,141]. Observations in the quasi-parallel foreshock show high amplitude fluctuations having $|\delta\mathbf{B}|/B \sim 1$, often referred to as SLAMS[84,142], shock-like kinetic structures (shocklets), finite compressibility and non-gyrotropic particle distributions, most likely involving specular reflection of ions at the shock and/or nonlinear trapping of ions in the wave fields. In the downstream sheath regions the compression of the flow affects the spectrum of the turbulent fluctuations transmitted through the shock e.g. SLAMS, by increasing the amplitude of the fluctuations perpendicular to the shock normal and compressing the wavenumber in the direction parallel to it[143,144]. This will lead to enhanced dissipation as wave energy from the inertial range is abruptly amplified and transported to the dissipation range, leading to additional heating of the downstream plasma. Other turbulent fluctuations can be on the other hand generated locally, e.g. current sheets, magnetic islands, vortexes etc. as found in kinetic simulations[91,140], see Figure 19, bottom, right panel. Turbulent fluctuations at kinetic scales in quasi-parallel shock regions leads to strong plasma heating and particle acceleration to high energies. One example is small-scale reconnection occurring in thin current sheets in the terrestrial magnetosheath[20,31]. The efficiency of such small-scale reconnection seems to depend on shock boundary conditions and parameters such as the θ_{Bn} and systems size. Current sheets and magnetic islands are much more frequent in the quasi-parallel magnetosheath than in the quasi-perpendicular[31,140]. However, the exact dependence of this dissipation mechanism on θ_{Bn} is not known. Furthermore, the number of current sheets and islands and their interactions is expected to increase with the size of the magnetosheath[140], suggesting that dissipation due to turbulent reconnection could be stronger in the

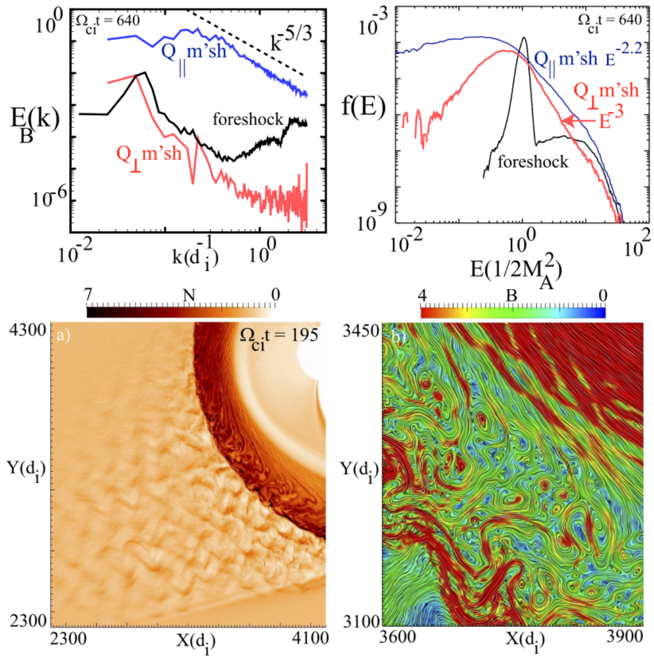

Figure 19: *Large-scale particle-in-cell numerical simulation of the terrestrial bow shock. Top, left: spectra of magnetic fluctuations. Top, right: proton distribution functions. Bottom, left: map of plasma density. Bottom, left: map of magnetic field*

larger sheath regions associated to interplanetary shocks. Another example is diffusive shock acceleration (DSA) that is one of the most important mechanisms invoked for particle acceleration in astrophysical plasmas and is efficient at quasi-parallel shocks[121]. This mechanism is the prime candidate to explain the acceleration of galactic cosmic rays in supernova remnants to energies of $\sim 10^{15}$ eV and beyond. In DSA mechanism, particles are scattered in pitch angle by turbulent fluctuations so that they cross back and forth the shock and gain energy at each shock crossing[120]. However, thermal particles must attain a threshold energy through an "injection" mechanism in order to get efficiently accelerated by DSA mechanism. Despite of this importance, the mechanism of particle injection is not fully understood. Kinetic scale turbulent fluctuations in shock regions, e.g. SLAMS or foreshock cavities, are important candidates for particle injection by reflecting and scattering ions.

The quasi-perpendicular shock ($\theta_{Bn} > 45^{\circ}$) is typically associated to lower amplitude of turbulent fluctuations, as indicated by Figure 19 top, left panel. Yet such fluctuations can play a significant role for particle energization at kinetic scales. Field-aligned beams (FABs) observed upstream of quasi-perpendicular terrestrial bow shock have distributions showing high-energy tails that are produced by intermittent turbulence[145]. On the downstream side, different fluctuations (e.g., mirror modes) grow because of free energy in the anisotropic ($T_{\perp} > T_{\parallel}$) ion distributions[101]. Combined with evolution in a structured and sheared downstream flow, these fluctuations will act as another source of turbulence relatively close to the dissipation range.

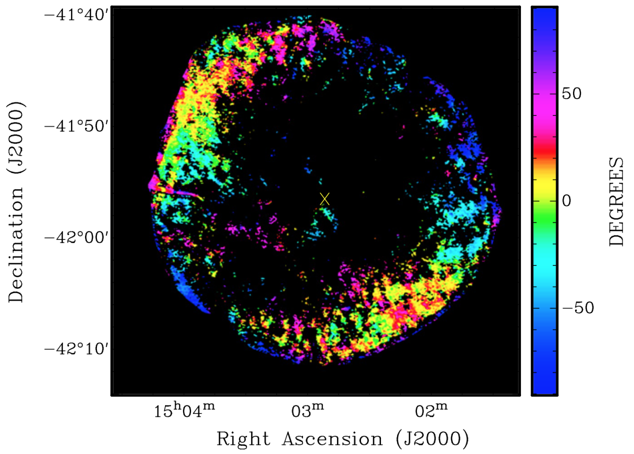

Figure 20: *Magnetic field orientation at supernova remnant SN 1006, where yellow corresponds to radial magnetic field and blue to perpendicular to the radial direction. The most efficient particle acceleration and generation of magnetic turbulence in SN 1006 is attained for shocks in which the magnetic field direction and shock normal are quasi-parallel, while inefficient acceleration and little to no generation of magnetic turbulence are obtained for the quasi-perpendicular case*[15].

Despite of the importance of turbulence in shock regions, *in situ* measurements assessing the role of turbulent fluctuations for particle heating and acceleration at kinetic scales are few. The three-dimensional magnetic structure fluctuations, e.g. SLAMS or shocklets, has been studied in detail by e.g. Cluster spacecraft for the case of the terrestrial shock. However, accurate measurements of electric field as well as high resolution particle measurements are still missing. Because of its orbit THOR will be an excellent mission to study turbulent fluctuations and dissipation at kinetic scales in shock regions. THOR will make observations of both the the Earth's bow shock and of interplanetary shocks (**RS-12**). THOR particle measurements with high temporal, angular and energy resolution and resolving different species will be crucial to study how energy dissipation at kinetic scales depends on plasma parameters and boundary conditions (e.g. different θ_{Bn} and system size) in different shock regions (foreshock, shock and sheath) (**RS-5**, **RS-8**, **RS-9**, **RS-10**, **RS-11**). By comparing shocks with different parameters (Mach numbers, obliquity, size), THOR will identify properties that are universal and independent of the size of the system. This information can be exported to other larger size heliospheric (coronal shocks, solar-wind termination shock) or astrophysical scenarios.

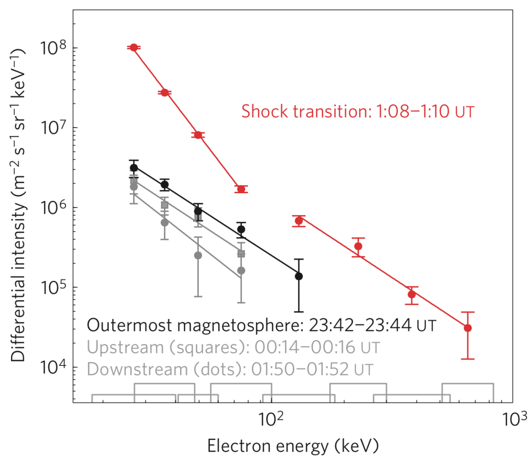

Figure 21: *Electron acceleration to relativistic energies at a strong quasi-parallel shock wave within the Saturn's bow shock*[146].

One such astrophysical example are supernova remnant shocks that are site of major acceleration of galactic cosmic rays and are thought to be efficient for particle acceleration when the shock is quasi-parallel[15], as shown in Figure 20. *In situ* observations of strong particle acceleration and turbulence at quasi-parallel shock having relatively large Mach number (up to $\sim$100) have been reported at Saturn's bow shock[146], however particle instrumentation was not sufficient to resolve the detailed processes responsible for the particle acceleration, see Figure 21. Higher resolution observations e.g. by Cluster spacecraft have been reported for the case of Earth's bow shock[38], which on the other hand has much smaller size and lower Mach number (typically below 10) than other planetary and interplanetary shocks. THOR observations in different quasi-parallel shock regions will contribute advancing our understanding of particle acceleration therein.

2.5 Additional science

In addition to the prime mission goals there are quite a few additional important science questions that can be addressed with THOR. Here we shortly describe a few such examples.

Turbulence at fluid scales in the solar wind The THOR mission will also allow to improve our understanding of turbulence at fluid scales. Turbulent cascade at such scales can occur if there are counter-streaming waves in the sunward/antisunward direction. Being sun-pointing, THOR will allow the most precise test of this process by performing the most exact Poynting flux measurements of waves and computation of Elsasser variables(**RS-3**,**RS-2**).

Reconnection in the solar wind THOR will allow to study with high accuracy reconnecting current sheets in the solar wind [147–149] by e.g. estimating the exact inflow speeds into current sheets and separatrices through both $\mathbf{E} \times \mathbf{B}$ measurements (**RS-3**) and particle moments measurements (**RS-5**, **RS-6**, **RS-7**). This will allow to accurately measure the reconnection rate and the energy dissipation rate $\mathbf{E} \cdot \mathbf{J}$. THOR will also allow accurate studies of the breaking of the condition of frozen-in magnetic fields and related Hall physics.

Reconnection-generated turbulence in the solar wind The identification of small-scale fluctuations in reconnection regions is very important for understanding energy dissipation during reconnection. Large gradients and anisotropies are observed around such regions supporting a variety of wave generation mechanisms. One important example is the reconnection outflow region, where waves and turbulence have been observed[150,151]. Reconnection outflows can generate local turbulence with different characteristic wavenumbers implying the occurrence of different dissipation mechanisms near ion scales[151]. THOR high temporal resolution field and particle measurements will allow to identify the structure of reconnection outflows, including embedded flux tubes, regions with enhanced temperature anisotropies[151,152] or intermittent structures[83] (**RS-1**, **RS-6**, **RS-7**, **RS-8**, **RS-9**, **RS-10**).

Electromagnetic emission generation in the solar wind Another important additional science question which can be studied using THOR is how electromagnetic waves are produced in type II solar radio burst. Only a small number of type II source regions have been observed directly by past missions, e.g. Wind and Stereo [153,154]. Although these missions have electric field instruments capable of resolving the Langmuir waves, they lack magnetic field instruments which can resolve waves at the plasma frequency and its harmonics. As a result the mechanisms responsible for radio wave emission are still a matter of debate. It is expected that THOR will encounter a number of type II source regions in the solar wind. THOR better wave measurements of both electric and magnetic fields at the plasma frequency and its harmonics will allow us to understand in detail the generation mechanisms (**RS-1**, **RS-2**).

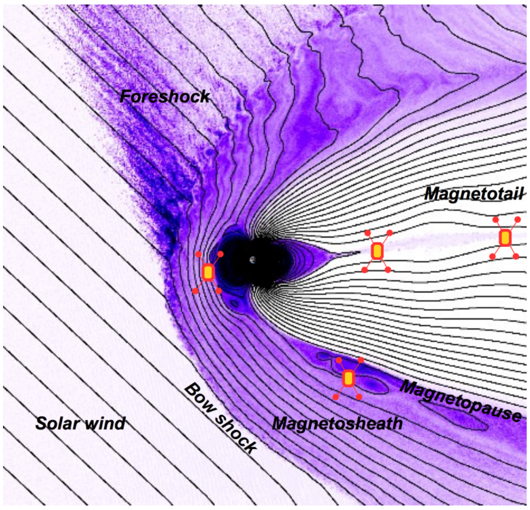

Figure 22: *Regions of interest for THOR science in the near-Earth space. Beyond the main regions (solar wind, shock and magnetosheath) THOR will also make observations at the magnetopause boundary and in the magnetotail.*

Magnetospheric regions During a substantial part of the orbit, THOR will be in the Earth's magnetosphere, see Figure 22, where several important additional science questions can be addressed such as the structure of the magnetopause and magnetotail current sheet at kinetic scales, the microphysics of Kelvin-Helmholtz instability at the magnetopause and the microphysics of plasma jets fronts in the magnetotail. We describe one such example below.

Plasma jet fronts in the magnetotail The interaction of fast jets with ambient plasma results in the formation of jet fronts[155–157]. Jet fronts are important for energy dissipation and particle energization at kinetic scales, the front itself having a thickness ranging from few ion to electron scales[158,159]. One important question is whether such thin jet fronts are shock-like structures, as expected in solar corona and other astrophysical environments and suggested by Cluster observations[157], or tangential discontinuities with no plasma flow across[155,156]. It was not possible to solve this problem with the available data, due to the insufficient accuracy of electric field measurements as well as due to the low time resolution of particle measurements, that are required to quantify plasma inflow across the front and evaluate energy dissipation through $\mathbf{E} \cdot \mathbf{J}$. THOR will provide such measurements (**RS-3**,**RS-6**,**RS-7**).

Space weather During its nominal mission of three years, THOR can serve as a support for other spacecraft missions in near-Earth space and address science that is important for space weather (**RS-12**). The recent COSPAR Roadmap on Space weather[b] spells out several key requirements to progress in such science. In the nearest term, it will be crucial to improve our understanding of which solar wind structures, seen at L1 by monitoring missions, can actually reach the Earth's magnetosphere and become "geo-effective" there. This science is very important for both the space plasma and space weather communities and can be investigated by THOR already during its nominal lifetime. THOR observations, together with those from still existing and/or newly arriving L1 missions, will lay the foundation for the planning of a later optimised long-term space weather monitoring program. On a longer term, the roadmap spells out the need for a coordinated fleet of solar wind monitoring spacecraft in suitable locations around L1 and on suitable orbits between L1 and the Earth. Depending on the results of the initial science phase, it can be envisaged to move THOR around L1 during its extended phase. In this phase, the mission would probably no longer be operated by the ESA Science and Exploration Program, but it could be managed e.g. by the SSA program, becoming one important key European asset in a coordinated global inter-agency fleet of spacecraft.

[b] https://cosparhq.cnes.fr/sites/default/files/executivesummary_compressed.pdf

3 Scientific requirements

Table 1 shows the traceability matrix from the science objectives to science measurement requirements. Due to the complexity of plasma physics each science objective requires several science measurement requirements to be fulfilled. The science requirements themselves and how they trace to instrument performance requirements is given in Table 2. Finally, general mission requirements are summarized in Table 4.

3.1 Science Measurement requirements

Temporal and spatial scales Most of the science measurement requirements for THOR are formulated with respect to kinetic scales and we need to know the expected kinetic scales of plasma to convert science requirements into instrument performance requirements. Table 2 shows how science measurements requirements are traced into instrument performance requirements. Figure 23 shows statistical distribution of characteristic plasma parameters in solar wind and magnetosheath. These allow to estimate characteristic plasma waves frequencies and also temporal scales corresponding to spatial kinetic scales Doppler shifted by the solar wind. Figure 24 summarizes expected plasma temperature and density parameter ranges that THOR will encounter and Figure 25 summarizes all the expected temporal scales in solar wind and magnetosheath. Figure 25 also summarizes the main science requirements on temporal resolution of fields and particles which are discussed below.

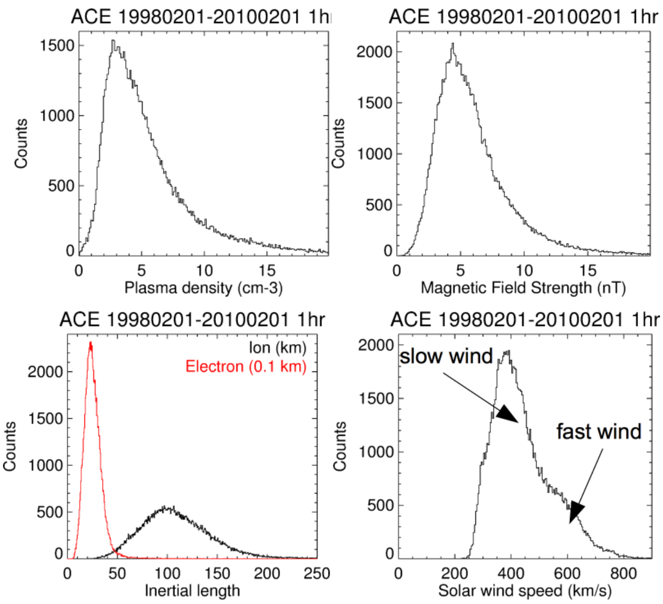

Figure 23: *Typical solar wind parameters based on ACE data. In magnetosheath B and n values are roughly 4 times higher and inertial length 2 times smaller.*

Fields temporal resolution To identify electric and magnetic fields in turbulent plasma down to the smallest in space and shortest in time dissipation scales, E and B fields should be measured with sufficient temporal resolution to resolve the Doppler-shifted Debye length scales and plasma frequency (**RS-1**), see Figure 25. The existing or upcoming missions, such as Cluster, could resolve **E** but not **B** at such a high temporal resolution. However, both **E** and **B** have to be resolved to identify important energy dissipation processes at the smallest scales, e.g. such as due to fast solitary waves and Langmuir waves. Preferentially all three components of **E** and **B** have to be measured for high frequency waves to make possible wave and structure polarization identification.

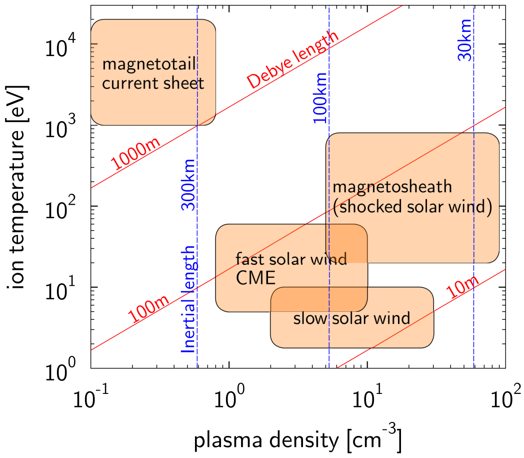

Figure 24: *Expected plasma parameters encountered by THOR. Electron temperatures are comparable to proton temperatures in solar wind but factor 3-5 smaller than proton temperatures in magnetosheath and plasma sheet. Proton kinetic scales are defined by proton inertial length which is comparable to proton gyroradius. Electron kinetic scales are roughly 40 times smaller than proton kinetic scales.*

Fields sensitivity To resolve waves and coherent structures in turbulent plasma both **E** and **B** measurements must have sufficient sensitivity (**RS-2**). The most sensitive **B** measurements in the solar wind at kinetic scales so far have been carried out by Cluster. Figure 26(top) shows a few examples of magnetic fluctuation spectra, the dashed line being the instrument noise level. It is seen that the amplitude of fluctuations is comparable to the noise level at the electron scales. This is confirmed by Figure 26(bottom) showing the statistics over all solar wind events of signal to noise ratio at electron scales. To satisfy the requirement **RS-2** the sensitivity of **B** measurement has to be increased at least several times in comparison to Cluster (**RI-2**). On the other hand, the requirements on the sensitivity levels for **E** field measurements is comparable to earlier missions. However, it is important that at least two component of **E** are measured with the required sensitivity levels (**RI-2**). The sensitivity of electric field is discussed in the payload section, see Figure 41.

Table 1: *THOR Science Traceability Matrix*

Cosmic Vision	2. How does the Solar System work? 2.1 From the Sun to the edge of the Solar System											
THOR science theme:	Turbulent energy dissipation and particle energization											
		Science Measurem. Requirem.										
Science Questions		Fields				Particles						
		RS-1	RS-2	RS-3	RS-4	RS-5	RS-6	RS-7	RS-8	RS-9	RS-10	RS-11
1. How is plasma heated and particles accelerated? (Sec. 2.2)	Wave mode identification and spectra	✓	✓		✓	✓	✓	✓				
	Effects of wave damping on plasma					✓	✓	✓	✓	✓	✓	✓
	Coherent structure identification	✓	✓	✓	✓	✓	✓	✓				
	Effects of coherent structures on plasma					✓	✓	✓	✓	✓	✓	✓
2. How is the dissipated energy partitioned? (Sec. 2.3)	Among electrons, protons and heavier ions					✓	✓	✓	✓	✓	✓	
	Between heating and particle acceleration					✓			✓	✓	✓	✓
3. How does dissipation operate in different regimes of turbulence? (Sec. 2.4)	Pristine solar wind	✓	✓	✓	✓	✓	✓	✓	✓	✓	✓	✓
	Flow interaction regions	✓		✓	✓	✓	✓	✓	✓	✓	✓	✓
	Shocks and sheath behind shocks	✓		✓	✓	✓	✓	✓	✓	✓	✓	✓

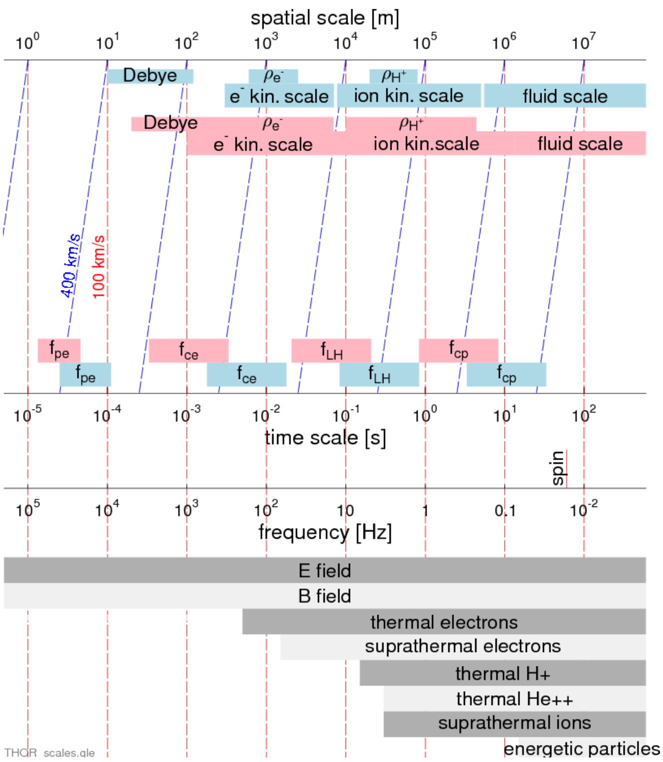

Figure 25: *Typical temporal and Doppler shifted spatial scales of physical processes in the solar wind and their comparison to the temporal resolution of THOR instrumentation.*

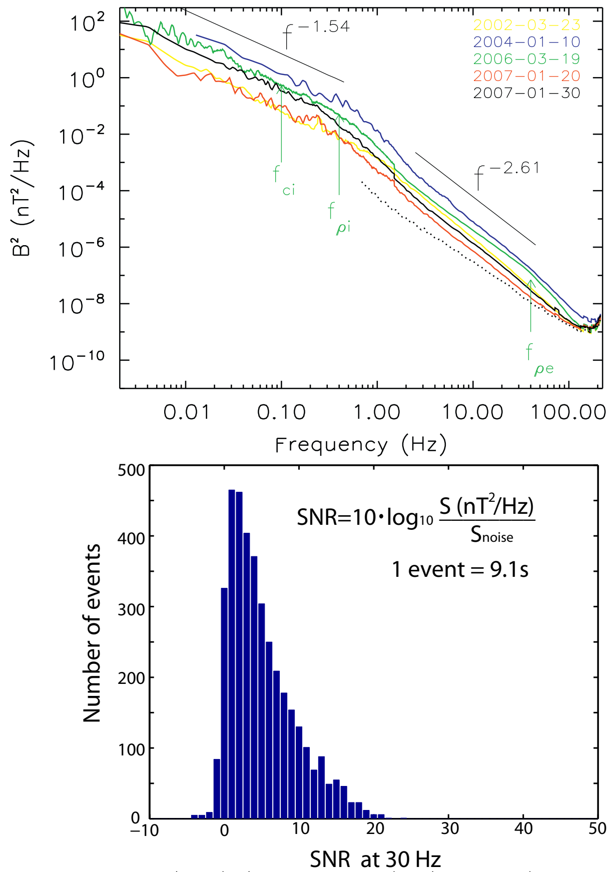

Figure 26: *(top) (Fig. 7 in 53). (bottom) Statistics of signal to noise ratio at 30 Hz (roughly electron scale) from all Cluster solar wind observations when Cluster was in burst mode*[62].

Table 2: *Traceability of Science Measurement Requirements to Instrument Performance Requirements.*

Science Measurement Requirement	Instrument Performance Requirement
RS-1 E and **B** fields shall be measured with **temporal resolution** down to plasma frequency and Doppler-shifted Debye length scale.	**RI-1 E** and **B** fields shall be measured to resolve frequency range from DC to 100kHz.
RS-2 Measurements of **B** and at least two components of **E**, down to electron kinetic scales, shall be **sensitive** enough to have the noise floor significantly below the typical solar wind fluctuation levels.	**RI-2** At least two components of **E** shall be measured with sensitivity better than $[10^{-11}, 3\,10^{-14}, 2\,10^{-14}, 10^{-14}]$ $(\mathrm{V/m})^2/\mathrm{Hz}$ @$[10, 100, 10^3, 10^4]$Hz. **B** shall be measured with sensitivity better than $[3\,10^{-5}, 10^{-7}, 3\,10^{-10}, 5\,10^{-11}]$ $\mathrm{nT}^2/\mathrm{Hz}$ @$[1, 10, 100, 10^3]$Hz.
RS-3 B and at least two components of **E** shall be measured with sufficient **accuracy** to have error in $\mathbf{E}\times\mathbf{B}$–drift velocities less than 20% of the Alfvén velocity at DC levels and less than 10% for fluctuations.	**RI-3 B** shall be measured with accuracy better than 0.1 nT. At least two components of **E** shall be measured with absolute accuracy better than 0.1 mV/m for the DC measurement and better than 0.05 mV/m for fluctuations.
RS-4 It shall be possible to resolve phase velocities up to a few times electron thermal velocity.	**RI-4** The phase velocities of at least up to 10,000 km/s shall be possible to measure.
RS-5 At least H^+, He^{++} and O^+ ions shall be measured.	**RI-5** At least H^+, He^{++}, and O^+ ions shall be resolved with $m/dm \geq 8$.
RS-6 H^+ moments - density, velocity, temperature - shall be measured with sufficient temporal resolution to resolve the sub-H^+ scales. He^{++} moments should be measured at He^{++} scale.	**RI-6** H^+ moments – density, velocity, temperature – shall be resolved with a cadence down to 50 ms, He^{++} moments down to 300 ms.
RS-7 Electron moments - density, velocity, temperature and temperature anisotropy - shall be measured with sufficient temporal resolution to resolve the electron scales.	**RI-7** It shall be possible to measure electron moments - density, velocity, temperature and temperature anisotropy - with the temporal resolution of at least 5 ms.
RS-8 3D distribution functions of H^+ and He^{++} covering energies up to at least a few times the thermal energy shall be taken with sufficient temporal resolution to resolve the ion scales.	**RI-8** In pristine solar wind it shall be possible to measure H^+ 3D distribution function up to 8 keV with temporal resolution down to 150 ms, dE/E down to 5 % and angular resolution down to 3°. In magnetosheath it shall be possible to measure H^+ at least up to 5 keV with temporal resolution down to 150 ms, dE/E down to 10% and angular resolution down to 10°. He^{++} shall be measured with temporal resolution down to 300 ms.
RS-9 3D electron distribution function covering energies up to at least a few times times the thermal energy shall be taken with sufficient temporal resolution to resolve the electron scales.	**RI-9** It shall be possible to measure full 3D electron distribution function up to 500 eV with reduced angular and energy resolution at a cadence of 5ms.
RS-10 3D distribution functions at suprathermal energy range (up to a few tens times thermal energy) shall be measured with temporal resolution comparable to the respective kinetic scales.	**RI-10** 3D electron distribution function shall be measured in energy range 1–10 keV with temporal resolution down to 15 ms, dE/E down to 10 % and angular resolution down to 5°.
	RI-11 3D ion distribution function shall be measured in energy range 3–30 keV with temporal resolution down to 300 ms, dE/E down to 10 % and angular resolution down to 10°.
RS-11 Energetic electrons shall be measured up to relativistic energies (i.e., >511 keV), energetic ions up to a few times MeV/nuc to resolve the spectra produced by interplanetary shocks.	**RI-12** It shall be possible to measure 3D distribution function of electrons with energies up to 600 keV and ions with energies up to 8 MeV/nuc with temporal resolution down to 15 s.
RS-12 The science measurement requirements shall apply to at least the regions of main scientific interest: pristine solar wind, foreshock, bow-shock and magnetosheath.	**RI-13** Instrument operational capability shall be optimized for plasma parameters: n=1–100cc, Te=5–200eV, Tp=5eV–1keV, Talpha=5eV–4keV, Vdrift=0–1000km/s, B=1–200nT.

Fields accuracy To distinguish kinetic/inertial Alfvén waves, to resolve reconnection inflows into reconnecting current sheets, to resolve tangential discontinuities from shocklets moving in the plasma frame, it is crucial that **B** and two components of **E** are measured with sufficient **accuracy** to resolve large scale $\mathbf{E} \times \mathbf{B}$–velocities with precision higher than 20% of the Alfvén velocity and those for fluctuations with precision higher than 10%(**RS-3**). Alfvén velocity is about 50 km/s and 100 km/s in solar wind and magnetosheath respectively. This translates into the requirement on electric field accuracy of 0.05 mV/m and magnetic field 0.1 nT (**RI-3**). **RS-3** for the **E** measurements is neither satisfied by the current missions, such as Cluster, nor upcoming ones such as MMS.

The major limitation is that the accuracy of the DC measurement by axial booms (measuring the spin axis component) is normally worse than 1 mV/m and the accuracy of the sun-pointing component is about 1 mV/m. The most accurate measurement is done by the wire booms in the spin plane perpendicular to the sun line. This is demonstrated in Figure 27 which shows observations of Alfvén wave in the solar wind by Cluster. The sun-pointing measurement of E_X clearly shows low accuracy by differing significantly from the expected $(-\mathbf{v} \times \mathbf{B})_X$ value. This disagreement in addition depends on the plasma environment, being different in the beginning and end of the interval. The E_X measurement is also strongly affected by the spacecraft wake showing up as spiky field every second. Only the component perpendicular to the sun direction E_Y shows acceptable accuracy. Nevertheless, the total electric field constructed from the assumption $\mathbf{E} \cdot \mathbf{B} = 0$ is not accurate because of the low accuracy of E_X. Adding an axial probe in this case would not help to improve the accuracy. As discussed later, THOR solves the accuracy requirement by having the spin plane perpendicular to the sun line and thus being able to make high accuracy measurement in two directions (**RS-2**).

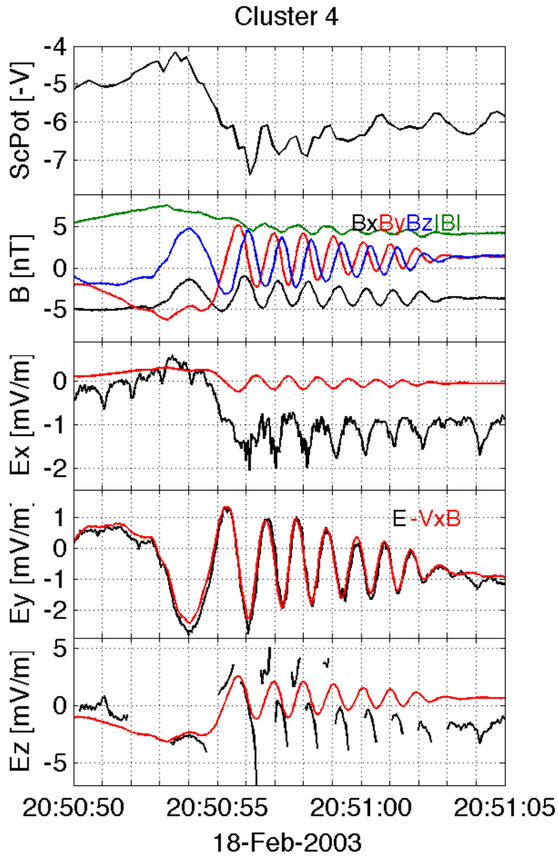

Figure 27: *Cluster observations of an Alfvén wave in the solar wind. Last three panels compare* **E** *measurements to expected* $-\mathbf{v} \times \mathbf{B}$ *values. While* E_Y *(perpendicular to the sun direction) is reliably estimated, the sun-pointing* E_X *is not. As a result, also* E_Z*, obtained using assumption* $\mathbf{E} \cdot \mathbf{B} = 0$*, is inaccurate. Having two accurate electric field components on THOR will allow accurate measurements of full* **E**.

Phase velocity To identify spatial scales of waves and coherent structures, as well as their efficiency in particle interaction it is important to resolve their phase velocity. Direct phase velocity measurement involves measuring the signal difference between probes separated by significant distance, such as Langmuir probes at the end of the wire booms in the spin plane. In such case, the full phase velocity vector can be reconstructed, if the orientation of the boundary or wave vector is known from other methods, e.g. minimum variance analysis. The highest values of phase velocities expected that has to be resolved are comparable to electron thermal speed, whistler phase velocity or electron Alfvén speed (**RS-4**). For typical values of solar wind plasma this translates into the requirement to resolve phase velocities up to about 10,000 km/s (**RI-4**). Existing and upcoming missions do not have sufficiently high temporal resolution of separate probe signals to achieve this. In addition to direct phase velocity measurements, also complementary indirect methods can be used. For example, for planar structures phase velocity can be estimated based on the Faraday's law, the tangential component of **E** should be constant in the structure reference frame. Some other methods are given in Table 29.

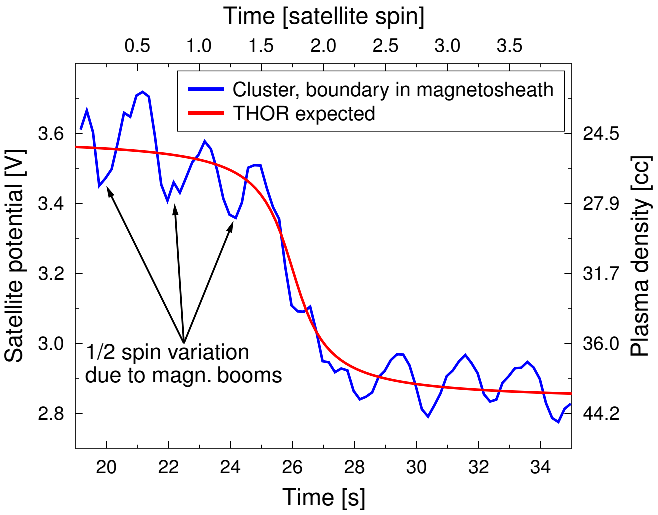

Figure 28: *Boundary observed in satellite potential. Cluster shows strong variations due to spin dependent changes in total illuminated area created by solid magnetometer booms. All spacecraft with large spin axis angle with respect to the Sun (Cluster, THEMIS, MMS, BepiColombo, ...) have such variations. No such variations are expected in a sun-pointing THOR spacecraft.*

Particle moments To understand the physics of plasma heating at kinetic scales it is essential to measure particle moments of electrons and mass resolved ions (density, velocity and temperature) at their characteristic scales (**RS-7**,**RS-6**). Plasma density measurements are also critical for the identification of wave modes, the construction of wave dispersion relations, the identification of density gradients, all the key parameters required to understand the turbulent state of plasma. Therefore THOR shall resolve plasma density down to electron scales (**RS-7**). Plasma density measurement can be measured by different methods with their applicability depending on the plasma environment and temporal scale. It is important that THOR can use different methods, such as plasma frequency tracking, particle instrument integrals and satellite potential, to cover all required temporal scales and expected plasma parameters. Satellite potential measurements so far has allowed the highest time resolution measurement of plasma density, down to electron scales. However, for a spacecraft with spin plane close to the ecliptic, there are large variations in spacecraft potential during a spin (see Fig. 28). This prevents the use of the spacecraft potential for accurate estimates of density and density fluctuations. The sun-pointing THOR will not suffer from this problem, and can meet meet the science requirement.

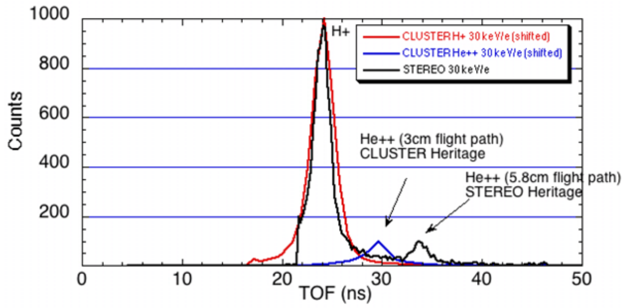

Figure 29: *A distribution of counts for H^{+} and He^{++} of Cluster/CODIF and Stereo/PLASTIC instruments. To resolve He^{++} a mass separation comparable to Stereo/PLASTIC is required (**RI-5**).*

Particle distribution functions summary THOR shall characterize mass resolved ion and electron populations in plasma allowing to resolve thermal and suprathermal parts of the distribution functions (**RS-5**,**RS-8**,**RS-9**), to understand e.g. what determines the observed ion/electron temperature ratio in a collisionless plasma turbulence [160,161] and the role of different wave damping mechanisms for the acceleration of suprathermal particles [162]. Table 3 compares the performance of some current and upcoming missions relevant to THOR science in terms of their temporal, angular, energy resolution of 3D particle distribution functions. The performance of current missions Cluster and WIND do not satisfy most of the THOR requirements. Solar Orbiter satisfies most energy/angular resolution requirements for pristine solar wind, but has inadequate temporal resolution. MMS satisfies improves on temporal resolution, except for electrons and He^{++}, and has insufficient angular/energy resolution to resolve pristine solar wind for ions. Summarizing, the combination of all THOR requirements on measuring particle distribution functions of thermal and suprathermal electrons and ions is not satisfied by any existing or upcoming mission.

Table 3: *3D distribution function resolution*

	Electrons			ions/solar wind			ions / sheath&shock			
	dt	dE/E	dθ	dt	dE/E	dθ	dt	dt_α	dE/E	dθ
THOR	**5ms**	**10%**	**5°**	**0.15s**	**5%**	**3°**	**0.15s**	**0.3s**	**10%**	**10°**
Solar Orbiter	1s	10%	10°	1s	7.5%	<2°				
MMS	30ms	17%	6°	0.15s	10%	5°	0.15s	10s	10%	5°
Cluster	4s	13%	5.6°	4s	18%	5.6°	4s	4s	18%	11°
WIND	3s	20%	5.6°	3s	20%	5.6°	3s		20%	11°

Best resolution of 3D distribution function measurements and their compliance with THOR instrument performance requirements. For angular resolution best value between polar and azimuthal directions is given. Green marks values that are compliant within 50% limit, red non-compliant values. Where no measurements are available are marked white.

Particle distribution functions examples We give a few examples motivating the THOR requirements on particle distribution function measurements. As an example for temporal resolution, Figure 30 shows that electron distribution function looks like heated bi-Maxwellian at ion scale while at electron scales show beams and non-isotropic core, indicating importance of resolving distribution functions at electron scales **RS-9**). This translates into requirements on temporal resolution of measurements of electron distribution function (**RI-9**). As another example for temporal resolution, recent studies comparing simulations with Helios observations of alpha particle temperature anisotropy in the solar wind revealed how the low time resolution of velocity distribution measurements can generate unphysical increase in perpendicular temperature, due to procedures of data sampling and averaging[163]. As an example for energy/angular resolution, Figure 31 shows that a beam in a simulation of solar wind turbulence is resolved only if the resolution in velocity space is sufficiently high (**RS-8**). This translates into requirements on energy/angular resolution of measurements of proton distribution functions (**RI-8**). This requirement is more severe in the case of drifting plasma, such as fast drifting pristine solar wind. For drifting plasmas the energy resolution dE/E required to resolve the distribution function scales roughly as the ratio of thermal velocity and drift velocity of the plasma population observed. This leads to two different requirements on energy/angular resolution within pristine solar wind and magnetosheath (**RI-8**). For the case of shock regions, it is required to resolve simultaneously the distribution function of both the fast drifting pristine solar wind and the thermalized sheath ions, including reflected and accelerated ions into the foreshock (**RI-8**). Similarly, drifting electron components, such as electron beam seen in Figure 30, put similar energy/angular resolution requirements on the electron distribution (**RI-9**). A number of turbulent energization mechanisms, e.g. stochastic ion heating and electron acceleration within coherent structures, suggest that often electrons are accelerated in the form of narrow suprathermal beams along the magnetic field while ions are heated in the perpendicular direction. This translates into the requirement to have higher angular resolution for electrons than for ions (**RI-9**). Finally, acceleration and heating mechanisms work differently for different ion mass species, as discussed in Section 2.3, translating into the requirement to resolve ions of different mass(**RS-5**). Figure 29 shows mass separation on some previous mission, illustrating that to resolve He^{++} THOR has to have mass separation comparable to Stereo/PLASTIC instrument (**RI-5**).

Energetic particles RS-11 To distinguish plasma heating from particle acceleration, the full distribution functions of energetic particles need to be measured. Traveling interplanetary shocks typically accelerate ions up to several MeV/nuc and electrons up to hundreds of keV, thus defining the upper end of the energy range to be covered by the energetic particle instrument. The lower end must overlap with the thermal plasma instrument to ensure the the respective fluxes are well cross-calibrated. Because the acceleration processes must ultimately be related with magnetic field variations, detailed pitch-angle distributions are required at typical time scales such as the proton gyroperiod at 1 AU which is approximately 10 s. In the case of THOR this means that pitch-angle distributions need to be acquired at sub-spin time resolution. To determine the influence of wave-particle interactions and detailed the spatio-temporal behavior of the acceleration process, 3-D VDFs shall be required once per spin.

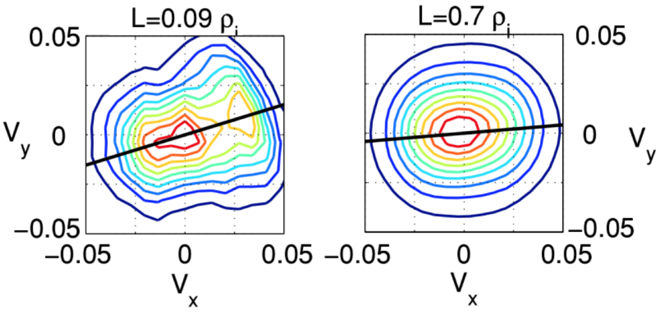

Figure 30: *Electron velocity distribution function in turbulence when averaged over electron scales (left) and ion scales (right). Physics of electron energization can be only resolved at electron scales*[27].

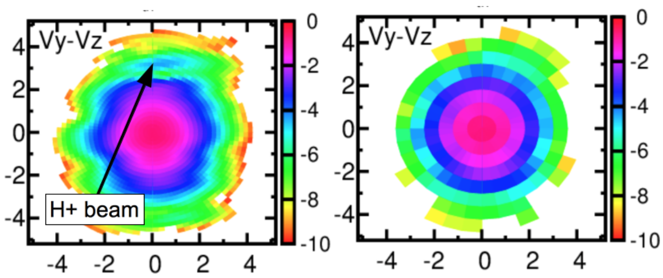

Figure 31: *Ion distribution functions in numerical simulations of turbulence shown with different velocity space resolution. On the left the velocity space resolution is high enough to resolve the proton beam which cannot be resolved with the velocity resolution right. The velocity resolution at the beam roughly corresponds to the THOR requirement of being able to resolve energies with dE/E values down to 10 (**RI-8**).*

3.2 Mission requirements

Table 6 gives the THOR mission success criteria.

Table 4: *THOR Mission requirements*

Mission Requirements - Orbit
RM-1 Orbit shall be optimized for satellite to spend long time intervals in the regions of main scientific interest as defined in **RS-12**.
RM-2 Orbit shall be optimized for maximum telemetry.
Mission Requirements - Operations
RM-3 It shall be possible to save on-board at least 10 days of high resolution data from which scientifically interesting time intervals can be selected for the transmission to the ground.
RM-4 Satellite payload shall operate in a way to maximize the data return from all the regions of main scientific interest as defined in **RS-12**.

Orbit requirements The large difference between turbulent plasma state in an undisturbed solar wind in comparison to close proximity to shock and astrophysical importance of understanding these differences requires that THOR spends long time intervals in the undisturbed solar wind (away from the foreshock), in the foreshock, at the bow shock, as well as in the magnetosheath (**RS-12**). There are no strict requirements on the orbital plane orientation, inclination or perigee values, except that bow shock region at the nose of the magnetosphere shall be covered during some part of the mission. However, to increase the science output from the mission it is preferential to select such orientation and inclination that during the period when THOR is in tail, the time spent in the magnetotail current sheet is maximized. Perigee should be above 2,000 km, to avoid stability problems of lunar interactions and sensor contamination (observed on Cluster below about 800 km altitude).

Science operations Normally payload can generate much more data than can be downlinked to ground. Therefore there shall be capability to save data on-board and make selection of data intervals for downlink. This would allow to select exact intervals of science interest, such as shock crossings, solar wind intervals with particular parameters and large scale boundaries. To make selection process in a reasonable time there shall be capability to save high resolution data from payload from at least 10 days of operations (**RM-3**).

Comparison to other missions Table 5 shows the comparison of THOR with other existing and upcoming missions by analyzing which science measurement requirements different missions satisfy. In the comparison we include only missions that have been or will be able to cover at least some of the plasma regions which are focus of THOR. It is seen that only a few of the requirements can be satisfied by other missions, while satisfying all of the science measurement requirements as required by the science questions has not been so far possible by any of the missions.

Table 5: *Mission compliance with THOR science requirements (✔ - compliant, ✓ - partially compliant). Some missions compliant with two or less science requirements: ACE, Helios-1,2, Spect-R.*

Mission	Science Measurement Requirem.											
	Fields				Particles							
	RS-1	**RS-2**	**RS-3**	**RS-4**	**RS-5**	**RS-6**	**RS-7**	**RS-8**	**RS-9**	**RS-10**	**RS-11**	**RS-12**
THOR	✔	✔	✔	✔	✔	✔	✔	✔	✔	✔	✔	✔
Cluster	✓										✔	✔
MMS	✓		✔	✔	✔		✓		✓	✓	✓	✔
Solar Orbiter	✔	✔			✓						✓	✓
SPP	✓	✔			✓						✓	✓
THEMIS	✓										✓	✔
Wind	✓										✓	✔

Table 6

THOR mission success criteria
THOR will be **scientifically** successful when its data analysis has resulted in significant, qualitative and quantitative progress in understanding plasma heating and particle acceleration mechanisms in different turbulent plasma environments.
THOR will be **experimentally** successful when high quality Burst mode data have been returned from at least: • 50 quasi-parallel shock crossings, • 20 quasi-perpendicular shock crossings, • 100 h slow solar wind, • 50 h fast solar wind, • 50 h foreshock, • 100 h magnetosheath behind quasi-par shock, • 20 h magnetosheath behind quasi-perp shock,

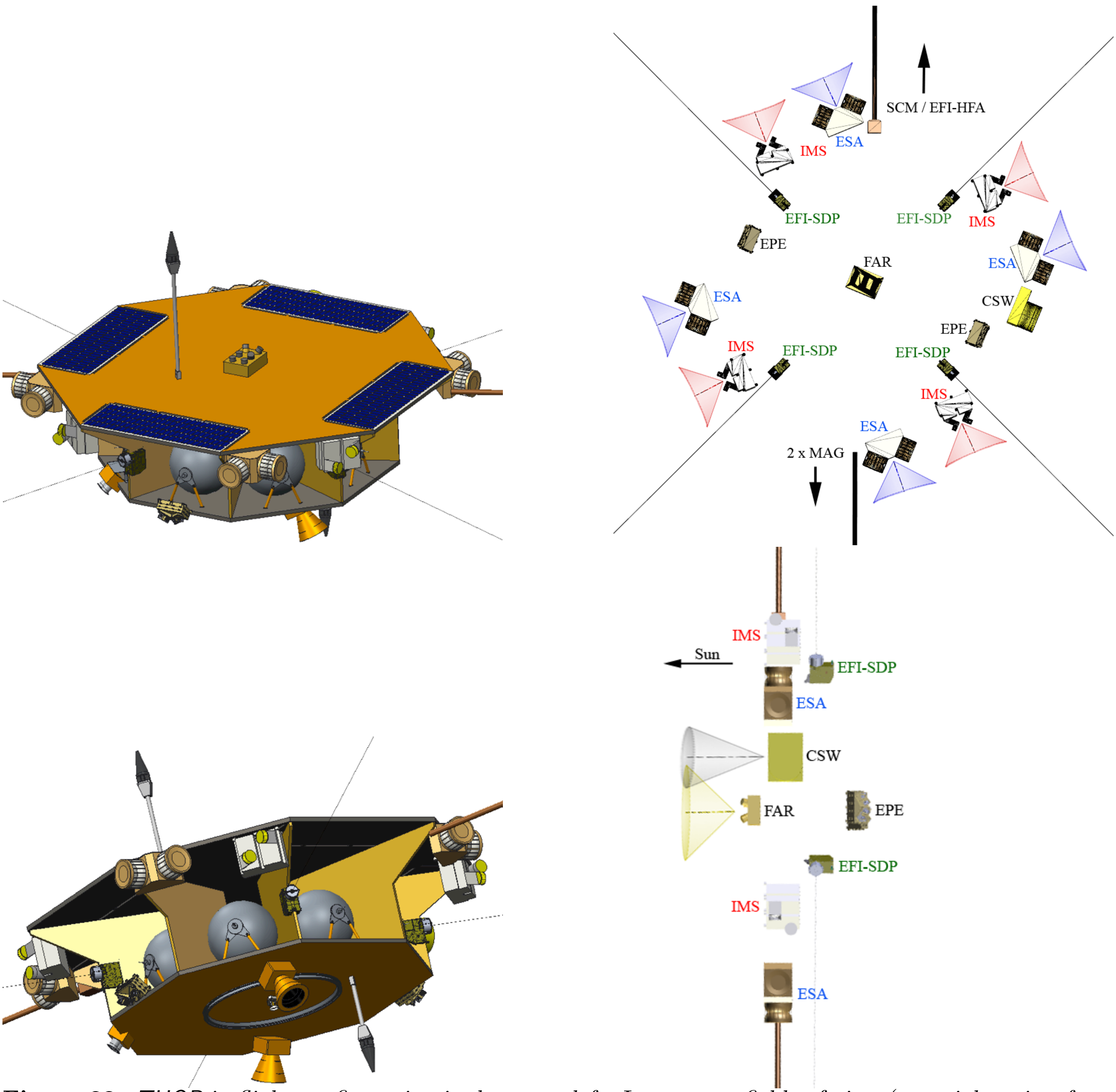

Figure 32: *THOR in-flight configuration is shown on left. Instrument fields of view (top, right: view from the Sun, bottom, right: view in a spin plane.*

4 Scientific payload

4.1 Payload summary

The THOR payload summarized in Table 7 is designed to fulfill the instrument performance requirements listed in Table 2. To satisfy the science requirements **RI-1** to **RI-4**, the THOR baseline model payload includes AC and DC magnetometers (MAG, SCM), four wire probe antennas and three orthogonal dipole antennas to measure DC and AC electric fields in 3D. All measurements from these electromagnetic field sensors will be processed by dedicated electronic modules contained within the FWP instrument box.

THOR will carry advanced particle instrumentation designed to enable very high time resolution measurements of particle distributions. A Faraday cup (FAR) measures the ion temperature and flow velocity to satisfy science requirement (**RI-6**), while the electron temperature and the density are derived from electric wave data produced by FWP. Ion and electron 3D particle distribution functions are measured using electrostatic analyzers (ESA and IMS). The IMS instrument will allow to separate individual ion species (**RI-5**) at very high time resolution (**RI-8**, **RI-11**). The ESA electron analyzer will sample the thermal electron distribution at a very high cadence (**RI-9**) and suprathermal electrons at a lower rate (**RI-10**). A dedicated instrument CSW will be included to provide high resolution optimized measurements of the drifting cold solar wind ions (**RI-8**). Data measured by the IMS, ESA and CSW analysers will be processed by a common digital processor unit (PPU) to reconstruct the particle distribution functions and compute moments (**RI-6**, **RI-7**).

Higher energy electrons and ions (**RI-12**) are monitored with a solid state detector (EPE) at a lower time resolution.

The baseline payload of THOR consists almost entirely of proven technology, with heritage from recent missions (e.g. Cluster, STEREO, RBSP) combined with newly-developed concepts already selected in the context of future missions (e.g. Bepi-Colombo, Solar Orbiter, MMS, Solar Probe Plus). Most of the units and building blocks of the payload have recent flight heritage and their performance, constraints and resource utilization are well characterized. Several potential enhancements of instrument baseline resolution are described in the respective instrument sections below and will be studied in phase A.

4.2 Instrumentation

The baseline THOR spacecraft has a sun-pointing spin axis ($<\sim10°$ from the Sun) and rotates slowly (nominal period is 30 s). The slow spin rate is primarily to reduce the fuel required to maintain the sunward-pointing attitude; the science requirements can be met over a broad range of spin rates. There is a strong heritage of using sun-pointing satellites for plasma measurements in near-Earth space (CRRES, Freja, RBSP) and there are no severe technological problems related to this choice. The important advantages of this choice given THOR's science requirements are discussed below. Fig. 32 shows a possible design of the THOR spacecraft with the instrument accommodation marked and Fig. 8 shows the mass and power budget of the proposed instrumentation.

The THOR scientific instrument suite will be funded by national agencies. Unlike on previous missions, the equipment for spacecraft potential control via ion beam emission, important for sensitive cold particle measurements, is not considered a scientific instrument, but a spacecraft service device to be procured by ESA.

4.2.1 MAG – DC magnetometers

Figure 33: *Fluxgate magnetometer developed for Solar Orbiter, providing heritage for MAG.*

MAG is a dual-sensor fluxgate magnetometer for measuring the ambient magnetic field. The design of the magnetometer consists of two triaxial sensors and the related magnetometer electronics, hosted on printed circuit boards in the common electronics box of the fields and wave processor (FWP).

The two sensors such as the ones show in Fig. 33 are placed along a solid boom, one at the end of the boom and the second at an intermediate distance along the boom, in order to enable reliable subtraction of any residual spacecraft magnetic field. Each sensor itself uses only two ring-cores to measure the magnetic field along the required three directions which enables proper sensor miniaturization. The magnetic field is sensed in the X and Y direction via separate ring-cores, while the Z direction is pick-up over both ring-cores.

The design of the electronics relies on a digitization of the AC output signal from the fluxgate sensor directly after a pre-amplifier. It follows the general

Table 7: *THOR science instrumentation.*

Instrument	Measured quantity	Range	Max. cadence	Requirements
MAG	Magnetic field	DC-50 Hz	128 sps	**RI-1**, **RI-2**, **RI-3**
SCM	Magnetic field	1Hz-200 kHz	524 ksps	**RI-1**, **RI-2**
EFI	Electric field	DC-200 kHz	524 ksps	**RI-1**,**RI-2**,**RI-4**,**RI-7**
FAR	Fast ion moments		32 sps	**RI-6**
FWP	Fields and waves		524 ksps	**RI-1**, **RI-7**
ESA	Electron distribution	1 eV–20 keV	5 ms	**RI-7**, **RI-9**, **RI-10**
IMS	Ion distribution	5 eV–32 keV	150 ms	**RI-5**,**RI-6**,**RI-8**,**RI-11**
CSW	Cold solar wind ions	5 eV–32 keV	150 ms	**RI-8**
EPE	Energetic particles	e^-: 20 keV–700 keV i^+: 20 keV–8 MeV	7.5 s	**RI-12**
PPU	Particle data products			**RI-6** to **RI-11**

*THOR science instrumentation: summary information on the range of measurement and resolution. Instrumental requirements addressed by individual instruments are shown here (note that **RI-13** applies to all instruments and is not included in the table).*

Table 8: *THOR Payload technical budget*

Instrument	Instrument type	Mass [kg]	Power [W]	TRL	Heritage/Note
MAG	Fluxgate magnetometer	1	3	8	BepiColombo, VEX
SCM	Search coil magnetometer	2.4	1	5	Cluster, MMS
EFI	2 x double probes, 3 x boom	13.2	3	5*	Cluster, RBSP, JUICE
FAR	Faraday cup	4.8	4.8	7	Spectr-R
FWP	EM field and wave receiver	7.2	19	5	Solar Orbiter, JUICE
ESA	Electron spectrometer	32.4	30	5	Stereo, Solar Orbiter
IMS	Ion spectrometer with TOF	28.8	34	6	Cluster, IBEX, MMS, Stereo
CSW	Electrostatic analyzer	8	10	6	Solar Orbiter
EPE	Solid state detector	4.8	5	6	Solar Orbiter
PPU	Digital electronics	7.2	25	5	Solar Orbiter
Harnesses		20			
Total (incl. DMM)		**133.8**	**134.8**		

THOR Payload technical budgets: Mass and power estimates for each individual instrument are current best estimates. A Design Maturity Margin of 20% has been applied to all mass and power estimates in the totals. For instruments with multiple units, mass and power totals include all units. Solid booms are not included in the instrument mass totals, although harness mass has been included for instruments on those booms (MAG, EFI and SCM). (*) EFI-SDP has TRL of 7, EFI-HFA has TRL of 5.

trend of a signal conversion from analogue to the digital domain as close as possible to the sensor(s). In this context, the replacement of analogue circuitry by digital processing in a Field Programmable Gate Array (FPGA) and an Application Specific Integrated Circuit (ASIC) improves the overall measurement stability, guarantees a precise timing of the field vectors relative to the system clock independent from selected range and sampling rate and it furthermore reduces the susceptibility of the system to electro-magnetic interference. The MAG electronics will be powered from regulated voltages provided by FWP power supply, MAG communication and telemetry will be routed via FWP data processing unit.

MAG will return magnetic field vectors at up to 128 sps, with a noise floor less than 0.006 nT/$\sqrt{\text{Hz}}$ at 1 Hz, which has been improved compared to previous mission such as Cluster. The noise floor of the proposed MAG sensor (based on Solar Orbiter engineering model) as can be seen in Fig. 37 in comparison to Cluster and the sensitivity of SCM. THOR MAG therefore provides high quality data with sufficient overlap with the SCM data to meet science requirements (**RI-2**).

MAG has two sensitivity modes (ranges) to adapt to the intensity of the magnetic environment along the THOR orbit. All baseline characteristics of MAG are given in Table 9.

To perform measurements with the declared noise level, MAG requires an appropriate magnetic cleanliness plan, as implemented on previous space missions (c.f. Section 5.3). Calibration of the instrument will be performed at existing facilities to fulfill the required accuracy of 0.1 nT (**RI-3**) along the lines used in previous missions.

Heritage and consortium structure: The

Table 9: *MAG technical parameters. All numbers include 20% design margin.*

Mass	0.8 kg (both sensors)
Volume	11 x 7 x 5 cm per sensor
Accommodation	Two sensors mounted on a boom. Electronics inside FWP box.
Power	3 W
Data products	B-field vectors
Range	±500 nT (low range) ±8000 nT (high range)
Measurement cadence	128 vectors/s
TM rate	5 kbps
TRL	7

MAG instrument will be developed by IWF Graz (PI: R. Nakamura) with a strong involvement from Imperial College London (Co-PI: S. Schwartz). The MAG team has been involved in the development and operation of a large number of high-quality fluxgate instruments like e.g. on Cassini, Cluster, Double Star and Venus Express. The fluxgate hardware for THOR is directly derived from the MMS and Solar Orbiter missions (Fig. 33) which are going to be launched in March 2015 and during 2017, respectively. In contrast with strict sensitivity requirements relevant for SCM, neither the required DC accuracy of 0.1 nT (**RI-3**) nor the required sensitivity below 10 Hz (**RI-2**) are unusual, and are met in-flight by the heritage instruments[164].

4.2.2 SCM – Search-Coil Magnetometer

The dual-band search coil magnetometer (SCM) is a triaxial magnetic sensor of inductive type. It is intended to measure three components of the magnetic field in the frequency range between 1 Hz and 200 kHz. It provides spectral information over that range and in addition delivers waveform measurements sampled at frequencies up to 524 kHz. It is composed of three dual-band magnetic antennas. Each antenna is made of a ferrite core with a first coil to perform the measurements in the LF range (below 4 kHz), and a second coil to perform the measurements in HF range between 1 kHz and 200 kHz. A mutual reducer is inserted to decouple the two windings. The mutual reducer is a cylinder made of a high permeability material (Fig. 34). Secondary coils are used as a flux feedback, to create a flat frequency response on a bandwidth centered on the resonance frequencies of the two main coils. This active part is potted inside an epoxy tube (400 mm long, external diameter 20 mm).

The magnetic antennas are assembled orthogonally in a compact configuration as shown in Fig 36. This mechanical support is made in a nonmagnetic material (PEEK KETRON) and stands for the interface with the satellite. The amplification electronic circuit is made in 3D technology (an option would be ASIC technology allowing for additional mass and power savings). It is divided into several printed circuit boards (PCB), which are stacked and molded in an epoxy resin. Tantalum layers are inserted between electronic boards to improve the radiation tolerance. It is composed of 3 HF amplification channels, 3 LF channels, and 1 power supply regulation circuit. The 3D module will be housed in the foot of the sensor foot (close to the antennas) to improve the signal to noise ratio.

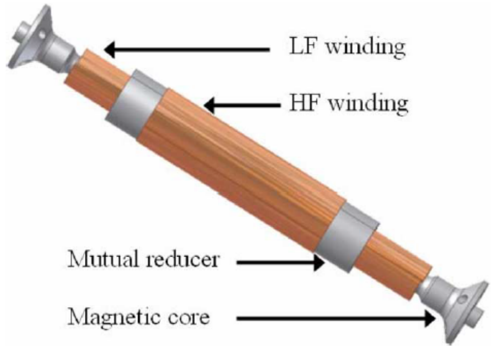

Figure 34: *A detail of a double-band search coil.*

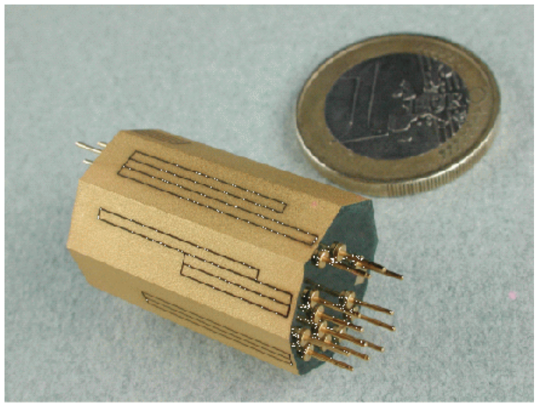

Figure 35: *Miniaturized preamplifier in radiation hard package will be used on SCM. A similar preamplifier is used on Solar Orbiter.*

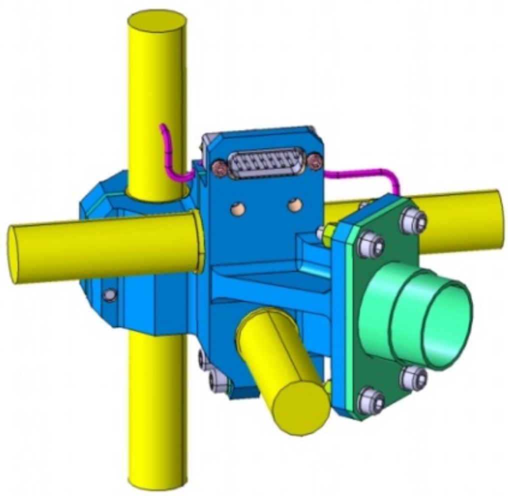

Figure 36: *CAD drawing of SCM including the mounting assembly.*

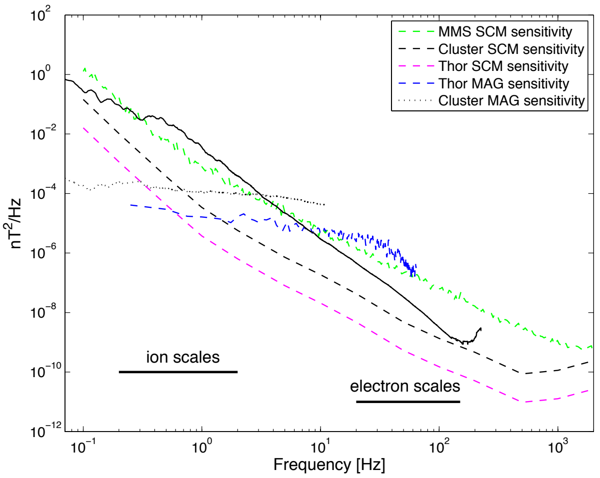

Figure 37: *Expected SCM sensitivity in comparison to the existing missions. Solid line shows a turbulence spectra in solar wind, measured by Cluster, when the turbulence amplitude is significant.*

Fig. 37 shows the sensitivity of search coil instruments on existing missions. With these instruments, the physics at electron scales in the solar wind can only be observed when the level of turbulence is high. The red line shows the expected THOR/SCM noise level. The increased sensitivity would satisfy requirement **RI-2** with good margin even in the solar wind also when turbulence levels are low. Mass increases associated with the increased coil length required to meet this target are partially offset by extensive miniaturization of the electronics already conducted in association with the MMS mission.

Heritage and consortium structure: The SCM instrument will be developed in collaboration of LPP in Paris (PI: F. Sahraoui) and LPC2E in Orléans (Co-PI: J.-L. Pincon). SCM has a long heritage since the concept has flown successfully on several missions such as Ulysses, Galileo, Cassini, Cluster,Themis, Double Star and Demeter. Others are currently built to fly on MMS, BepiColombo, Taranis, Solar Orbiter, Solar Probe Plus and JUICE. The double band antenna concept is already designed and manufactured for BepiColombo and TARANIS missions. While most sub-parts have a TRL of 9, the overall TRL is 5. This value is mainly constrained by the novel bi-band antenna and will increase after a successful launch of TARANIS and BepiColombo.

Table 10: *SCM technical parameters. Mass, power and telemetry include 20% design margin.*

Mass	2 kg
Volume	∼45 cm cylinders + base, whole assembly ∼40x40x50 cm
Accommodation	On a 5 meter boom.
Power	1 W
Data products	AC B-field analog signal
Bandwidth	LF: 1 Hz - 4 kHz, HF: 1 kHz - 200 kHz
TM rate	included in FWP TM
TRL	5 (most parts TRL 8–9)

4.2.3 EFI – Electric Field Instrument

EFI measures components of the electric field vector in space as the potential difference between two probes. In order to bring the probe-plasma voltage closer to zero, and to decrease the dependence of the probe voltage on fluctuations in the current due to ambient plasma, a bias current is applied to the probes. The EFI instrument measures the electric field vector in the frequency range 0–200 kHz (satisfying **RI-1**). EFI consists of two sets of sensors: Spin-plane Double Probes (EFI-SDP) providing high sensitivity DC electric field in the spacecraft spin plane (2D), and High-Frequency Antenna (EFI-HFA) providing 3D AC electric field at frequencies above ∼1 kHz.

EFI-SDP consists of 4 probes in the spin plane, extended on 50 m long wire booms, and thus measures two components of the electric field vector in the spin plane. The four EFI-SDP units are mounted at the side of the spacecraft so that the deployed booms form two orthogonal boom pairs. The EFI-SDP deployment will be performed during the commissioning phase; a steady spin rate exceeding a minimum value defined in phase A has to be maintained during the deployment so that the centrifugal force exceeds tension of the spring and probes will deploy safely. EFI-HFA consists of 6 cylindrical probes forming 3 orthogonal pairs having 2.5 m tip-to-tip. EFI-HFA is mounted on a boom, in such a way that all of the sensors have the same area facing the sun as well as the spacecraft.

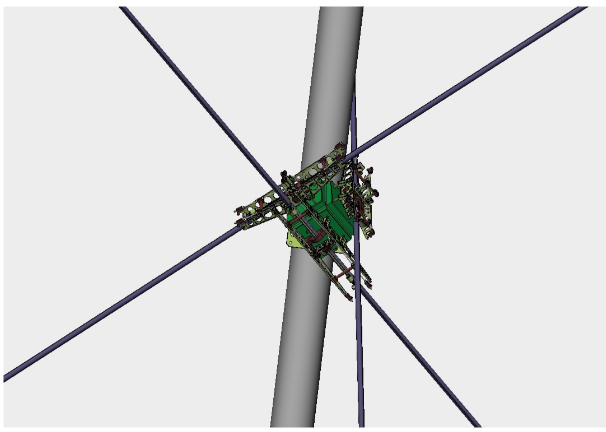

Figure 38: *A CAD drawing of the hinge assembly attaching the EFI-HFA antennas to the boom.*

As THOR spacecraft has a sun-pointing spin axis, EFI-SDP measures the electric field in the plane approximately orthogonal to the sun using long wire booms. The sun-pointing attitude greatly reduces errors due to wake effects and asymmetric photoelectron clouds, enabling the highly accurate ±0.1 mV/m (satisfying **RI-3**) near-DC electric field measurements. The increased accuracy and sensitivity (satisfying **RI-2**) can be seen in Fig. 27 and 41, which illustrate the use of different antennae and wire boom directions on Cluster, THEMIS and

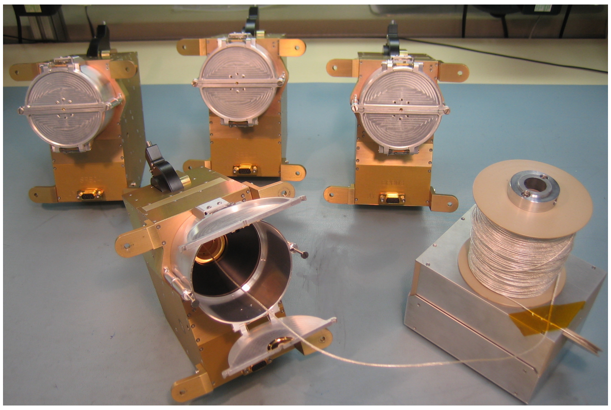

Figure 39: *The EFW instrument on RBSP provides heritage for EFI-SDP.*

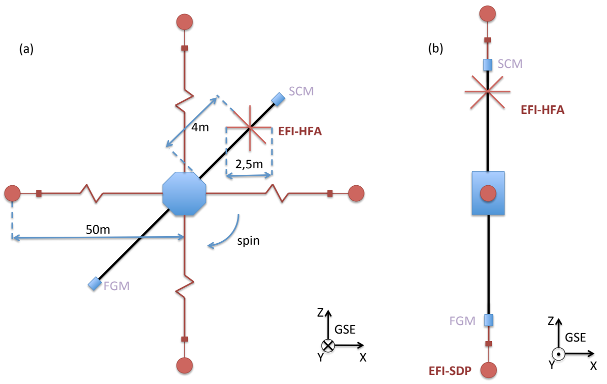

Figure 40: *A diagram showing the accommodation of EFI antennas on the spacecraft.*

MMS.

EFI-HFA measures the 3D AC electric field. The baseline of the EFI-HFA is much shorter than for the EFI-SDP making this measurement less sensitive, however the sensitivity is sufficient to resolve strong electric field fluctuations in the solar wind, shock and magnetosheath such as Langmuir, ion-acoustic and electrostatic solitary waves, for which large $E_{||}$ is expected and therefore 3D measurement is essential.

Most of the time EFI is run in E-field mode with constant bias current. Periodically a bias sweep is conducted in order to determine the I-V curve of the probes, which among others needed to determine the optimal bias current setting. EFI also measures the floating potential of the satellite, which can be used to estimate the plasma density at very high time resolution (up to a few hundred Hz). The sun-pointing attitude greatly reduces changes in the illuminated area, and hence the associated spin-dependent errors. In combination with densities derived from the observed plasma frequency emission line, EFI monitors the plasma density from DC to a few hundred Hz. The spacecraft potential will be provided via spacecraft data bus to PPU which will use it for onboard moment calculation.

An interferometry mode can be used to infer wavelengths and scale sizes at the smallest scales in the plasma, resolving electric field structures at Debye length scales moving with phase velocities up to ~20,000 km/s (satisfying **RI-4**). The highest time resolution time series data are collected during snapshots, both time triggered and event triggered, throughout the orbit. High frequency activity occurring between snapshots are monitored using power spectra computed on board. The frequency range of the snapshots and spectra covers the plasma frequency, and highly-accurate plasma densities are calculated by monitoring this plasma emission line.

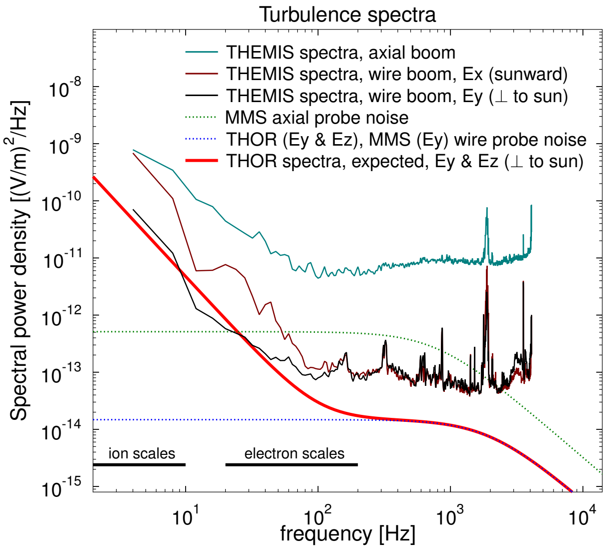

Figure 41: *Comparison of electric field spectra in the solar wind measured by wire and axial probes on THEMIS. Axial booms have significantly higher noise level. The signal of sun-pointing direction is contaminate by wake effects. THOR being sun-pointing will measure two high quality components of electric field perpendicular to the Sun-Earth line.*

Table 11: *EFI technical parameters. Mass, power and telemetry include 20% design margin.*

	EFI-SDP	EFI-HFA
Mass	11.2 kg	2 kg
Dimensions	4 spheres on 50 m wire	three orthogonal 2.5 m dipoles
Accommodation	In spin plane 90° apart	On SCM boom
Power	1.8 W	1.2 W
Data products	probe potential, 2D E-field	3D AC E-field
Bandwidth	DC–200 kHz	~1 kHz - 200 kHz
Range	±1 V/m	±0.5 V/m
TM rate	Included in FWP rate	
TRL	7	5

Heritage and consortium structure: EFI hardware is contributed by IRF, Uppsala Sweden (PI: Y. Khotyaintsev), Space Science Laboratory, UC Berkeley, USA (Co-PI: S. Bale) and SRC-PAS, Warsaw, Poland (Lead Co-I: H. Rothkaehl).

EFI-SDP builds on the heritage of double-probe instruments with long wire booms flown onboard RBSP and THEMIS, and which are similar to Cluster/EFW and MMS/SDP. The EFI-SDP boom units are based on RBSP and have TRL 7 (units will be exact copies or very similar to RBSP/EFW, but different mounting results in TRL 7). EFI electronic boards are based on MMS/FIELDS and SolarOrbiter/RPW/BIAS and have TRL 7. EFI-HFA antennas are based on JUICE/RPWI/RWI and have TRL 5.

4.2.4 FWP – Fields and Waves Processor

The Fields and Waves Processor (FWP) is a central electronics unit for all electromagnetic field measurements. This unit will interface with all fields sensors (EFI, MAG and SCM) and perform all tasks related to field data digitization and on-board processing. FWP box will house several data acquisition subunits, all sharing a common power supply and data processing unit and thus a single data and power interface to the spacecraft. The subunits of FWP are described in Table 12. The subunits will be integrated in a standard aluminium alloy electronics box. Internal interfaces (analog and digital) between the boards will be realized via backplane. FWP will implement a degree of fault tolerance via cold redundant DPU and power supplies and partial overlap of data acquisition modules, so in case of a failure of any single subsystem, the instrument can still fulfill its mission.

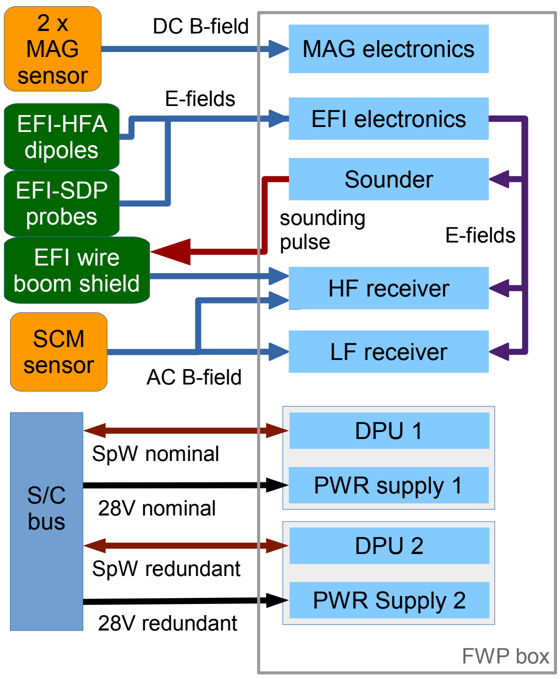

Figure 42: *Block diagram of the FWP instrument showing the subunits inside the box and connections to sensors and spacecraft.*

MAG and EFI electronics: The FWP box will house the electronics boards responsible for biasing of E-field antennas and E-field acquisition as well as the complete MAG electronics driving the MAG sensor and acquiring the data. These boards are considered parts of EFI and MAG and relevant information can be found in the respective sections 4.2.3 and 4.2.1.

The Thermal noise High frequency Receiver (THR) is a wave analyzer board responsible for spectral analysis and processing of signals from EFI antennas and SCM in the full frequency range up to 200 kHz. Digitization is performed via stacked ADC ASIC, under development by LESIA with the suport of CNES, reaching very high dynamic range (> 100 dB). THR will perform on-board spectral processing and thermal noise analysis which allows estimating absolute electron density and temperature from thermal noise spectra in the solar wind (**RI-7**), complementing ESA measurements. LESIA (Paris-Meudon) will be responsible for the delivery of the THR board. LESIA has a long heritage in the development of radio and thermal noise high frequency instruments (e.g. STEREO, Solar Orbiter, Bepi-Colombo, WIND).

The Low Frequency Receiver (LFR) is a wave analyzer board responsible for digitization and processing of signals from EFI antennas and SCM in the frequency range up to 20 kHz and waveform acquisition up to 200 kHz, fulfilling requirement (**RI-1**). The signal is then processed by integrated digital logic implemented in an FPGA, performing filtering, decimation and spectral analysis of the signals in order to reduce the telemetry volume. IAP has significant heritage in the development of wave analyzers for recent missions (Solar Orbiter, TARANIS, JUICE etc.). IAP Prague will be responsible for the delivery of the LFR board.

Electron Density Sounder (EDS) is an active experiment injecting oscillating signal on the shield of the EFi/SDP wire booms and measuring the response of the plasma in electric field. Analysis of plasma resonances then allows to obtain precise absolute measurement of electron density (**RI-7**) invaluable for particle instrument cross-calibration. Comparing to THR, EDS provides good estimates even in the presence of natural waves, but the active nature of the measurement perturbs other field measurements. EDS has to be run in a low duty cycle. EDS can also measure natural wave spectra, providing partial redundancy for HFR. University of Sheffield will be responsible for EDS and EDS heritage comes from Cluster WHISPER instrument.

The Data Processing Unit (DPU) is a central computer dedicated to controlling the units within the FWP box, receiving raw telemetry data from all FWP units, formatting and compressing the science data and transmitting them to the spacecraft. DPU software will also perform numerical calculations for producing spectral matrices and optionally particle correlation function from very high resolution data on-board (a feature to be studied in phase A). The board will include a powerful fault tolerant CPU (dual-core Leon3-FT), 128MB of memory, SpaceWire interface to the spacecraft and digital interfaces to other FPW subunits. As the FWP DPU represents a critical system for the entire mission,

Table 12: *FWP subunits.*

Acronym	Subunit name	Function	Responsible institute
MAG/ELB	MAG electronics board	MAG electronics	IWF Graz *MAG PI responsibilty*
EFI/HFB	EFI HF electronics board	E-field receiver for EFI/HFA	IRF Uppsala
EFI/LFB	EFI HF electronics board	E-field receiver for EFI/SDP with probe biasing	IRF Uppsala *EFI PI resposibility*
FWP/LFR	Low frequency receiver	Acquisition and processing of signals below 20 kHz	IAP Prague *PI: J. Soucek*
FWP/THR	Thermal noise and HF receiver	HF spectral measurements, on-board thermal noise analysis	LESIA, Paris *Lead CoI: M. Maksimovic*
FWP/EDS	Electron density sounder	Active measurement of plasma resonances	Univ. of Sheffield *Lead CoI: K. Yearby*
FWP/DPU	Data Processing Unit	TC/TM handling, wave-particle correlation calculation	IAP Prague
FWP/PSU	Power Supply Unit	Voltage conversion and power distribution	SRC-PAS, Warsaw *Co-PI: H. Rothkaehl*

two separate units in cold redundancy will be included in FWP box. IAP will be responsible for the delivery of hardware both DPU units. Flight software running in the DPU will be developed by IRF in Uppsala.

Power Supply Unit (PSU) is a DC-DC power converter providing stabilized low voltages to all subunits. The PSU will include a digitally controlled power distribution unit with the ability to power on or off any subunit independently, secondary current and voltage monitoring as well as overcurrent protection. Two separate units in cold redundancy will be included in FWP box. SRC-PAS in Warsaw will be responsible for the development and delivery of PSU hardware. The SRC-PAS has a strong heritage in power supply design for various space instrument including JUICE, TARANIS, Bepi-Colombo, Venus Express, Mars Express and other space instrumentation. The power supply will be designed with EM cleanliness in mind - switching DC-DC converters will be crystal controlled and synchronized.

Summary technical parameters of FWP are given in Table 13. FWP will be built by a consortium of several institutes (see Table 12). The IAP in Prague will lead this consortium.

Table 13: *FWP technical parameters. Mass, power and telemetry include 20% design margin.*

Mass	6 kg
Volume	22 x 14 x 32 cm
Accommodation	SC instrument platform
Power	19 W
Data products	E/B spectra, waveforms, wave-particle correlations, plasma parameters
Cadence	up to 524 ksps
TM rate	up to 800 kbps
TRL	5

4.2.5 FAR – Faraday Cup

The Faraday cup instrument (FAR) is a fast monitor of solar wind parameters based on simultaneous measurements of the total ion flux and ion integral energy spectrum by six identical Faraday cups (FCs) with collectors split into two halves. From this combined measurement, it is possible to determine basic solar wind ion parameters: density, three velocity components, and temperature (**RI-6**).

We intend to use two FCs for a determination of the two flux directions. Third FC will measure the ion distribution function within 1–3 s and the ratio of alpha particle and proton densities can be determined with this cadence. Collector currents of other FCs serve as a proxy of the moments of the ion energy distribution and these moments can be determined (in a Maxwellian approximation) on the ground with the resolution determined by the FC geometrical factor and telemetry rate; A sampling rate of 32 Hz is expected satisfying the requirement **RI-6** with a sufficient margin.

Figure 43: *A photograph of the predecessor of THOR FAR instrument: the BMSW solar wind monitor for the Spectr-R spacecraft.*

In the THOR configuration, each FC is equipped with four grids: grounded grids cover outer and inner diaphragms that define the angular characteristics; a positive control grid is placed equidistantly from outer and inner diaphragms; and a suppressor grid lies between the inner diaphragm and a collector. The grounded grids are used for an elimination of an internal electric field outside FC. The control grid is connected to a tunable high voltage source and thus, only the ions with the velocity sufficient to overcome the grid potential can reach the collector. The suppressor grid is powered by a negative potential of ≈ -300 V. This potential returns back photoelectrons emitted from the collector by a solar UV radiation as well as solar wind electrons. The value of the suppressor grid potential is sufficient for precise measurements in a plasma with the electron temperature up to ≈ 100 eV, i.e., for the solar wind and near night-side magnetosheath. The electron component of the collector current caused by photoelectrons from the suppressor grid should be subtracted from the total measured current. This point is important for a precise determination of solar wind parameters. The estimations from previous missions have shown that this photocurrent is roughly equivalent to the proton number flux of the order of 10^{-9} cm^{-2} s^{-1}, i.e., about 30% of the nominal solar wind flux.

In comparison with the heritage instrument (BMSW on Spektr-R spacecraft), all THOR FCs are oriented approximately along the Sun-Earth line, they are equipped with splitted collectors and the dimension of the entry window (34 mm) is enhanced, thus the angular characteristics cover large angles and the instrument noise will be lower. Moreover, both main modes of the BMSW instrument (i.e., so-called sweeping and adaptive modes[165]) will work simultaneously on THOR. During the flight, one FC can be used for a permanent determination of the alpha particle parameters.

The sensor axis needs to be approximately aligned with the solar wind flow. On THOR the FAR instrument will be placed in the center of the from side of the spacecraft - the sun-pointing alignment of the spacecraft will ensure optimum orientation for the solar wind and foreshock regions and acceptable measurements will be made in the flank magnetosheath. FAR will not be able to operate efficiently in dayside magnetosheath regions where plasma flow is strongly deflected away from sun-earth direction.

The power spectral density of the solar wind turbulence at the upper end of the ion kinetic scale is expected to be up to ten orders of magnitude lower than that at the beginning of the MHD scale ($\approx 10^{-5}$ Hz), thus the amplitude of fluctuations should exceed the instrumental and statistical noises and it requires large geometrical factors

To facilitate in-flight calibration and to increase the instrument reliability, we expect 6 unified FCs equipped with identical front-end electronics (amplifiers, HV supplies). This design allows a determination of photocurrents, inter-calibration of sensors as well as the instrument reconfiguration (swapping of individual FCs) in the case of a failure of a part of the instrument. The conversion of FC currents into physical units uses the computer model of sensors and the values of photocurrents and detector sensitivities gained during intervals of the in-flight calibration. FAR is able to real-time provide on-board processed moments with reduced accuracy to other THOR instrument (such as CSW).

The instrument can measure ion density up to 150 cm^{-3}, ion velocity from 100 to 700 km/s, and ion thermal speed between 5 and 200 km/s. The control of the instrument consists of three types of modes of commanding: calibration, changes of the data rate, and changes of instrument configuration. The baseline characteristics of the instrument are listed in Table 14.

Table 14: *FAR technical parameters. Mass, power and telemetry include 20% design margin.*

Mass	4.8 kg
Volume	29 x 21 x 12 cm
Accommodation	On the sun-facing side of the spacecraft.
Power	4.8 W
Data products	ion density, velocity, temperature
Cadence	H^+: 32 ms, He^{++}: ~ 1 s
View angle	$\pm 50°$ from sunward direction
TM rate	13 kbps
TRL	7

Heritage and responsibilities: FAR for THOR is based on the BMSW instrument (Fig. 43) operating nominally onboard the Spektr-R spacecraft since the launch in 2011. FAR instrument will be developed by Charles University in Prague where the BMSW instrument was developed. The PI of the instrument will be Z. Němeček.

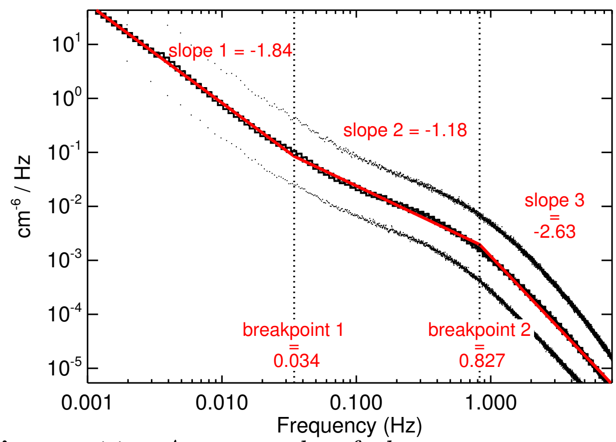

Figure 44: *An example of the power spectrum of solar wind density fluctuations from BMSW instrument on Spectr-R. The red line shows medians, black segments the first and third quartiles. This figure demonstrates the ability of FAR to observe the turbulent cascade in its entire frequency range. Adapted from Šafránková et al., Solar wind density spectra around the ion spectral break, submitted.*

4.2.6 CSW – Cold Solar Wind Ions

The CSW instrument will measure the three-dimensional velocity distribution functions (VDFs) of the cold solar wind ions at the cadence of 150 ms, a time resolution never achieved before in this region, addressing the requirement **RI-8**. It will provide measurements complementary of the Faraday Cups (FCs), which have higher cadence but cannot provide full 3D VDFs.

CSW can be divided into two main units: the detector unit and the electronics unit. The detector unit first comprises entrance deflectors which allow to sweep over angles ±21° out of the main detection plane (3° angular resolution). Deflected ions are then subject to energy-per-charge (E/Q) selection through a classic top-hat electrostatic analyzer. Through this analyzer the E/Q selected ions are focus onto microchannel-plates (MCP) in chevron stack, which allow a 10^6 gain in charge, collected on anodes. The MCPs define the main detection plane. Anodes in this planes are sectorized (16) to achieve a 3° resolution in the range ±24°. The electronics unit comprises a set of electronics boards that provide the required instrument functionality. The first board, onto which the anodes and MCPs are mounted, will also perform the signal amplification function through the use of a 16-way ASICs (an incremental development based on heritage of Solar Orbiter). High-voltage boards will be devised to control both the electrostatic analyzer voltage sweeps and the entrance deflector sweeps. The counting and data acquisition will be performed in an FPGA board. Finally, the electronics unit will contain a power and low voltage board.

The CSW instrument will be accommodated on the side of the spacecraft with a clear sunward field-of-view (FOV).

In order to achieve the science requirements, CSW will provide 3D velocity distribution functions at the high cadence of 150 ms and with an energy resolution of 5-8 %. The VDFs will have an unprecedented 3° resolution in both elevation and azimuth, thanks to fine anode sectoring and fast deflector sweeping. Electrostatic analyzer voltage sweeps will also be twice faster than typical. To achieve these goals, CSW will have an overall geometric factor of order 4 times higher than previous instruments (e.g., Proton and Alpha Sensor on Solar Orbiter). Volume (owing to high geometric factor) and power consumption (owing to fast sweeps) are thus relatively large comparing the similar previous instruments (cf. Table 15). CSW instrument might use averaged solar wind speed data received from the FAR instrument to optimize the tracking of solar wind flow (to be analyzed in phase A).

Heritage and consortium structure: The CSW PI institute will be IRAP (Toulouse, France), with significant contribution from BIRA (Brussels, Belgium). The PI is B. Lavraud (IRAP) and the Co-PI is J. De Keyser (BIRA). IRAP will provide all parts of the detector unit as well as the detection/amplification and high-voltage boards. BIRA will provide the FPGA and Power/LVPS boards as well as the mechanics for the electronics unit.

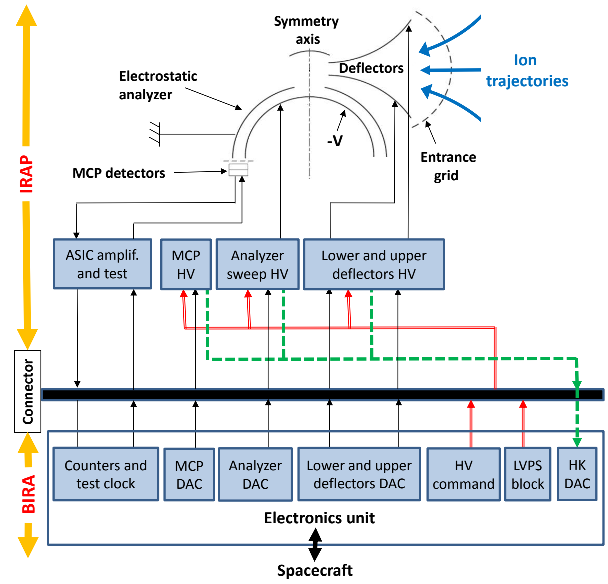

Figure 45: *A block diagram of the CSW instrument, showing responsibilites of IRAP and BIRA.*

Table 15: *CSW technical parameters. Mass, power and telemetry include 20% design margin.*

Mass	8 kg
Volume	35 x 25 x 25 cm
Accommodation	On sun-facing side of spacecraft
Power	10 W
Data products	3D ion distribution
Energy range	200 eV - 20 keV
Cadence	150 ms per 3D VDF
TM rate	∼ 170 kbps
TRL	6

4.2.7 ESA – Electro-Static Analyser

Modern electrostatic analysers utilise a top-hat design which has a narrow field of view in one (azimuthal) angular dimension, while in the other (polar) dimension the instantaneous analyser field of view can be up to 360°. A single such electron analyser, needs a time of order a spacecraft spin period to acquire a full 3D VDF. For the THOR spacecraft, this cannot satisfy the electron measurement requirements and high time cadence 3D VDFs can only be achieved by mounting several analysers around the spacecraft. Moreover, in order to keep the amount of hardware realistic while also providing the required azimuth angular resolution, we enhance these with electrostatic aperture deflection systems (ADS, Fig. 46) which allow each analyser to look in several directions in quick succession. We plan to meet the ESA requirements using 8 such analyser heads with instantaneous polar field of view 180°, which will be packaged as 4 pairs for more efficient use of spacecraft resources (Fig. 47), as will also be deployed on the NASA MMS spacecraft. The combined heads provide complete 4π steradians solid angular coverage during a time period defined by the time to measure across the consecutive ADS settings. Electrons from a selected azimuth and energy are deflected into the top-hat analyser by applying the appropriate voltage across the ADS deflectors. Within the top-hat, electrons are selected in energy by the applied voltage across the concentric hemispheres. Electrons which reach the detectors (MCP or CEM) are recorded. It is essential to synchronize the changes in the voltages applied to the ADS deflectors and analyser hemispheres and to change these voltages accurately at very high rates in order to sweep through the sensor energy range and cycle through the ADS deflection angles. With the current design, it is not practical to use fewer sensors with wider ADS azimuth range, as the highest energies we need to measure cannot be deflected through such large angles, and the count accumulation times would need to be reduced further.

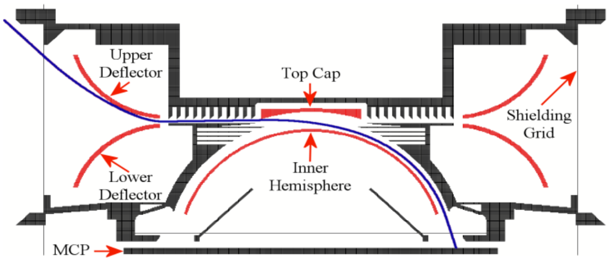

Figure 46: *Top hat analyser with aperture deflection*

Each of the 4 dual head electron analysers described above must be mounted with its wide (polar) field of view in the plane containing the spin axis and perpendicular to the spacecraft surface, in order to achieve the fast measurement rates and to minimise the entry of low energy electrons originating from the spacecraft.

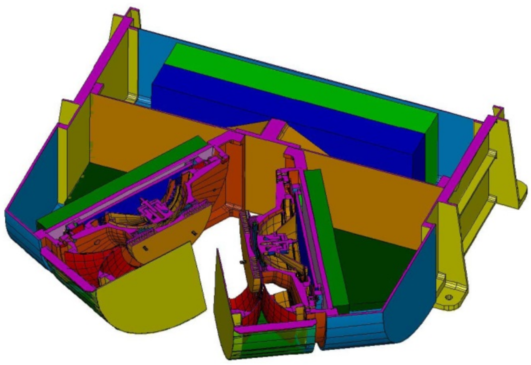

Figure 47: *Dual-ADS analyser sensor unit*

To meet the science requirements (**RI-10**), the sensors described above will be designed to be able to cover the energy range 1eV to 30 keV, with an energy resolution of up to 10%. The azimuthal angular coverage of the combined sensor suite will be 360° with each sensor covering ±22.5° with up to 5° resolution, while in the polar direction each sensor will cover 0 to 180°, again with up to 5° resolution. Note however that telemetry rates and counting statistics will likely not allow the instrument to be usefully used with the highest resolution and/or ranges in all dimensions. For example in order to make measurements at the highest required time cadences (5 ms for a 3D distribution - as required by (**RI-9**)) the measurements will need to be made over a narrower energy range and/or at lower energy or angular resolutions. Similarly, high angular resolution measurements will require accumulation of counts over longer time periods.

As indicated above, the sensor suite will have to operate in one of a number of science modes depending on the science measurement priority (e.g. high time resolution modes, high angular resolution modes, etc). In addition, a number of engineering modes will be available in order to monitor and ensure the absolute and relative calibration of the 8 sensor heads within the package. The raw data product from the sensors is a set of electron counts over a given time period within a given energy and angular range. This raw data from each sensor will be transmitted to the particle suite DPU (PPU), in which it will be reassembled to form a complete 3D velocity distribution function and used to calculate on-board moments (**RI-7**).

Heritage and consortium structure: The 4 ESA dual head sensors will be designed and built by a consortium consisting of UCL/Mullard Space Science Laboratory (MSSL) in the UK and NASA/Goddard Space Science Laboratory (GSFC) in the USA. Under this arrangement the PI of the sensor suite will be Prof. C. J. Owen (MSSL) while Dr. C. J. Pollock (GSFC) will act as co-PI and NASA PI. ESA instrument design builds on the heritage of both teams in the development of electron instruments for previous missions including Cluster, Solar Orbiter and MMS. Note that we anticipate that there may be technical overlap with certain sensor subsystems deployed on the other particle instrumentation proposed for this mission. A task for the study phase should be the identification of such subsystems with a view to minimising duplicate development. It may therefore prove to be the case that a broader network of hardware partners will develop for the build phase.

4.2.8 IMS – Ion Mass Spectrometer

The sensor combines energy per charge selection with a time-of-flight (TOF) measurement to determine three-dimensional distribution functions of ions with given mass per charge over the energy range 5 eV/q to 40 keV/q and a mass range of 1-32 amu. The mass-per-charge resolution is

Table 16: *ESA technical parameters. Mass, power and TM numbers include 20% design margin.*

Angular resolution	down to 5°
Energy resolution	down to dE/E = 10%
Mass	32.4 kg (all 4 units)
Volume	40 x 40 x 20 cm per unit
Accommodation	On the side of the spacecraft. Units separated by 90°.
Power	30 W
Energy range	1 eV - 30 eV
Data products	electron VDF
Cadence	down to 5 ms
TM rate	up to ∼ 4.5 Mbps
TRL	5 (electronics 6)

$(m/q)/(\Delta m/q) > 8$ to resolve H^+, He^+, He^{++} and O^+ (**RI-5**). This design was used successfully on Cluster/CODIF, Fast/TEAMS, Equator-S/ESIC, Stereo/PLASTIC instruments and will be used on BepiColombo/MSA.

The 3D distribution functions of main species will be measured with the following time resolution: $H^+ \sim 150$, $He^{++} \sim 300$ ms and O^+ with lower cadence (**RI-8**, **RI-11**). Moments of the distribution function will be obtained from 3D distributions (**RI-6**). This resolution will be obtained by strategically mounting 4 double-head units on the spacecraft. Each single-head consist of one electrostatic analyzer (top-hat) to capture ions over ±22.5° in elevation while covering 180° in azimuth, so that 4π steradian will be covered instantaneously by the 4 double-heads mounted on the side of the spacecraft and phased by 90°, similarly to MMS/FPI instrument. Fig. 48 shows one THOR double-head unit.

A longer TOF chamber ∼ 6.5 cm (compared to ∼ 3.5 cm on Cluster) will be used to better separate H^+ from He^{++} (**RI-5**), as done for STEREO/Plastic (Fig. 29). Improvement in the MCP configuration with respect to Cluster/CODIF will also give better stability and long-term efficiency.

A schematic illustrating the functional principles of the design, is shown in Fig. 49. There are three main structural elements to the IMS: the electrostatic analyzer, the time-of-flight section, and the electronics box. Ions entering the sensor are selected by energy per charge by the electrostatic analyzer. At its exit, ions are accelerated to 15 keV/e (nominal post-acceleration) and then enter the TOF system. Ions pass through the thin carbon foil. Electrons knocked off the foil are steered to the inner micro-channel plate (MCP) providing the "start" signal. This signal is also used to determine the ion entrance position. Ions continue through the foil and hit the outer MCP to give a "stop" signal.

Electrostatic Analyzer: The design of the electrostatic analyzer for each single head is based on heritage from BepiColombo/MSA however electrostatic deflection will be included similarly to MMS/FPI. The field of view (FOV) of each single head is 45° x 180° with angular resolution 11.25° in azimuth and 9° in polar direction (5 deflection steps) (**RI-8**, **RI-11**). The energy range is 5 eV/q to 40 keV/q scanned over 128 energy sub-steps, resulting in 32 main energy steps, so that each elementary measurements (1 energy, 1 angle) is done over ∼ 1 ms. A full scan of FOV will be done over ∼ 150 ms. The energy resolution is $\Delta E/E = 10\%$ (**RI-8**, **RI-11**). The geometrical factor $G \sim 2 \cdot 10^{-4}\,\mathrm{cm^2\,sr\,eV/eV}$ (all efficiencies included) will be electrostatically adjusted using a flux controller ("spoiler") to avoid saturation in the solar wind. Two top-hat sensors will be mounted on each double-head unit as shown in Fig. 48 to obtain a field of view of 90° × 180° per double head and thus full 4π for the IMS instrument. An alternative measurement strategy could be used, by combining each pair of single heads into a single analyzer that provides a FOV of 90° x 360° by looking simultaneously in opposite directions and deflecting in each direction by ±22.5°. Four such analyzers would be mounted on the side of the spacecraft and will be phased by 90° as for the baseline measurement strategy. This alternative strategy would allow reducing the complexity of the instrument with also some possible saving in mass/energy, and is a task for the study phase.

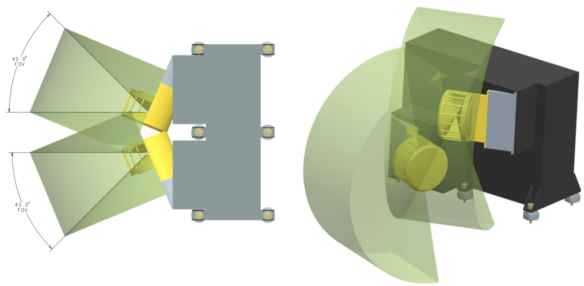

Figure 48: *A CAD drawing of the IMS double-head unit and its field of view.*

Time-of-Flight Section: At the entrance to the TOF section are the thin (2-3 μg/cm^2) carbon foils. The carbon foil support grids and support structure are based on designs used for Cluster/CODIF, Fast/TEAMS, Stereo/PLASTIC and IBEX-LO (all build at UNH). The TOF optics assembly is based on the designs for Cluster/CODIF but with a longer flight path similar to the one of Stereo/PLASTIC (**RI-5**). The start anode is divided into angular sectors used to determine the incoming angle. The electrons are focused to the center of these positions. This type of electron azimuthal focusing is the same as used on Cluster/CODIF and with the longer flight path in Stereo/PLASTIC.

The MCP configuration is modified from the Cluster/CODIF design. In the heritage design, the MCPs are located in the high-voltage section of the instrument. The amplified current from the MCP then crosses the high voltage gap to an anode at ground potential. Improvements for the IMS detector will be made from lessons learn from Cluster and

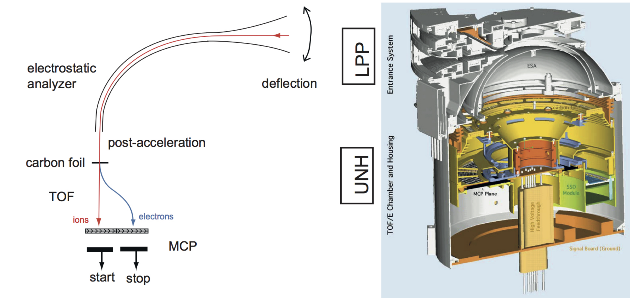

Figure 49: *Left: a schematic demonstrating the principle of operation of the of the IMS instrument. Right: Cutaway view of the Stereo/PLASTIC entrance System and TOF chamber. Adapted from*[166]

Stereo.

Electronic subsystems: The electrical subsystems of IMS consist of an analog and a digital board, a high voltage power supply board, a high voltage stepping power supply for the electrostatic analyzer, and a low voltage power supply. All these components have heritage from previous missions such as CLUSTER, STEREO, IBEX, FAST, BepiColombo and MMS.

Consortium structure: The IMS instrument will be provided by a consortium of several institutes lead by the Laboratoire de Physique des Plasmas (LPP), Paris (PI: A. Retinò) with a large contribution by the University of New Hampshire (UNH) (Co-PI: H. Kucharek). The LPP will be responsible for the electrostatic analyzers and for the detection electronics while the UNH will be responsible for the TOF section. ISAS/JAXA, Tokyo and MPS, Göttingen will provide smaller hardware contributions in terms of MCPs and electronic components.

Table 17: *IMS technical parameters. Mass, power and TM numbers include 20% design margin.*

Angular resolution	10°
Energy resolution	down to dE/E = 10%
Mass	28.8 kg (all 4 units)
Volume	16 l per unit
Accommodation	On the side of the spacecraft. Double-head units separated by 90°.
Power	34 W
Energy range	5 eV/q - 40 keV/q
Data products	ion VDF (H^+,He^+,He^{++},O^+)
Cadence	H^+: 150 ms, He^{++}: 300 ms
TM rate	$\sim$ 2.5 Mbps
TRL	6

4.2.9 EPE – Energetic Particle Experiment

The Energetic Particle Experiment (EPE) on-board THOR is a particle instrument measuring the energy spectra and angular distributions of energetic electrons (20-700 keV) and ions (20-8000 keV/n) as needed to fulfill requirement **RI-12**. The instrument has two sensor units, each one measuring with two double-ended telescope pairs in four viewcones. Utilizing the spin of the spacecraft, EPE observations cover the full sky.

The two ends of the telescopes observe electrons and ions, respectively. Each telescope consists of a stack of three solid-state detectors. On one end, the stack is covered by a thin parylene foil, stopping ions below a few hundred keV/n but letting electrons pass almost unaffected. The uppermost detector (500 μm thick Si) on this side is operated in anticoincidence with the second and, thus, observes the energy spectrum of electrons stopping in the detector. The other end of the telescope has no foil but instead a broom magnet that deflects electrons below a few hundred keV. This side of the telescope has a 20 μm thick Si detector followed by a 500 μm Si detector, which thus form an ion telescope observing at energies from 20 keV to 8 MeV/n. Ions passing the the first detector can be identified using the ΔE vs. E technique, which enables the separation of ions heavier than hydrogen from protons and CNO from He at energies above 300-400 keV/n. Full elemental resolution is achieved in the MeV/n energy range.

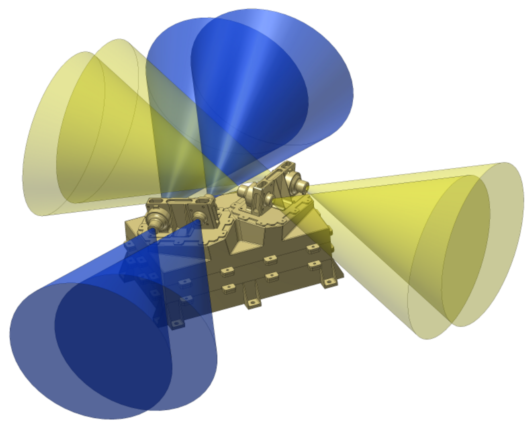

Figure 50: *A CAD drawing of one of the two EPE units showing instrument field of view.*

Each of the two identical EPE units integrates the sensors and electronics in a single package. Each unit has an independent SpaceWire and power interface to the spacecraft, providing partial redundancy and ensuring that data (albeit degraded) will be available in case of failure one EPE unit.

The EPE instrument collects the full 3D distribution of all particles in one half of the spacecraft spin period (every $\sim$ 15 s). The relative orientation of the 8 independent telescopes was conceived to enable good quality sub-spin measurements for most magnetic field configurations. Cuts of the VDF in 8 directions are available every $\sim$ 2 seconds and on average, it will be possible to recover a full pitch angle distributions of energetic ions and electrons every 7.5 seconds.

Pre-flight ground energy calibration (1% level) of all detector elements, on-axis active area calibration, selected off-axis directions active area calibra-

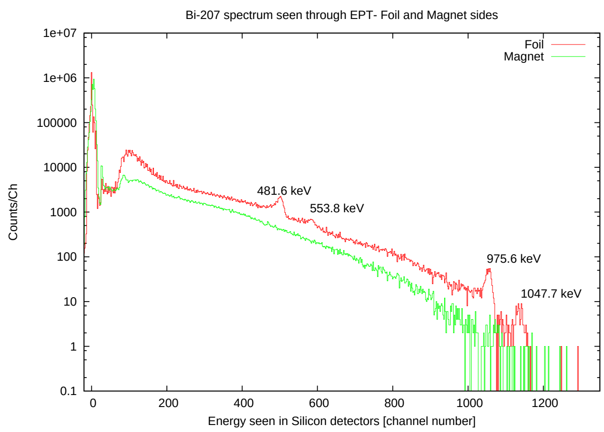

Figure 51: *Bi-207 spectrum measured by EPE prototype. The red curve (electron measurement) shows the peaks corresponding to the characteristic energies of Bi-207 decay. No peaks are seen in the green curve (proton channel) indicating a good separation of electrons and protons up to nearly 1 MeV.*

tion and dead-time calibration will be performed. Calibration quality will be monitored in-flight using measured data and cross-calibration with suprathermal electron/ion instruments. Most of the required calibration facilites are in-house at CAU.

Table 18: *EPE technical parameters. Mass, power and telemetry include 20% design margin.*

Angular resolution	45 degrees
Energy resolution	dE/E = 25%-50%
Mass	4.8 kg (both units)
Volume	20 x 20 x 20 cm (each unit)
Accommodation	On the side of the spacecraft. Two units separated by 90°.
Power	5 W
Energy range	e-: 20-700 keV i+: 20-8000 keV
Data products	particle VDF
Cadence	15s for 3D VDF 7.5s for pitch angle VDF
TM rate	13 kbps
TRL	6 (most parts TRL 7-8)

Heritage and consortium structure: The EPE instrument will be lead by the University of Kiel (PI: R. Wimmer-Schweingruber) with a contribution of University of Turku (Co-PI: R. Vainio). EPE combines heritage from Solar Orbiter EPD, STEREO/SEPT, and SOHO/ERNE instruments.

4.2.10 PPU – Particle Processing Unit

The PPU provides a single power, telemetry, and control interface to the spacecraft as well as power switching, commanding and data handling for IMS, CSW and ESA. The approach of a common processing unit for these particle instruments permits to facilitate technical, programmatic and scientific synergies and enables an integrated and coherent management for correlative plasma measurements. Moreover, it offers the possibility to optimize and save spacecraft resources and also to facilitate inter-operation with other instruments on the spacecraft. More in detail, the PPU will perform the following tasks: Receive/Transmit commands from S/C; drive instrument operational modes; acquire and process data from the instruments; download science and telemetry data through the S/C interface (SpaceWire); distribute primary power supplies to sensors. It functionality is essential to operate the particle payload and to fulfill requirements **RI-6** to **RI-11**. The PPU will be able to manage IMS, CSW, and ESA simultaneously in all the foreseen modes of operation.

As far as the data processing is concerned, the PPU will have to deal with the three-dimensional particle distribution functions of ions and electrons. Starting from the measured 3D particle distributions the PPU will compute moments and quality parameters. Afterwards, whenever required, it will compress the 3D distribution with a loss-less compression algorithm. An optional feature of PPU to be studied in phase A is a direct digital link between PPU and FWP data processing unit, which would allow providing real-time particle data (such as individual particle impacts) to FWP where it would be used by for wave particle correlation calculation.

The foreseen PPU architecture will be based on a dual-core LEON3FT CPU ASIC and a number of FPGA based HW accelerators (see 52). It will have a fully redundant configuration, with two CPU boards, based on the dual-core LEON3FT processor and two groups of 3 Compression and Scientific Processing (CSP) boards based on FPGAs. Each CSP will be provided with two FPGAs and dedicated input (raw scientific data) and output (data resulting from processing) buffers for each sensors. The input buffers will be based on 256Mbyte SDRAMs while the output ones on 4Mbyte SRAMs. The parallel processing capabilities of the CSP, together with high data rate point-to-point links between the CSP and the CPU, can ensure very good performances also in presence of a considerable number of sensors. Such architecture comprises also two PCDM modules and one Backplane and SpW Repeaters/Distributors (BSR).

The PPU SW is assumed to be structured in three layers: the Application Software layer (which will perform, amongst other functionalities, the scientific data processing), the Application Service Software and the Machine Services Software (which will include the Real Time Operating System kernel).

Heritage and consortium structure: PPU HW and SW will be provided by INAF-IAPS (PI: F. Marcucci). TSD/RTI, presently developing and manufacturing the Digital Processing Unit for the Solar Wind Analyser plasma suite on Solar Orbiter (see 53), has made available highly qualified expertise for the THOR PPU design and development. The TRL of the conceived PPU is 5 and PPU, which is based on existing space qualified components, can benefit considerably from the present implementation of the SWA DPU on Solar Orbiter.

Table 19: *PPU technical parameters. Mass, power and telemetry include 20% design margin.*

Mass	6 kg
Volume	20 x 25 x 16 cm
Accommodation	SC instrument platform
Power	20-30 W
Data products	3D and pitch-angle particle distributions, moments
TM rate	$\sim$ 3.5 Mbps
TRL	5

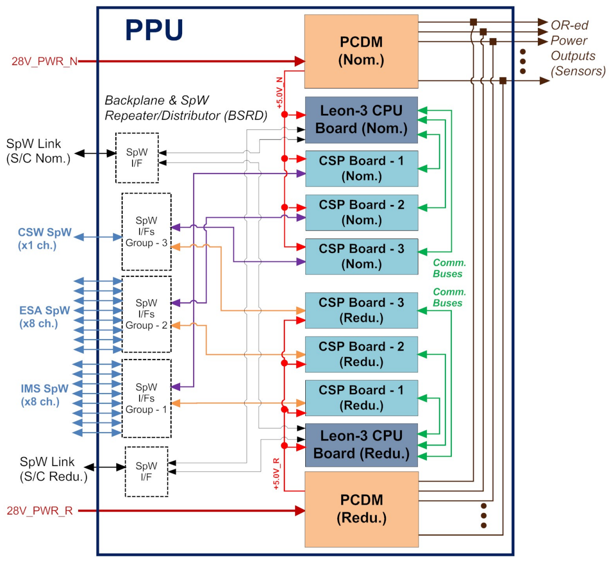

Figure 52: *PPU block diagram depicting the interfaces and redundancy concept (Courtesy of TSD/RTI).*

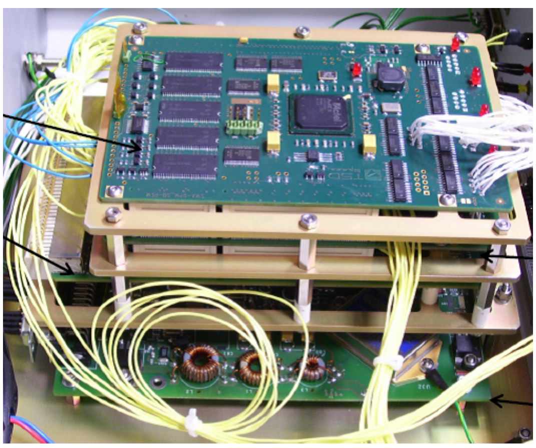

Figure 53: *Solar Orbiter SWA DPU engineering model (Courtesy of TSD/RTI).*

4.3 Payload operation

The payload operations concept is based on operating the payload as a whole, i.e. on simultaneous and coordinated operation of all instruments. The THOR payload is rather advanced, but it is simple to operate. The baseline is to operate the payload continuously, however some of the particle instruments may be switched off during parts of the orbit outside the key science regions in order to extend their life time. The payload will generate two science data streams transferred to the spacecraft mass memory:

- Survey data covering the full time at low time resolution,
- Burst data covering the full time in the *key science target regions* at high time resolution.

This payload operations strategy is similar to previous missions such as FAST, Cluster, THEMIS, STEREO.

The full Survey data is downloaded to ground. The telemetry rate is not sufficient to download the full volume of Burst data on each orbit, and therefore *selective data downlink* will be used for the Burst data, where the burst intervals for downlink will be selected based on the science priorities using the Survey data (see 6.4). In order to give sufficient time to select the scientifically interesting Burst intervals and prepare commands for downloading them, the on-board storage of ∼5 Tbits allows to store at least 275 hours of Burst data, which satisfies **RM-3**. Selective downlink is used on the present RBSP mission, as well is planned for the future missions like MMS, Solar Orbiter and JUICE.

Table 20 gives a representative instrument telemetry budget appropriate for the primary science objectives. Survey data provides continuous low TM stream of field and particle data which can be fast downloaded to ground and intended primarily to be used as a basis for selection of Burst intervals, however can be also used for other science and calibration purposes. Survey data contains MAG, SCM and EFI time series at 32 sps as well as spectra of E and B, as well as 3D distributions and moments for ions and electrons at up to 4 times per spin (7.5 sps). Survey data constitutes 10% to 20% of the total downlinked telemetry.

The total data rates mostly depend on the amount of Burst data downloaded. The particle instruments return their maximum telemetry rates in Burst (ion moments at 32 sps for FAR, 3D distributions at 100 sps for ESA, 3D distributions at up to 10 sps for IMS and 7 sps for CSW, 3D distributions once per spin for EPE), MAG at 128 sps, and EFI and SCM at 1024 sps with spectra and snapshots to cover higher frequencies and wave tracking to determine the density, resulting in telemetry rate of 4.5 Mbps. Closure on the main science question can be achieved with several hours of Burst data, also containing several minutes of *high-resolution waveform* (HRWF), downloaded per orbit. Such snapshots contain the SCM and EFI timeseries at 256 ksps giving telemetry rate of 29.5 Mbps. Acquisition of HRWF is enabled together with acquisition of Burst, but only transferred to the mass memory in short snapshots (up ∼10 sec long) at (a) commanded time instances (”honesty” data) and (b) when an on-board algorithm triggers on a particular criterium (triggered burst) such as a passing through an abrupt transition such as a current sheet. As the honesty bursts are acquired at predefined equidistant times, such data provides a statistically unbiased set of HRWF data, which complements the triggered bursts. The triggering is done by the FWP using the data from the fields sensors connected to FWP, and no communication with other instruments is required. Assuming downlink of 2 hours of Burst data per orbit gives a data volume of 40 Gbit per orbit. This representative figure is flexible: there is no requirement that this data volume be met on every orbit, and the duration of the Burst observations as well as the amount of HRWF data can be varied to fit the telemetry constraints.

Table 20: *THOR data rate budget.*

	4x16 RE	4x26 RE	14x60 RE
Survey			
Fraction of total TM	9%	20%	24%
Rate [kbps]	29.9	29.9	6.0
Data [Gbit/orbit]	3.9	7.4	6.5
Burst			
Data rate [kbps]	4651	4299	4299
Downloaded [min]	139	113	76
Downloaded [Gbit/orbit]	36.9	27.8	18.6
HRWF			
Data rate [kbps]	465	430	430
Downloaded [sec]	146	110	74
Downloaded [Gbit/orbit]	4.1	3.1	2.1
Total			
Downloaded [Gbit/orbit]	**44.9**	**38.3**	**27.2**

Data rate shows at which rate data are recorded in the spacecraft mass memory.

The baseline is to change the payload modes by use of a single command from the spacecraft which triggers execution of pre-defined sequences (macros) stored in the flash memory of the PPU and FWP. During the normal science operations such macros will need to be updated several times per year in order to optimize the instrument performance. Such optimization is needed due to evolution of plasma characteristics in the key science regions in the course of time as the orbit evolves and the plasma regions encountered for the dayside, down-dusk and tail orbits are sufficiently different. Also the telemetry rates in Survey/Burst will need to adjusted by altering temporal/angular/energy resolution following raise of the apogee and related decrease in the downlink capacity. Uploading new macros is considered a routine operation, which can be part of standard operations. The execution of a macro is tested by the PI teams on a ground reference units before uploading, and its telemetry output is verified. Tests on any integrated unit at ESA will not be needed for post-launch macro uploads. During prelaunch integrated tests, several macros will be used for on-ground calibration and verification purposes.

5 Mission profile

To meet the science objectives of Section 2, we propose the following mission profile.

5.1 Mission configuration and orbit

Mission life time The nominal mission is 3 years.

Spacecraft design THOR is designed as a sun-pointing spinning satellite with a suggested spin period of 30 sec. The design heritage is drawn from the OHB-Sweden Freja satellite. Spin is necessary to deploy and have long wire antennas to achieve accurate and sensitive electric field measurements (**RI-2**,**RS-3**), as well as for a complete angular coverage by energetic particle detectors (**RI-12**). The spin rate is not strongly constrained by the instrument performance requirements. However, lower spin rate decreases the time resolution for full energetic particle characterization, and higher spin rates impact on the fuel budget. The solar cells are mounted on dedicated panels at the edges on the top panel and can radiate from their back-sides. In addition, the lower platform has a smaller diameter than the top platform, further improving the radiative cooling to space. Side panels are not used, which reduces mass and allows more cooling possibilities to internally mounted equipment. The sides are however covered with single-layer foils with electrically conductive outer surfaces (ITO Kapton or black Kapton). Vertical shear walls connect the top and bottom platforms and provide mounting surfaces for the payload and system units. MLI is further used for thermal isolation, nominally on the space-facing side of each platform.

Orbit design To satisfy **RM-1** and **RM-2** THOR orbit has been designed to have 3 phases summarized in Table 22. Figure 54 shows the expected position of magnetopause and bow shock. In addition, the orbital coverage of THOR is colored gray. To spend long times at the bow shock (**RM-1**) while maximizing telemetry (**RM-2**) during the first year, Phase 1, orbit has low perigee 4 R_E and the apogee slightly outside the nominal bow shock location at 16 R_E. During the second year, Phase 2, to spend longer time periods in the undisturbed solar wind and foreshock (**RM-1**) orbit is designed with 26 R_E apogee. Finally in Phase 3 THOR is put in the orbit 14 x 60R_E where both long time periods in solar wind during apogee and long periods around bow shock at perigee are possible. The final orbit shall be stable yet have the possibility to use the moon to change the orbit during extended mission. This means that the orbit shall reach the moon orbit, yet it shall also assure that the influence of the moon is minimized. This is done by selecting an orbital period with a fraction of the moon orbital period. The true anomaly is then chosen such that the satellite is not close to the moon at apogee.

Launch and orbit injection THOR is launched with Soyuz launcher from Kourou. The spacecraft is injected into a geocentric 4R_E x 16R_E orbit with the orbital plane close to the ecliptic plane and apoapsis being in the dusk sector. The inclination of the orbit is set to 10°. Argument of perigee (ω) and right ascension of ascending node (Ω) are selected to a) ensure that the apogee cannot be in the ecliptic during equinoxes since this could generate very long eclipse durations (3.3h), and b) to ensure that sufficient clearance always exists to the geostationary ring. Allowable launch injection conditions are shown in Table 21 (generating maximum eclipse durations not exceeding 1.2h)

Table 21: *THOR launch injection conditions*

	March		June		September		December	
Ω	0°	180°	90°	270°	180°	0°	270°	90°
ω	270°	90°	270°	90°	270°	90°	270°	90°

For each time option, there are two different allowable launch injection conditions.

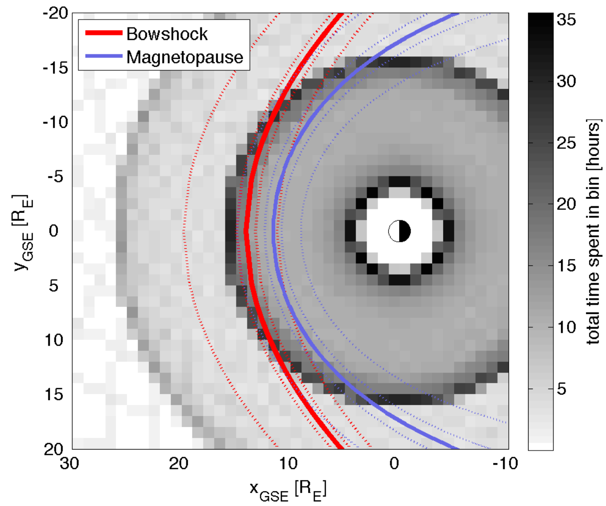

Figure 54: *The nominal location of bow shock and magnetopause for expected solar wind conditions 2025/26 based on the daily averaged OMNI data and common models. The solid lines show the mean position of bow shock and magnetopause, while the dashed lines show minimum, 25% percentile, 75% percentile and maximum position locations. Gray scale shows the orbital coverage of THOR.*

Table 22: *THOR mission phases*

Phase	Orbit	T [h]	ΔV to next orbit
1	4 x 16 R_E	44.53	204 m/s
2	4 x 26 R_E	81.81	214 m/s
3	4 x 61 R_E	330.37	260 m/s
	14 x 61 R_E		

Each of the mission phases lasts one full year. The total ΔV needed for orbital maneuvers is 678 m/s. Phase 3 involves Moon flybys to save ΔV.

Propulsion The propulsion subsystem is designed around a hydrazine propellant system, with an assumed specific impulse of 230s. The main thruster consists of one 20N thruster used for orbital transfers of THOR. A cluster of 1N thrusters are used for attitude control (precession control and spin rate establishment and maintanance). Transferring between the orbits during the mission requires ΔV=678 m/s, see Table 22. Applying 25% margin the total ΔV for the mission is calculated to be ~847m/s giving a propellant mass fraction of 0.46. This is achieved with 225 kg hydrazine. It is proposed to split the propellant load into eight smaller, and easier to accommodate, 45l propellant tanks. The minimum required volume of fuel in each of the tanks, including 10% margin, is 41.2l. The tanks are positioned radially in the satellite structure. They are connected in two branches which are nominally open and connected together to supply the propulsion system. It is however possible, should one branch fail, to isolate it and thus only use one branch, thus ensuring a partial degradation rather than a complete loss of mission.

Attitude requirements THOR shall be sun-pointing to within 10°, so as to maintain highly accurate electric field measurements (**RS-3**) and allow use of the Faraday cup for high time resolution monitoring of the solar wind (**RS-6**). For reconstructing plasma and field properties reliably, a reconstructed 3-axis attitude accuracy of 1° is needed.

Attitude control The main attitude control task during the operational phase of the mission is to maintain the spin-vector sun-pointing and to perform spin-rate maintenance. All AOCS maneuvers are performed using pairs of thrusters. Due to the low spin rate which renders fluid nutation dampers ineffective, it is anticipated to use the AOCS thrusters also for active nutation damping.

Attitude reconstruction The attitude determination system is based on X-beam sun-sensors (provides sun angle and spin-phase pulse) and APS star trackers. The reorientation of the spin vector towards the Sun can be performed autonomously on the basis of the sun sensor measurement or the inertial star tracker measurement.

5.2 Mass, power, link, radiaton budgets

Mass budget The THOR mass budget is given in Table 23. The total mass is compatible with Soyuz launch.

Table 23: *THOR mass budget*

	Item	CBE [kg]	CBE+DMM [kg]
	Platform	293	382
Payload	Payload	111,5	133,8
	Data handling	12	14,4
	Subtotal	**123,5**	**148,2**
	Spacecraft dry mass	**416,5**	**530,2**
	System margin		20%
	System total dry mass		**636,2**
Propellant	(maneouvers + AOCS)	**278,1**	305,9
	Propellant (residuals)		312,0
	Wet mass	**694,6**	**948,2**

Power budget The THOR power budget is given in Table 24. The payload does not need to be operated in eclipse, but the batteries need to support data dumps during short perigee eclipses and possibly essential heaters during long apogee eclipses, which may last for up to 72min. Solar array consists of triple junction cells (e.g. Azur 3G30) with an efficiency of 30%, yielding a BOL power of 563 W and EOL (3 years) power of 484 W. These assume an offset angle of 6% at a panel temperature of 60°C. There is ample space on the front side of the spacecraft to increase the surface area of the solar cells and thus their power output if necessary. To comply with EMC requirements (see 5.3), the power system will be a non-switching, linear shunted system, with dumping of excess power at several different locations on the spacecraft. Bus voltage will be maintained at 28±4V. The grounding concept will be a Distributed Single Point Ground system.

Table 24: *THOR power budget.*

	sunlight avg [W]	eclipse avg [W]
PCDU input power req	**483.07**	229.75
BME discharge losses		22.98
Battery power need		**252.73**

Margin of 20% is incuded. Assuming solar flux of 1323 W/m^{2}2, 60°C solarpanel, 6° offset angle, 7.85% loss factor and 30% BOL solar cells. Maximum eclipse time is 72 min.

Communication THOR will use X-band for uplink and downlink. Due to the required high telemetry rates and the orbital configurations (**RM-1**,**RM-2**), it is proposed to have a stepwise selectable downlink rate depending on the range to the ground station. In order to have a positive link margin of at least 2-3 dB, and to limit the number of link steps to 5, steps and distance ranges as in Table 25 are assumed. Data transmission from the satellite will be temporarily turned off when switching downlink reception rates in the ground station in order to avoid losing data. In order to increase the volume of retrieved science data, two ground stations spaced approximately 180° in longitude will be used for telemetry downlink. With the ESA Kourou station being assumed the primary station, the downlink will be divided between Kourou and the ESA ground station in Perth based on visibility during each orbit, nearly doubling the total downlink (Fig. 55). 15 m X-band ESTRACK ground stations are assumed, with G/T=37.5 dB/K. With 25W RF power and the use of a TWT configuration to reduce losses, an orbit average science data rate of ~345kbps for the first year and ~155kbps for the second year is achievable, see Table 25. For the 3rd year data rate is ~25kbps. The gain of the on-board antenna is assumed to be only -1 dBi allowing the use of standard LGA antennas as on Cluster.

Table 25: *THOR link budget*

Distance [RE]	Bit-rate [kbps]	
4-6	2400	
6-10	1000	
10-16	400	
16-34	100	
34-66	25	
4x16RE orbit	Contacts/2 weeks	Gbit/2 weeks
Kourou	13	210
Perth	13	207
3-25RE orbit	Contacts/2 weeks	Gbit/2 weeks
Kourou	14	109
Perth	13	77

Assuming 15m X-band ground antenna and G/T=37.5 dB/K.

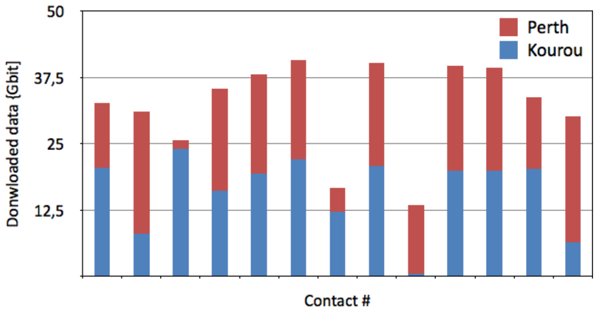

Figure 55: *THOR ground contact example for orbit 4×16 RE.*

Ground segment Spacecraft telemetry from the ground station will be provided as CCSDS Space Packets to the ESOC Missions Operations Centre (MOC) with all science TM and supporting platform telemetry forwarded to the Science Operations Centre (SOC). In the SOC, the science data is processed and the selection is made on which high resolution (Normal/Burst mode) data to download during the next ground contact. Selection is based on the Survey data, which is always downloaded in its entirety, with priority directly after housekeeping data (see section 6.4).

Operations concept The spacecraft operations (telecommands generation, telemetry reception, distribution and storage, orbit determination and maneuver planning/execution are all handled by ESOC, with off-line support provided by the System Prime contractor on a need-basis. The command lists to the scientific instruments will be generated by the SOC, for checking and uplinking by the ESOC MOC. Operational constraints for when propulsion manoeuvres are performed are allowed, and such manoeuvres should be avoided in the science data taking portion of the orbit. There is a 6 h latency allowed for distribution of payload data from the ground station to the SOC.

On-board data handling and TTC Payload instruments are primarily operated at altitudes above 8 RE. The payload instruments provide their data as complete CCSDS Space Packets to an on-board mass memory using a SpaceWire interface. Dumping of the mass memory is performed during each ground contact. At the start of the pass, the SOC commands which TM (max 1 Gbit) it wishes have downlinked during the pass. During the same pass, time-tagged telecommands are uploaded. These will consist mainly of payload ON/OFF commands and Tx ON/OFF times for the coming orbit(s). During the first part of the mission typical contact times will be in the order 10-15 h, allowing the downlinking of typically 10-20 GBits of data, see Figure 55. During the second part of the mission, the downlink rate is reduced as shown in Table 25.

Radiation The radiation environment has been predicted with SPENVIS for a 2-year mission. For a cover slide thickness of 50 μm, the received fluence at the solar cells is equivalent to $4*10^{14}$ 1 MeV electrons per cm^2, which results in a solar array power degradation of <2% using 3J GaAs cells (Azurspace 3G30C). The low degradation is due to the fact that the orbit is above the proton belts, and the prediction is for a 95% confidence level for solar flares. Increasing the confidence level to 99%, the received fluence for this coverslide thickness increases by a factor of 3 to $1.5\,10^{15}$ 1 MeV electrons per cm^2, which results in a solar array power degradation of $\leq$4%. The total 4π ionisation dose (Si) over the mission is in the order of 34 krad for 5mm of Aluminium shielding (137 krad for 3mm Al shielding). Box shielding will therefore be required and adequate mass margins have been allocated for this.

5.3 Electromagnetic Cleanliness

EMC issues are critical for THOR, requiring strict attention during all the phases of spacecraft and payload design and building, as in e.g. Cluster. To decrease the effect of spacecraft magnetic field on the measurements, the MAG and SCM sensors most sensitive to EM interference will be mounted at the ends of long booms away from interference source. The use of long booms has been used on many previous missions including Cluster, which provides very clean magnetic field measurements. Three top level EMC requirements are summarized in Table 26.

Magnetic cleanliness: To reliably observe weak magnetic fields as required by the science objectives, magnetic cleanliness at the level of Cluster is necessary: truly DC magnetic field, never changing and accurately characterized on ground shall stay below 5 nT at the magnetometer; long term variations (longer than 1 hour time scale) below 0.5 nT peak-to-peak; medium term variations (1 s – 1 h) shall not exceed 10 pT (averaged over 1 s) over a period of 1 h. The focus will be to ensure a very high stability of the spacecraft-generated magnetic disturbances (same approach as on Cluster). A dedicated magnetic cleanliness programme, verified at a magnetic calibration facility (IABG or similar), will be implemented in order to minimize current loops

Table 26: *THOR EMC requirements*

Low frequency magnetic cleanliness
REMC-1 The total magnetic field of the spacecraft should be minimized ($< 5\,\mathrm{nT}$) and properly characterized on ground. Slow variations (longer than 1 hour) in the spacecraft magnetic field should be limited to 0.5 nT peak-to-peak, and medium variations (1 second to 1 hour) to 10 pT peak-to-peak.
Electrostatic cleanliness
REMC-2 Differential surface charging of the spacecraft should be minimized to allow DC electric field measurements by EFI instrument. The voltage between any two points on spacecraft surface should be at most 1 V.
AC electromagnetic emissions
REMC-3 Electromagnetic emissions from both the spacecraft systems and payload in the frequency range of EFI, MAG and SCM instruments (DC to 250 kHz) must be minimized and controlled. Frequencies of emissions exceeding the noise floor of THOR instruments (c.f. Fig. 37 and Fig. 41) must be stable and synchronized to as few discrete frequencies as possible.

and the use of soft magnetic materials on board. This will include a deperm of the spacecraft complemented with rigorous AIT practices not exposing the spacecraft to magnetized tools etc. Existing platform equipment will be thoroughly reviewed with regard to magnetic cleanliness before being selected.

Electrostatic cleanliness: To observe low frequency electric fields at required accuracy and to maintain an even spacecraft potential, all outer surfaces of the spacecraft will be conductive and attached to spacecraft ground, with possible exception of small patches.

Electromagnetic noise: Very low AC fields (electric and magnetic) should be generated by the spacecraft during the main science data taking periods to ensure unperturbed high-frequency field measurements. (**RS-2**; c.f. Figures 37 and 41). To comply with this, the power system can be implemented as a non-switching, linear shunted system, with dumping of excess power at 12 different locations on the spacecraft. The grounding concept should be a Distributed Single Point Ground system. Harness routing must be optimized to minimize current loops and/or achieve self-compensation.

5.4 Additional subsystems

Active spacecraft potential control The Active Spacecraft Potential (ASP) controller reduces the positive spacecraft potential by emitting indium ions of 4 to about 10 keV energy. This allows for much more accurate plasma measurements at low energies comparable to the spacecraft potential and provides a better satellite potential environment improving the electric field measurements. On THOR ASP is located on the shadow side of the spacecraft and emits the ion beam away from the spacecraft in the anti-sunward direction. The main constituents of the ASP instrument is a pair of ion emitter units (4 emitters in total), each connected to a dedicated high voltage supply. The four emitters are present due to lifetime and redundancy reasons. The MMS emitters have demonstrated capability to achieve 9350 h operation time at a current level of 20 μA, which is the nominal operational value for MMS. THOR will be flown in a denser plasma environment than MMS and therefore would overall profit from a less charged spacecraft. Still to reduce the spacecraft potential to a lower level requires a stronger emitter current than in a sparse environment. To operate ASP with higher emitter currents, more ions can be emitted with only small impact on the overall mass. The ASP instrument has been flown on several missions like Equator-S, Cluster, and Double Star TC-1, and therefore has a high TRL. It will also be flown on the four spacecraft of the NASA MMS mission, planned to be launched in March 2015. All these ASP instruments were led by IWF/OEAW. For the most recent ASP (MMS), IWF was responsible for the instrument integration, the controller development, on-board and ground software, FOTEC Wiener Neustadt supplied the ion emitter modules, RUAG Space Austria supplied the electronics including the box and the ESA/ESTEC Science and Robotic Exploration Directorate provided modeling of ion beam and spacecraft potential.

5.5 Options, trade-offs and extension

Mission options *Telemetry* Significant increase in the downloaded data rate can be achieved using 35-m dishes (G/T=50.1 dB/K) instead of 15-m ones. For example, for the third year of mission this would allow to go from 25 kbps to 500 kbps, thus allowing almost 20 times higher telemetry rates.

Mission descoping options Phase 3 can be simplified to orbit 4 x 40-50R$_E$, saving $\Delta V \sim 300\,\mathrm{m/s}$. Such an orbit would still return excellent data from undisturbed solar wind but it would not allow a good coverage of bow shock and magnetosheath during the 3rd year. However, bow shock and magnetosheath are well covered during Phase 1.

Extended mission scenarios As suggested, THOR is a highly focused scientific mission with payload and systems slimmed to target the main science goals. Several variations of the above scenario not jeopardizing these goals are easy to see:
<u>Orbit variation</u> Depending on available launch opportunities, the inclination and perigee altitude may be raised to nearly arbitrary values. This could impact downlink strategy and radiation doses, but otherwise does not change the ability to meet THOR science goals.
<u>Solar wind monitor</u> This would require more fuel to reach suitable orbits (ideal is L1, but e.g. elliptic lunar orbits can also work), increase of designed lifetime to several years, and a significant increase

of operational time.

Coordination with other missions This scenario would require active orbital control.

6 Management scheme

6.1 Procurement scheme

ESA ESA would be responsible for spacecraft manufacturing, launch and operations, as well as, the data archiving and distribution.

National agencies All scientific instruments of THOR would be provided by the national agencies. Table 27 shows all the national agencies with a planned hardware contribution to the THOR payload and their responsibility within the instrument consortia. More detailed description of each of the instrument consortia can be found in the respective description of the instrument. In addition to hardware provision, the national agencies would have to support instrument operations, data calibration and data processing at least throughout the nominal phase of the mission.

6.2 Programme participation

The possible modes of participation to the THOR programme are:

Principal Investigator (**PI**), heading an instrument consortium providing an instrument.

Co-Principal Investigator (**Co-PI**) is appointed if he/she is responsible for a major contribution to the development and building of an instrument and he/she is from a country/institution different from the one of the PI.

Lead co-Investigator (**Lead Co-I**), is appointed if he/she is responsible for a significant development and building of an instrument and he/she is from a country/institution different from the one of the PI.

Co-Investigator (**Co-I**), a member of a consortium providing an instrument and having a well-defined role in the instrument team, serving under the direction of the PI, and being critical for the successful completion of instrument goals by contributing unique expertise and/or capabilities.

Interdisciplinary Scientist (**IDS**), an expert in specific overarching science themes connected to the mission objectives who takes advantage of synergistic use of the THOR data. To ensure a top-level oversight of mission science, four Interdisciplinary Scientists (IDS) will be selected through an open AO process after the start of the implementation phase. In general, IDSs should not reflect instrument specific domains, but rather cover specific science themes (e.g, shocks, turbulence, numerical simulations, etc.).

Guest Investigator (**GI**), scientist responsible for dedicated data collection and analysis campaigns . GIs can support their campaigns by performing laboratory studies, theoretical or numerical investigations. Their proposals shall be submitted to ESA following an open AO process during the operational phase of the mission. Their tasks shall be agreed directly with the PIs, with concurrence of the ESA Project Scientist.

6.3 Science management

Science management for THOR is typical for ESA science projects, as for example JUICE.

Project Scientist ESA nominates the THOR Project Scientist (PS). PS is the Agency's interface with the Principal Investigators . PS will chair Science Working Team (SWT) and coordinate its activities.

Science Working Team SWT will consist of PS, PIs and IDSs. Co-PIs, Co-Is, GIs and other interested scientists will be invited to participate in SWT meetings, as appropriate. The SWT will monitor and advise ESA on all aspects of the mission that will affect its scientific performance. SWT is responsible for planning of science operations and development of the Master Science Plan (MSP).

6.4 Operations and data

Mission Operations Concept ESA will be responsible for the launch and operations/checkout of the spacecraft. ESA will establish a THOR Mission Operations Centre (MOC) located at ESOC and a Science Operations Centre (SOC) located at ESAC. Interaction between SOC, MOC, SWT and the PI teams is illustrated in Figure 56.

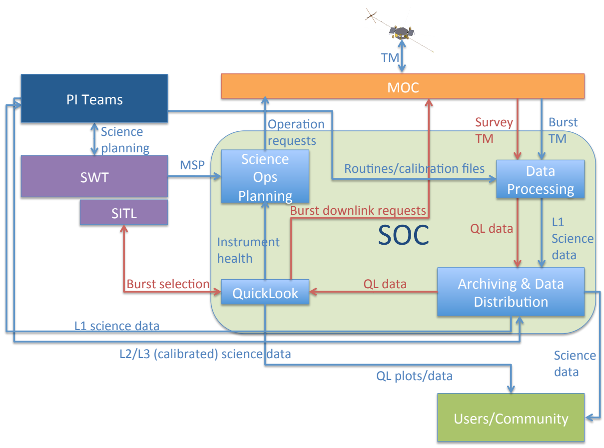

Figure 56: *THOR SGS structure and interaction with MOC and SWT/PI-teams, as well as with science community.*

Mission Operations The THOR MOC will be responsible for the operations of the spacecraft.

Science Operations The Science Ground Segment (SGS) consists of the Science Operations Centre (SOC) and contributions from the PI teams, including the scientist in the loop (described below). The ESA Ground Stations network, under the responsibility of ESOC, will support the telemetry and telecommand communications.

Scientific mission planning. The baseline for the THOR science operations is to collect and save on-board high resolution Burst and Fast data for parts of the orbit corresponding to key science target regions defined by the mission science require-

Table 27: *National labs with the planned hardware contribution to the THOR payload.*

Instrument	PI	Co-PI	Lead CoI
MAG	IWF(Austria)	ICL(UK)	
SCM	LPP(France)	LPC2E(France)	
EFI	IRF(Sweden)	SSL(USA)	SRC-PAS(Poland), KTH(Sweden)
FWP	IAP(Czech Rep.)	SRC-PAS(Poland)	Univ. Sheffield(UK), LESIA(France)
ESA	MSSL(UK)	NASA/GSFC(USA)	
CSW	IRAP(France)	BIRA-ISAB(Belgium)	
IMS	LPP(France)	UNH(USA)	ISAS/JAXA(Japan), MPS(Germany)
PPU	INAF-IAPS(Italy)		
FAR	MFF(Czech Rep.)		
EPE	IEAP(Germany)	Univ. Turku(Finland)	

ments, see figure 57. The MSP (produced by the SWT) defines time intervals for which Burst collection is enabled in accordance to predicted location of the key science target regions, such as the bowshock, magnetosheath and solar wind. A relatively small fraction of the Burst data can be transmitted to ground due to telemetry limitations (see Section 4.3). Selection of scientifically interesting burst intervals for downlink is done on ground based on the Survey stream which is being saved on-board during the entire period when the spacecraft payload is operating.

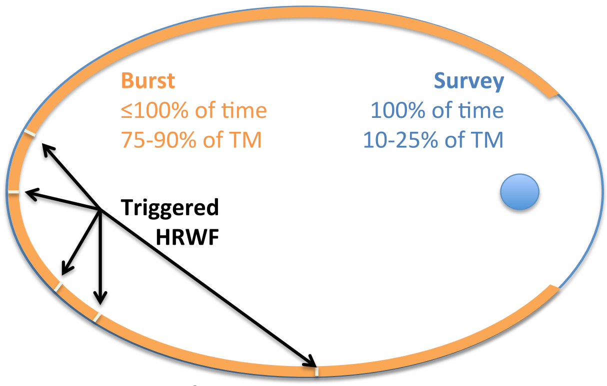

Figure 57: *THOR telemetry acquisition along the orbit. Survey data is sampled all the time, while Burst data is acquired only in the key science region. Burst data contains snapshots high-resolution waveforms (HRWF) of electric and magnetic fields; snapshot acquisition is both time and data triggered.*

Selective data downlink. During the ground contact, all of the Survey data and, in addition, Burst data from the previously selected intervals are transmitted (see Figure 58). The Survey data will be pipeline processed by SOC to produce Survey QuickLook products using software developed in cooperation with the PI teams and the best available calibrations at the moment the data are received. The Survey QuickLook products will provide the SOC with an overview of the data captured during the preceding period and will be used to assess instrument health and to select the intervals of Burst data to be downloaded.

Burst selection. Identification of the interesting time intervals from which to download Burst

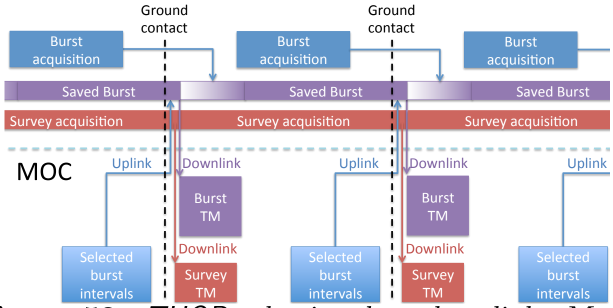

Figure 58: *THOR selective data downlink. More data than can be downlinked are acquired. During the ground contact all Survey data since the previous ground contact (a small volume) is downlinked, followed by selected Burst data.*

data is based on inspection of the Survey data as well as the ancillary data transmitted with the Survey stream. Such ancillary data will contain times of HRWF snapshots as well as other very low TM products obtained by on-board reduction of Burst data and characterizing Burst data available on-board, for example counter of electrostatic solitary waves, pseudo-moments of particle distributions, maximum electron flux in a particular channel over 1 minute period. The Burst data is then split into intervals and a figure of merit (FM) is assigned to each os the intervals, so that the intervals with higher FM will be have higher priority in the downlink queue. Selection of intervals can be done by an automatic algorithm at SOC, or by the Scientist In The Loop (SITL) assigned by the SWT. Initially the SITL responsibility will be circulated between the members of the PI teams, but the participation of a wider science community via GI programme is possible later in the mission. The SITL will be able to carry out his/her responsibilities remotely over the internet. A similar strategy involving a SITL is employed by the NASA MMS and RBSP missions.

The SITL selection will be performed using a dedicated SITL software tool which will access the Survey QuickLook data at the SOC, as well as information on the amount of telemetry available for the selection. The SITL software and will generate and provide to the SOC via a simple software interface the selected Burst time intervals and corresponding FMs, which will be converted to actual telecommands by software at the SOC. In case SITL selection is not available at the moment the SOC needs to generate the telecommands for Burst downlink, the intervals and FMs produced by the default automatic algorithm will be used, so that the *downlink commands will be always generated and no ground contact will be missed* (Figure 59). The amount of on-board storage allows to keep the acquired Burst for a period of 8–10 days, which defines the time frame for the SOC/SITL to make decisions about Burst selection. The ground contacts are planned at several times per orbit which means several ground contacts during the 10-day window, securing downlink of selected intervals. The timeline of SOC operations is summarized in Table 28 and Figure 56.

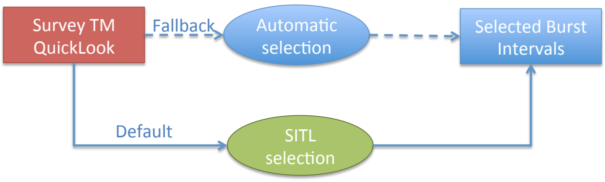

Figure 59: *THOR Burst selection is done by SITL, but an automatic algorithm will be used as a fallback option if SITL is not available.*

Table 28: *THOR science operations timeline (Time After Ground Receipt - TAGR).*

TAGR	Entity	Action
0h	SOC	recieve data
6h	SOC	Error check data
8h	SOC	Generate QL data
12h	SOC	Release QL data
12h	SITL	Start select BM intervals

Quick Look data. Apart from the Survey QuickLook Data, also Burst QuickLook products will also be produced at the SOC and will be put online within 24 hours of ground receipt. The Cluster QuickLook plot system serves as heritage for the THOR QuickLook system.

Data Rights and Policy THOR will employ the Open Data policy starting from 6 month into the nominal operations (after the end of commissioning). This 6 month delay is needed for the PI teams to establish the data processing and calibration pipelines. PI/Co-I must approve publication of data during the nominal mission. After the end of the nominal mission PI/Co-I approval is no longer needed, but consulting the PI team for data quality issues is still recommended.

Data distribution and archiving are an essential part of the mission. The existing system such as CAA/CSA (interface and design) can be used which reduces the costs. Implementation of the system need to start 2 years before launch, and acrhiving need continue 2 years after the end of the operations. Within one month of receipt, initial versions of the science data will be generated by the PI teams based on the latest calibrations and will be put online for use by the science community. All THOR data products will be open access from the time of delivery to the SOC by the PI teams. Refinement of the calibrations, using inflight experience and cross-calibration activities, is the responsibility of the PI teams. In case the calibration refinements affect old data products, these products will be reprocessed and redelivered to SOC with the file versions incremented. The science products provided by SOC will include high-resolution data in the spinning spacecraft frame, in the despun spacecraft frame and in Geocentric Solar Ecliptic (GSE) coordinates. After the end of the active phase of the mission we would expect the long-term archive to be held by ESA/ESAC, building on the Cluster Active Archive (CAA) and Cluster Science Archive (CSA) heritage. Figure 56 summarizes THOR data flow.

Science data analysis There is long list of data analysis methods and tools that are available for studies of THOR data. In Table 29 we show some of the methods with particular focus on analyzing waves and coherent structures, such as current sheets. All those are single spacecraft methods, however most of them have been validated using multi-spacecraft Cluster data.

Numerical simulation support The THOR team includes many scientists developing and running different plasma simulation codes addressing the physics of turbulence, shocks and reconnection. Table 30 is a list of codes accessible to the THOR team which can be used to support science data analysis and mission planning.

Table 30: *Numerical simulation codes available to support THOR science data analysis. For additional material including simulation movies see* `http://thor.irfu.se/home/numerical-simulations`.

Code	Type
HVM3D3V	Hybrid Vlasov-Maxwell 3D-3V
iPIC3D	Implicit moment PIC 3D
AstroGK	Eulerian continuum
GENE	Eulerian continuum
P3D	explicit PIC
TFPC	Two-fluid PISA code
Vlasiator	Hybrid-Vlasov
vpic-H3D	Relativistic 3D PIC
dHybrid	Hybrid - PIC
Vlem2D3V	Semi-Lagrangian Vlasov-Maxwell

Broad community involvement Broad community involvement is possible via the Open Data policy. Fast access to mission data via QuickLook plots- 24 hours after receipt, and fully calibrated data 30 days after receipt. Guest Investigator program which will be established after the launch. SWT together with GIs will generate MSP based on GIs science cases, and GIs could also serve as

Table 29: *Common methods for analysing plasma structures, boundaries, waves and turbulent fluctuations.*

Residue methods		Orient	Veloc	Accel	Required data
MVAB	Min variance of **B**	X			**B**
MVAE	Max variance of **E**	X			full 3D **E** field
HT	deHoffmann-Teller analysis		X	X	**E**, alternatively **V** and **B**
MFR	Min Faraday Residue	X	X		**E**, alternatively **V** and **B**
MMR	Min massflow residue	X	X		**V**, **B** and n (density)
MLMR	Min linear momentum res.	X	X		**V**, **B**, n, P[1] (pressure)
MTER	Min total energy residue	X	X		**V**, **B**, n, P, H (heat flux)
MER	Min entropy residue	X	X		**V**, **B**, n, P
COM[2]	Combination of above	X	X		
Reconstruction methods		**Product**			**Required data**
GS	Grad Shafranov	2.5D reconstruction of $\mathbf{B}, \mathbf{V}, P$			$\mathbf{B}, \mathbf{V}, P$
SRM[167]	Streamline Reconstr. Meth.	2D map of **V** field			$\mathbf{B}, \mathbf{V}, P, \rho$
GMHD[168]	General MHD reconstruction	2D field and plasma maps			$\mathbf{B}, \mathbf{V}, P, \rho$
HMHD[169]	Hall MHD reconstruction	as above + Hall effects significant			$\mathbf{B}, \mathbf{V}, p, \rho$, 2 comp of **E**
Wave/structure analysis methods		**Product**			**Required data**
	Multi-probe interferometry	phase velocity			**E**, n
	EMHD structure reconstr.[170]	phase velocity			**E**, **B**, n
Taylor		spatial scales			**v** and one of $\mathbf{E}/\mathbf{B}/\delta n$
Means		Polarization properties			**B**
SVD	Singular Value Decomposition	Polarization properties			$\mathbf{E}, \mathbf{B}$
Statistical analysis methods		**Product**			**Required data**
PDF	Probability Distr. Funct.	Intermittency description			time series
PVI	Partial Variance of Increments	Intermittency description			time series
SF	Structure Function	Self-similarity, fractal behaviour			time series
LIM[171]	Local Intermittency Measure	Wavelet intermittency			time series
PFMA	Partition f-n multifract. analys.	Gen. multifractal dimension			time series

For an overview of methods, see 172–174 and references therein. Methods not described in those papers are referenced individually.

[1] *Plasma pressure or temperature as a scalar or tensor quantity.*

[2] *Combining variance matrices from several methods used to utilize all available information.*

SITL during the implementation of GIs obs. THOR science meetings are open to broad science community.

Communication and Public Outreach

THOR is a mission to understand fundamental plasma processes of turbulent plasma environment in near-Earth space. The understanding of those processes will lead to important progress in understanding other plasma environments in the solar system, universe and laboratory. The term "turbulence" is often used also in everyday language, which gives many opportunities to connect to everyday life outside of plasma physics. This gives a wide spectra of possibilities for communication, outreach and education opportunities.

Based on experience from recent missions there will be many exciting new research results that can be demonstrated through press releases, outreach activities and educational material. Thus solar storms, geomagnetic activity, and their consequences (spectacular aurora, telecommunications and technical systems outages, and bio-hazards) provide visual and tangible vehicles to convey the mission message. Solar wind turbulence, turbulence in stellar winds, interstellar medium, Earth bow shock, shocks at coronal mass ejections, supernova shocks, tokamaks, are some of the examples that will be used to show the application of the science results. Space science is fun, of fundamental importance for society and of everyday importance for the average citizen. THOR will be a clear demonstration of the important European role in space science.

THOR project has a common integrated web presence at thor.irfu.se where in addition to information about the mission, spacecraft, instruments and data access, different outreach-specific material will be available. The preparation of that material will be based on the successful experience in using such material from Cluster, THEMIS, MMS and other missions together with ground-based observatories and facilities where appropriate.

Before launch school classes (age 6 to 16) will be given the opportunity to provide examples (photos or sound recordings) of what they consider "turbulence" and selected items will be stored on some suitable medium on-board THOR before launch. In a similar way photos of the classes can be "sent into space". At a suitable time before launch, school classes and their teachers are invited together with the press to see the (nearly finished) flight instruments. The same people are then invited to watch the live (ESA) TV coverage of the launch together with some of the involved scientists and engineers. After launch, our web page gives continues information on the position of THOR, which ground station is being used and other technical information, together with preliminary near-real-time overview scientific data open to the general public.

A Annexes

A.1 References

[1] H. Alfvén. The plasma universe. Physics Today, 39:22–27, September 1986.

[2] D. Biskamp. Magnetohydrodynamics Turbulence. Cambridge, UK: Cambridge University Press, —c2003, 2003.

[3] C. A. Hajivassiliou. Distribution of plasma turbulence in our Galaxy derived from radio scintillation maps. Nature, 355:232–234, January 1992.

[4] A. A. Schekochihin and S. C. Cowley. Turbulence, magnetic fields, and plasma physics in clusters of galaxies. Phys.Plasmas, 13(5):056501, May 2006.

[5] A. Brandenburg and Å. Nordlund. Astrophysical turbulence modeling. Rep.Pr.Ph., 74(4):046901, April 2011.

[6] A. Brandenburg, K. Subramanian, A. Balogh, and M. L. Goldstein. Scale Dependence of Magnetic Helicity in the Solar Wind. ApJ, 734:9, June 2011.

[7] R. Bruno and V. Carbone. The Solar Wind as a Turbulence Laboratory. Living Reviews in Solar Physics, 10:2, May 2013.

[8] S. Galtier. Wave turbulence in magnetohydrodynamics. ArXiv e-prints, January 2012.

[9] O. Alexandrova, C. H. K. Chen, L. Sorriso-Valvo, T. S. Horbury, and S. D. Bale. Solar Wind Turbulence and the Role of Ion Instabilities. Space Sci. Rev., 178:101–139, October 2013.

[10] B. G. Elmegreen and J. Scalo. Interstellar Turbulence I: Observations and Processes. ARA&A, 42:211–273, September 2004.

[11] D. Arzoumanian, P. André, P. Didelon, V. Könyves, N. Schneider, A. Men'shchikov, T. Sousbie, A. Zavagno, S. Bontemps, J. di Francesco, M. Griffin, M. Hennemann, T. Hill, J. Kirk, P. Martin, V. Minier, S. Molinari, F. Motte, N. Peretto, S. Pezzuto, L. Spinoglio, D. Ward-Thompson, G. White, and C. D. Wilson. Characterizing interstellar filaments with Herschel in IC 5146. A&A, 529:L6, May 2011.

[12] J. Saur. Turbulent Heating of Jupiter's Middle Magnetosphere. ApJ, 602:L137–L140, February 2004.

[13] V. M. Uritsky, J. A. Slavin, G. V. Khazanov, E. F. Donovan, S. A. Boardsen, B. J. Anderson, and H. Korth. Kinetic-scale magnetic turbulence and finite Larmor radius effects at Mercury. Journal of Geophysical Research (Space Physics), 116:9236, September 2011.

[14] M. von Papen, J. Saur, and O. Alexandrova. Turbulent magnetic field fluctuations in Saturn's magnetosphere. J. Geophys. Res., 119:2797–2818, April 2014.

[15] E. M. Reynoso, J. P. Hughes, and D. A. Moffett. On the Radio Polarization Signature of Efficient and Inefficient Particle Acceleration in Supernova Remnant SN 1006. AJ, 145:104, April 2013.

[16] T. A. Carter, H. Ji, F. Trintchouk, M. Yamada, and R. M. Kulsrud. Measurement of Lower-Hybrid Drift Turbulence in a Reconnecting Current Sheet. Phys. Rev. Lett., 88(1):015001, January 2002.

[17] P. Ricci and B. N. Rogers. Turbulence Phase Space in Simple Magnetized Toroidal Plasmas. Phys. Rev. Lett., 104(14):145001, April 2010.

[18] L. Sorriso-Valvo, R. Marino, V. Carbone, A. Noullez, F. Lepreti, P. Veltri, R. Bruno, B. Bavassano, and E. Pietropaolo. Observation of inertial energy cascade in interplanetary space plasma. Phys. Rev. Lett., 99:115001, Sep 2007.

[19] R. J. Leamon, C. W. Smith, N. F. Ness, W. H. Matthaeus, and H. K. Wong. Observational constraints on the dynamics of the interplanetary magnetic field dissipation range. J. Geophys. Res., 103:4775–+, March 1998.

[20] D. Sundkvist, A. Retinò, A. Vaivads, and S. D. Bale. Dissipation in Turbulent Plasma due to Reconnection in Thin Current Sheets. Phys. Rev. Lett., 99(2):025004, July 2007.

[21] F. Sahraoui, M. L. Goldstein, P. Robert, and Y. V. Khotyaintsev. Evidence of a cascade and dissipation of solar-wind turbulence at the electron gyroscale. Phys. Rev. Lett., 102(23):231102–+, June 2009.

[22] O. Alexandrova, J. Saur, C. Lacombe, A. Mangeney, J. Mitchell, S. J. Schwartz, and P. Robert. Universality of solar-wind turbulent spectrum from mhd to electron scales. Phys. Rev. Lett., 103:165003–+, October 2009.

[23] S. J. Schwartz, T. Horbury, C. Owen, W. Baumjohann, R. Nakamura, P. Canu, A. Roux, F. Sahraoui, P. Louarn, J.-A. Sauvaud, J.-L. Pinçon, A. Vaivads, M. F. Marcucci, A. Anastasiadis, M. Fujimoto, P. Escoubet, M. Taylor, S. Eckersley, E. Allouis, and M.-C. Perkinson. Cross-scale: multi-scale coupling in space plasmas. ExpAstr, 23:1001–1015, March 2009.

[24] A. Vaivads, G. Andersson, S. D. Bale, C. M. Cully, J. de Keyser, M. Fujimoto, S. Grahn, S. Haaland, H. Ji, Y. V. Khotyaintsev, A. Lazarian, B. Lavraud, I. R. Mann, R. Nakamura, T. K. M. Nakamura, Y. Narita, A. Retinò, F. Sahraoui, A. Schekochihin, S. J. Schwartz, I. Shinohara, and L. Sorriso-Valvo. EIDOSCOPE: particle acceleration at plasma boundaries. ExpAstr, pages 35–+, July 2011.

[25] B. D. G. Chandran, B. Li, B. N. Rogers, E. Quataert, and K. Germaschewski. Perpendicular Ion Heating by Low-frequency Alfvén-wave Turbulence in the Solar Wind. ApJ, 720:503–515, September 2010.

[26] S. Servidio, W. H. Matthaeus, M. A. Shay, P. A. Cassak, and P. Dmitruk. Magnetic reconnection in two-dimensional magnetohydrodynamic turbulence. Phys. Rev. Lett., 102(11):115003–+, March 2009.

[27] E. Camporeale and D. Burgess. The Dissipation of Solar Wind Turbulent Fluctuations at Electron Scales. ApJ, 730:114, April 2011.

[28] S. Servidio, F. Valentini, F. Califano, and P. Veltri. Local Kinetic Effects in Two-Dimensional Plasma Turbulence. Phys. Rev. Lett., 108(4):045001, January 2012.

[29] H. Karimabadi, V. Roytershteyn, M. Wan, W. H. Matthaeus, W. Daughton, P. Wu, M. Shay, B. Loring, J. Borovsky, E. Leonardis, S. C. Chapman, and T. K. M. Nakamura. Coherent structures, intermittent turbulence, and dissipation in high-temperature plasmas. Phys.Plasmas, 20(1):012303, January 2013.

[30] J. M. TenBarge and G. G. Howes. Current Sheets and Collisionless Damping in Kinetic Plasma Turbulence. ApJ, 771:L27, July 2013.

[31] A. Retinò, D. Sundkvist, A. Vaivads, F. Mozer, M. André, and C. J. Owen. In situ evidence of magnetic reconnection in turbulent plasma. NatPhys, 3:236–238, 2007.

[32] S. Perri, M. L. Goldstein, J. C. Dorelli, and F. Sahraoui. Detection of Small-Scale Structures in the Dissipation Regime of Solar-Wind Turbulence. Phys. Rev. Lett., 109(19):191101, November 2012.

[33] A. A. Schekochihin, S. C. Cowley, W. Dorland, G. W. Hammett, G. G. Howes, E. Quataert, and T. Tatsuno. Astrophysical gyrokinetics: Kinetic and fluid turbulent cascades in magnetized weakly collisional plasmas. ApJS, 182:310–377, May 2009.

[34] J. Cho and A. Lazarian. Simulations of electron magnetohydrodynamic turbulence. ApJ, 701:236–252, August 2009.

[35] G. G. Howes, J. M. Tenbarge, W. Dorland, E. Quataert, A. A. Schekochihin, R. Numata, and T. Tatsuno. Gyrokinetic Simulations of Solar Wind Turbulence from Ion to Electron Scales. Phys. Rev. Lett., 107(3):035004, July 2011.

[36] Y. Voitenko and M. Goossens. Nonlinear excitation of small-scale Alfvén waves by fast waves and plasma heating in the solar atmosphere. Sol. Phys., 209:37–60, September 2002.

[37] J. Soucek and C. P. Escoubet. Cluster observations of trapped ions interacting with magnetosheath mirror modes. Ann.Geophys., 29:1049–1060, June 2011.

[38] A. Kis, O. Agapitov, V. Krasnoselskikh, Y. V. Khotyaintsev, I. Dandouras, I. Lemperger, and V. Wesztergom. Gyrosurfing Acceleration of Ions in Front of Earth's Quasi-parallel Bow Shock. ApJ, 771:4, July 2013.

[39] F. Valentini, V. Carbone, P. Veltri, and A. Mangeney. Self-consistent Lagrangian study of nonlinear Landau damping. Phys. Rev. E, 71(1):017402, January 2005.

[40] D. M. Malaspina, D. L. Newman, L. B. Wilson, III, K. Goetz, P. J. Kellogg, and K. Kersten. Electrostatic Solitary Waves in the Solar Wind: Evidence for Instability at Solar Wind Current Sheets. J. Geophys. Res., 118:591–599, February 2013.

[41] C. S. Salem, G. G. Howes, D. Sundkvist, S. D. Bale, C. C. Chaston, C. H. K. Chen, and F. S. Mozer. Identification of Kinetic Alfvén Wave Turbulence in the Solar Wind. ApJ, 745:L9, January 2012.

[42] C. Lacombe, O. Alexandrova, L. Matteini, O. Santolík, N. Cornilleau-Wehrlin, A. Mangeney, Y. de Conchy, and M. Maksimovic. Whistler Mode Waves and the Electron Heat Flux in the Solar Wind: Cluster Observations. ApJ, 796:5, November 2014.

[43] S. D. Bale, P. J. Kellogg, F. S. Mozer, T. S. Horbury, and H. Reme. Measurement of the electric fluctuation spectrum of magnetohydrodynamic turbulence. Phys. Rev. Lett., 94(21):215002–+, June 2005.

[44] C. H. K. Chen, S. Boldyrev, Q. Xia, and J. C. Perez. Nature of Subproton Scale Turbulence in the Solar Wind. Phys. Rev. Lett., 110(22):225002, May 2013.

[45] S. Boldyrev, K. Horaites, Q. Xia, and J. C. Perez. Toward a Theory of Astrophysical Plasma Turbulence at Subproton Scales. ApJ, 777:41, November 2013.

[46] K. H. Kiyani, S. C. Chapman, F. Sahraoui, B. Hnat, O. Fauvarque, and Y. V. Khotyaintsev. Enhanced Magnetic Compressibility and Isotropic Scale Invariance at Sub-ion Larmor Scales in Solar Wind Turbulence. ApJ, 763:10, January 2013.

[47] C. H. K. Chen, S. D. Bale, C. Salem, and F. S. Mozer. Frame Dependence of the Electric Field Spectrum of Solar Wind Turbulence. ApJ, 737:L41, August 2011.

[48] R. Marino, L. Sorriso-Valvo, V. Carbone, A. Noullez, R. Bruno, and B. Bavassano. Heating the Solar Wind by a Magnetohydrodynamic Turbulent Energy Cascade. ApJ, 677:L71–L74, April 2008.

[49] V. Carbone, R. Marino, L. Sorriso-Valvo, A. Noullez, and R. Bruno. Scaling Laws of Turbulence and Heating of Fast Solar Wind: The Role of Density Fluctuations. Phys. Rev. Lett., 103(6):061102, August 2009.

[50] J. E. Stawarz, B. J. Vasquez, C. W. Smith, M. A. Forman, and J. Klewicki. Third Moments and the Role of Anisotropy from Velocity Shear in the Solar Wind. ApJ, 736:44, July 2011.

[51] C. H. K. Chen, L. Sorriso-Valvo, J. Šafránková, and Z. Němeček. Intermittency of Solar Wind Density Fluctuations From Ion to Electron Scales. ApJ, 789:L8, July 2014.

[52] O. Alexandrova, C. Lacombe, A. Mangeney, R. Grappin, and M. Maksimovic. Solar Wind Turbulent Spectrum at Plasma Kinetic Scales. ApJ, 760:121, December 2012.

[53] F. Sahraoui, M. L. Goldstein, G. Belmont, P. Canu, and L. Rezeau. Three dimensional anisotropic k spectra of turbulence at subproton scales in the solar wind. Phys. Rev. Lett., 105(13):131101–+, September 2010.

[54] R. Meyrand and S. Galtier. A universal law for solar-wind turbulence at electron scales. ApJ, 721:1421–1424, October 2010.

[55] G. G. Howes, W. Dorland, S. C. Cowley, G. W. Hammett, E. Quataert, A. A. Schekochihin, and T. Tatsuno. Kinetic simulations of magnetized turbulence in astrophysical plasmas. Phys. Rev. Lett., 100(6):065004, Feb 2008.

[56] J. M. TenBarge and G. G. Howes. Evidence of critical balance in kinetic Alfvén wave turbulence simulations a). Physics of Plasmas, 19(5):055901, May 2012.

[57] Y. Narita, K.-H. Glassmeier, F. Sahraoui, and M. L. Goldstein. Wave-vector dependence of magnetic-turbulence spectra in the solar wind. Phys. Rev. Lett., 104(17):171101–+, April 2010.

[58] C. H. K. Chen, T. S. Horbury, A. A. Schekochihin, R. T. Wicks, O. Alexandrova, and J. Mitchell. Anisotropy of solar wind turbulence between ion and electron scales. Phys. Rev. Lett., 104(25):255002–+, June 2010.

[59] L. Sorriso-Valvo, E. Yordanova, and V. Carbone. On the scaling properties of anisotropy of interplanetary magnetic turbulent fluctuations. Eur.Phys.Lett., 90:59001–+, June 2010.

[60] A. Mangeney, C. Lacombe, M. Maksimovic, A. A. Samsonov, N. Cornilleau-Wehrlin, C. C. Harvey, J.-M. Bosqued, and P. Trávníček. Cluster observations in the magnetosheath - Part 1: Anisotropies of the wave vector distribution of the turbulence at electron scales. Ann.Geophys., 24:3507–3521, December 2006.

[61] O. Alexandrova, V. Carbone, P. Veltri, and L. Sorriso-Valvo. Small-Scale Energy Cascade of the Solar Wind Turbulence. ApJ, 674:1153–1157, February 2008.

[62] F. Sahraoui, S. Y. Huang, G. Belmont, M. L. Goldstein, A. Rétino, P. Robert, and J. De Patoul. Scaling of the Electron Dissipation Range of Solar Wind Turbulence. ApJ, 777:15, November 2013.

[63] J. He, E. Marsch, C. Tu, S. Yao, and H. Tian. Possible Evidence of Alfvén-cyclotron Waves in the Angle Distribution of Magnetic Helicity of Solar Wind Turbulence. ApJ, 731:85, April 2011.

[64] J. J. Podesta and S. P. Gary. Magnetic Helicity Spectrum of Solar Wind Fluctuations as a Function of the Angle with Respect to the Local Mean Magnetic Field. ApJ, 734:15, June 2011.

[65] K. G. Klein, G. G. Howes, J. M. TenBarge, and J. J. Podesta. Physical Interpretation of the Angle-dependent Magnetic Helicity Spectrum in the Solar Wind: The Nature of Turbulent Fluctuations near the Proton Gyroradius Scale. ApJ, 785:138, April 2014.

[66] J. Šafránková, Z. Němeček, L. Přech, and G. N. Zastenker. Ion Kinetic Scale in the Solar Wind Observed. Phys. Rev. Lett., 110(2):025004, January 2013.

[67] F. Valentini, S. Servidio, D. Perrone, F. Califano, W. H. Matthaeus, and P. Veltri. Hybrid Vlasov-Maxwell simulations of two-dimensional turbulence in plasmas. Physics of Plasmas, 21(8):082307, August 2014.

[68] S. Servidio, K. T. Osman, F. Valentini, D. Perrone, F. Califano, S. Chapman, W. H. Matthaeus, and P. Veltri. Proton Kinetic Effects in Vlasov and Solar Wind Turbulence. ApJ, 781:L27, February 2014.

[69] C. T. Haynes, D. Burgess, and E. Camporeale. Reconnection and Electron Temperature Anisotropy in Sub-proton Scale Plasma Turbulence. ApJ, 783:38, March 2014.

[70] W. H. Matthaeus and S. L. Lamkin. Rapid magnetic reconnection caused by finite amplitude fluctuations. Phys.Fl., 28:303–307, January 1985.

[71] P. Veltri. MHD turbulence in the solar wind: self-similarity, intermittency and coherent structures. PPCF, 41:A787–A795, March 1999.

[72] A. Mangeney. Summary of Session 1: Fundamental Processes in Space Physics from Macroscopic to Microscopic Scales. Ap&SS, 277:117–122, June 2001.

[73] E. Priest and T. Forbes. Magnetic Reconnection. Cambridge Univ. Press, 2000., 2000.

[74] P. Dmitruk and W. H. Matthaeus. Structure of the electromagnetic field in three-dimensional Hall magnetohydrodynamic turbulence. Pl.Phys., 13(4):042307, April 2006.

[75] A. Greco, P. Chuychai, W. H. Matthaeus, S. Servidio, and P. Dmitruk. Intermittent MHD structures and classical discontinuities. Geophys. Res. Lett., 35:19111, October 2008.

[76] S. Servidio, A. Greco, W. H. Matthaeus, K. T. Osman, and P. Dmitruk. Statistical association of discontinuities and reconnection in magnetohydrodynamic turbulence. J. Geophys. Res., 116:9102, September 2011.

[77] J. Ambrosiano, W. H. Matthaeus, M. L. Goldstein, and D. Plante. Test particle accelera-

tion in turbulent reconnecting magnetic fields. J. Geophys. Res., 93:14383–14400, December 1988.

[78] P. Dmitruk and W. H. Matthaeus. Test particle acceleration in three-dimensional Hall MHD turbulence. J. Geophys. Res., 111:12110, December 2006.

[79] A. Lazarian and M. Opher. A model of acceleration of anomalous cosmic rays by reconnection in the heliosheath. ApJ, 703:8–21, September 2009.

[80] M. Hoshino. Stochastic Particle Acceleration in Multiple Magnetic Islands during Reconnection. Phys. Rev. Lett., 108(13):135003, March 2012.

[81] J. T. Gosling. Observations of magnetic reconnection in the turbulent high-speed solar wind. ApJ, 671:L73–L76, December 2007.

[82] A. C.-L. Chian and P. R. Muñoz. Detection of Current Sheets and Magnetic Reconnections at the Turbulent Leading Edge of an Interplanetary Coronal Mass Ejection. ApJ, 733:L34, June 2011.

[83] K. T. Osman, W. H. Matthaeus, J. T. Gosling, A. Greco, S. Servidio, B. Hnat, S. C. Chapman, and T. D. Phan. Magnetic Reconnection and Intermittent Turbulence in the Solar Wind. Physical Review Letters, 112(21):215002, May 2014.

[84] S. J. Schwartz and D. Burgess. Quasi-parallel shocks - A patchwork of three-dimensional structures. Geophys. Res. Lett., 18:373–376, March 1991.

[85] G. K. Parks, E. Lee, N. Lin, S. Y. Fu, M. McCarthy, J. B. Cao, J. Hong, Y. Liu, J. K. Shi, M. L. Goldstein, P. Canu, I. Dandouras, and H. Rème. Reinterpretation of Slowdown of Solar Wind Mean Velocity in Nonlinear Structures Observed Upstream of Earth's Bow Shock. ApJ, 771:L39, July 2013.

[86] R. A. Treumann. Fundamentals of collisionless shocks for astrophysical application, 1. Non-relativistic shocks. A&A Rev., 17:409–535, December 2009.

[87] M. Wan, W. H. Matthaeus, H. Karimabadi, V. Roytershteyn, M. Shay, P. Wu, W. Daughton, B. Loring, and S. C. Chapman. Intermittent Dissipation at Kinetic Scales in Collisionless Plasma Turbulence. Phys. Rev. Lett., 109(19):195001, November 2012.

[88] H. Hasegawa, M. Fujimoto, T.-D. Phan, H. Rème, A. Balogh, M. W. Dunlop, C. Hashimoto, and R. TanDokoro. Transport of solar wind into earth's magnetosphere through rolled-up kelvin-helmholtz vortices. Nature, 430:755–758, August 2004.

[89] D. Sundkvist, V. Krasnoselskikh, P. K. Shukla, A. Vaivads, M. André, S. Buchert, and H. Rème. In situ multi-satellite detection of coherent vortices as a manifestation of Alfvénic turbulence. Nature, 436:825–828, August 2005.

[90] O. Alexandrova, A. Mangeney, M. Maksimovic, N. Cornilleau-Wehrlin, J.-M. Bosqued, and M. André. Alfvén vortex filaments observed in magnetosheath downstream of a quasi-perpendicular bow shock. J. Geophys. Res., 111:12208, December 2006.

[91] D. Caprioli and A. Spitkovsky. Simulations of Ion Acceleration at Non-relativistic Shocks. I. Acceleration Efficiency. ApJ, 783:91, March 2014.

[92] P. Blasi. On the Equipartition of Thermal and Nonthermal Energy in Clusters of Galaxies. ApJ, 525:603–608, November 1999.

[93] A. G. Emslie, H. Kucharek, B. R. Dennis, N. Gopalswamy, G. D. Holman, G. H. Share, A. Vourlidas, T. G. Forbes, P. T. Gallagher, G. M. Mason, T. R. Metcalf, R. A. Mewaldt, R. J. Murphy, R. A. Schwartz, and T. H. Zurbuchen. Energy partition in two solar flare/CME events. J. Geophys. Res., 109:10104, October 2004.

[94] A. G. Emslie, B. R. Dennis, A. Y. Shih, P. C. Chamberlin, R. A. Mewaldt, C. S. Moore, G. H. Share, A. Vourlidas, and B. T. Welsch. Global Energetics of Thirty-eight Large Solar Eruptive Events. ApJ, 759:71, November 2012.

[95] J. D. Richardson, K. I. Paularena, A. J. Lazarus, and J. W. Belcher. Radial evolution of the solar wind from IMP 8 to Voyager 2. Geophys. Res. Lett., 22:325–328, February 1995.

[96] J. E. Borovsky and S. P. Gary. How important are the alpha-proton relative drift and the electron heat flux for the proton heating of the solar wind in the inner heliosphere? J. Geophys. Res., 119:5210–5219, July 2014.

[97] E. Marsch. Kinetic physics of the solar corona and solar wind. Living Reviews in Solar Physics, 3:1–+, July 2006.

[98] J. C. Kasper, A. J. Lazarus, and S. P. Gary. Hot Solar-Wind Helium: Direct Evidence for Local Heating by Alfvén-Cyclotron Dissipation. Phys. Rev. Lett., 101(26):261103, December 2008.

[99] D. Burgess, E. A. Lucek, M. Scholer, S. D. Bale, M. A. Balikhin, A. Balogh, T. S. Horbury, V. V. Krasnoselskikh, H. Kucharek, B. Lembège, E. Möbius, S. J. Schwartz, M. F. Thomsen, and S. N. Walker. Quasi-parallel Shock Structure and Processes. Space Sci. Rev., 118:205–222, June 2005.

[100] J. P. Eastwood, E. A. Lucek, C. Mazelle, K. Meziane, Y. Narita, J. Pickett, and R. A. Treumann. The Foreshock. Space Sci. Rev., 118:41–94, June 2005.

[101] E. A. Lucek, D. Constantinescu, M. L. Gold-

stein, J. Pickett, J. L. Pinçon, F. Sahraoui, R. A. Treumann, and S. N. Walker. The Magnetosheath. Space Sci. Rev., 118:95–152, June 2005.

[102] Y. Liu, J. D. Richardson, J. W. Belcher, and J. C. Kasper. Temperature Anisotropy in a Shocked Plasma: Mirror-Mode Instabilities in the Heliosheath. ApJ, 659:L65–L68, April 2007.

[103] J. A. Araneda, Y. Maneva, and E. Marsch. Preferential Heating and Acceleration of α Particles by Alfvén-Cyclotron Waves. Phys. Rev. Lett., 102(17):175001, May 2009.

[104] K. J. Bowers, B. J. Albright, L. Yin, W. Daughton, V. Roytershteyn, B. Bergen, and T. J. T. Kwan. Advances in petascale kinetic plasma simulation with VPIC and Roadrunner. Journal of Physics Conference Series, 180(1):012055, July 2009.

[105] Stefano Markidis, Giovanni Lapenta, and Rizwan-uddin. Multi-scale simulations of plasma with ipic3d. Mathematics and Computers in Simulation, 80(7):1509–1519, 2010.

[106] E. Sonnendrücker, J. Roche, P. Bertrand, and A. Ghizzo. The Semi-Lagrangian Method for the Numerical Resolution of the Vlasov Equation. Journal of Computational Physics, 149:201–220, March 1999.

[107] F. Valentini, P. Trávníček, F. Califano, P. Hellinger, and A. Mangeney. A hybrid-Vlasov model based on the current advance method for the simulation of collisionless magnetized plasma. Journal of Computational Physics, 225:753–770, July 2007.

[108] S. Bourouaine, D. Verscharen, B. D. G. Chandran, B. A. Maruca, and J. C. Kasper. Limits on Alpha Particle Temperature Anisotropy and Differential Flow from Kinetic Instabilities: Solar Wind Observations. ApJ, 777:L3, November 2013.

[109] B. D. G. Chandran, D. Verscharen, E. Quataert, J. C. Kasper, P. A. Isenberg, and S. Bourouaine. Stochastic Heating, Differential Flow, and the Alpha-to-proton Temperature Ratio in the Solar Wind. ApJ, 776:45, October 2013.

[110] Y. G. Maneva, A. F. ViñAs, and L. Ofman. Turbulent heating and acceleration of He^{++} ions by spectra of Alfvén-cyclotron waves in the expanding solar wind: 1.5-D hybrid simulations. J. Geophys. Res., 118:2842–2853, June 2013.

[111] X. Li and S. R. Habbal. Hybrid simulation of ion cyclotron resonance in the solar wind: Evolution of velocity distribution functions. J. Geophys. Res., 110:10109, October 2005.

[112] D. Telloni, E. Antonucci, and M. A. Dodero. Oxygen temperature anisotropy and solar wind heating above coronal holes out to 5 Rsun. A&A, 476:1341–1346, December 2007.

[113] E. A. Kronberg, R. Bučík, S. Haaland, B. Klecker, K. Keika, M. I. Desai, P. W. Daly, M. Yamauchi, R. Gómez-Herrero, and A. T. Y. Lui. On the origin of the energetic ion events measured upstream of the Earth's bow shock by STEREO, Cluster, and Geotail. J. Geophys. Res., 116:2210, February 2011.

[114] D. Perrone, F. Valentini, S. Servidio, S. Dalena, and P. Veltri. Vlasov Simulations of Multi-ion Plasma Turbulence in the Solar Wind. ApJ, 762:99, January 2013.

[115] D. Perrone, F. Valentini, S. Servidio, S. Dalena, and P. Veltri. Analysis of intermittent heating in a multi-component turbulent plasma. European Physical Journal D, 68:209, July 2014.

[116] I. H. Cairns and B. F. McMillan. Electron acceleration by lower hybrid waves in magnetic reconnection regions. Physics of Plasmas, 12(10):102110, October 2005.

[117] A. Afanasiev, R. Vainio, and L. Kocharov. The Effect of Stochastic Re-acceleration on the Energy Spectrum of Shock-accelerated Protons. ApJ, 790:36, July 2014.

[118] J. F. Drake, M. Swisdak, and R. Fermo. The Power-law Spectra of Energetic Particles during Multi-island Magnetic Reconnection. ApJ, 763:L5, January 2013.

[119] G. P. Zank, J. A. le Roux, G. M. Webb, A. Dosch, and O. Khabarova. Particle Acceleration via Reconnection Processes in the Supersonic Solar Wind. ApJ, 797:28, December 2014.

[120] A. R. Bell. The acceleration of cosmic rays in shock fronts. I. MNRAS, 182:147–156, January 1978.

[121] D. Caprioli, A.-R. Pop, and A. Spitkovsky. Simulations and Theory of Ion Injection at Non-relativistic Collisionless Shocks. ApJ, 798:L28, January 2015.

[122] J. W. Armstrong, B. J. Rickett, and S. R. Spangler. Electron density power spectrum in the local interstellar medium. ApJ, 443:209–221, April 1995.

[123] P. Hennebelle and E. Falgarone. Turbulent molecular clouds. A&A Rev., 20:55, November 2012.

[124] D. Falceta-Gonçalves, G. Kowal, E. Falgarone, and A. C.-L. Chian. Turbulence in the interstellar medium. Nonlinear Processes in Geophysics, 21:587–604, May 2014.

[125] I. Zhuravleva, E. Churazov, A. A. Schekochihin, S. W. Allen, P. Arévalo, A. C. Fabian, W. R. Forman, J. S. Sanders, A. Simionescu, R. Sunyaev, A. Vikhlinin, and N. Werner. Turbulent heating in galaxy clusters brightest in X-rays. Nature, 515:85–87, November 2014.

[126] E. Herbst. Chemistry in the Interstellar Medium. Annual Review of Physical

Chemistry, 46:27–54, October 1995.

[127] K. Joulain, E. Falgarone, G. Pineau des Forets, and D. Flower. Non-equilibrium chemistry in the dissipative structures of interstellar turbulence. A&A, 340:241–256, December 1998.

[128] S. R. Spangler and C. R. Gwinn. Evidence for an inner scale to the density turbulence in the interstellar medium. ApJ, 353:L29–L32, April 1990.

[129] A. Masters, N. Achilleos, M. G. Kivelson, N. Sergis, M. K. Dougherty, M. F. Thomsen, C. S. Arridge, S. M. Krimigis, H. J. McAndrews, S. J. Kanani, N. Krupp, and A. J. Coates. Cassini observations of a Kelvin-Helmholtz vortex in Saturn's outer magnetosphere. J. Geophys. Res., 115:7225, July 2010.

[130] J. Paral and R. Rankin. Dawn-dusk asymmetry in the Kelvin-Helmholtz instability at Mercury. Nature Communications, 4:1645, April 2013.

[131] S. N. Borovikov and N. V. Pogorelov. Voyager 1 near the Heliopause. ApJ, 783:L16, March 2014.

[132] T. V. Zaqarashvili, Z. Vörös, and I. Zhelyazkov. Kelvin-Helmholtz instability of twisted magnetic flux tubes in the solar wind. A&A, 561:A62, January 2014.

[133] T. V. Zaqarashvili, Z. Vörös, Y. Narita, and R. Bruno. Twisted Magnetic Flux Tubes in the Solar Wind. ApJ, 783:L19, March 2014.

[134] T. S. Horbury and J. M. Schmidt. Development and Effects of Turbulence in Connection with CIRs. Space Sci. Rev., 89:61–76, July 1999.

[135] J. E. Borovsky and M. H. Denton. Solar wind turbulence and shear: A superposed-epoch analysis of corotating interaction regions at 1 AU. J. Geophys. Res., 115:10101, October 2010.

[136] H. Hasegawa, A. Retinò, A. Vaivads, Y. Khotyaintsev, M. André, T. K. M. Nakamura, W.-L. Teh, B. U. Ö. Sonnerup, S. J. Schwartz, Y. Seki, M. Fujimoto, Y. Saito, H. Rème, and P. Canu. Kelvin-helmholtz waves at the earth's magnetopause: Multiscale development and associated reconnection. J. Geophys. Res., 114:12207–+, December 2009.

[137] C. Foullon, E. Verwichte, V. M. Nakariakov, K. Nykyri, and C. J. Farrugia. Magnetic Kelvin-Helmholtz Instability at the Sun. ApJ, 729:L8, March 2011.

[138] S. A. Balbus and J. F. Hawley. Instability, turbulence, and enhanced transport in accretion disks. Reviews of Modern Physics, 70:1–53, January 1998.

[139] D. Burgess and M. Scholer. Microphysics of Quasi-parallel Shocks in Collisionless Plasmas. Space Sci. Rev., 178:513–533, October 2013.

[140] H. Karimabadi, V. Roytershteyn, H. X. Vu, Y. A. Omelchenko, J. Scudder, W. Daughton, A. Dimmock, K. Nykyri, M. Wan, D. Sibeck, M. Tatineni, A. Majumdar, B. Loring, and B. Geveci. The link between shocks, turbulence, and magnetic reconnection in collisionless plasmas. Phys.Plasmas, 21(6):062308, June 2014.

[141] S. D. Bale, M. A. Balikhin, T. S. Horbury, V. V. Krasnoselskikh, H. Kucharek, E. Möbius, S. N. Walker, A. Balogh, D. Burgess, B. Lembège, E. A. Lucek, M. Scholer, S. J. Schwartz7 10, and M. F. Thomsen. Quasi-perpendicular shock structure and processes. Space Sci. Rev., 118:161–203, June 2005.

[142] E. A. Lucek, T. S. Horbury, I. Dandouras, and H. Rème. Cluster observations of the Earth's quasi-parallel bow shock. J. Geophys. Res., 113:7, June 2008.

[143] J. F. McKenzie and K. O. Westphal. Transmission of Alfvén waves through the Earth's bow shock. Planet. Space Sci., 17:1029–1037, May 1969.

[144] R. Vainio and R. Schlickeiser. Alfven wave transmission and particle acceleration in parallel shock waves. A&A, 331:793–799, March 1998.

[145] K. Meziane, M. Wilber, A. M. Hamza, C. Mazelle, G. K. Parks, H. RèMe, and E. A. Lucek. Evidence for a high-energy tail associated with foreshock field-aligned beams. J. Geophys. Res., 112:1101, January 2007.

[146] A. Masters, L. Stawarz, M. Fujimoto, S. J. Schwartz, N. Sergis, M. F. Thomsen, A. Retinò, H. Hasegawa, B. Zieger, G. R. Lewis, A. J. Coates, P. Canu, and M. K. Dougherty. Electron acceleration to relativistic energies at a strong quasi-parallel shock wave. Nature Physics, 9:164–167, March 2013.

[147] T. D. Phan, J. T. Gosling, M. S. Davis, R. M. Skoug, M. Øieroset, R. P. Lin, R. P. Lepping, D. J. McComas, C. W. Smith, H. Reme, and A. Balogh. A magnetic reconnection X-line extending more than 390 Earth radii in the solar wind. Nature, 439:175–178, January 2006.

[148] J. T. Gosling, S. Eriksson, D. J. McComas, T. D. Phan, and R. M. Skoug. Multiple magnetic reconnection sites associated with a coronal mass ejection in the solar wind. J. Geophys. Res., 112:8106–+, August 2007.

[149] T. D. Phan, J. T. Gosling, and M. S. Davis. Prevalence of extended reconnection x-lines in the solar wind at 1 au. Geophys. Res. Lett., 36:9108–+, May 2009.

[150] K. E. J. Huttunen, S. D. Bale, T. D. Phan, M. Davis, and J. T. Gosling. Wind/WAVES observations of high-frequency plasma waves in solar wind reconnection exhausts. J. Geophys. Res., 112:1102, January

2007.
[151] Z. Vörös, Y. L. Sasunov, V. S. Semenov, T. V. Zaqarashvili, R. Bruno, and M. Khodachenko. Reconnection Outflow Generated Turbulence in the Solar Wind. ApJ, 797:L10, December 2014.
[152] Y.-H. Liu, J. F. Drake, and M. Swisdak. The structure of the magnetic reconnection exhaust boundary. Phys.Plasmas, 19(2):022110, February 2012.
[153] S. D. Bale, M. J. Reiner, J.-L. Bougeret, M. L. Kaiser, S. Krucker, D. E. Larson, and R. P. Lin. The source region of an interplanetary type II radio burst. Geophys. Res. Lett., 26:1573–1576, June 1999.
[154] M. Pulupa and S. D. Bale. Structure on Interplanetary Shock Fronts: Type II Radio Burst Source Regions. ApJ, 676:1330–1337, April 2008.
[155] V. Sergeev, V. Angelopoulos, S. Apatenkov, J. Bonnell, R. Ergun, R. Nakamura, J. McFadden, D. Larson, and A. Runov. Kinetic structure of the sharp injection/dipolarization front in the flow-braking region. Geophys. Res. Lett., 36:21105–+, November 2009.
[156] Y. V. Khotyaintsev, C. M. Cully, A. Vaivads, M. André, and C. J. Owen. Plasma Jet Braking: Energy Dissipation and Nonadiabatic Electrons. Phys. Rev. Lett., 106(16):165001, April 2011.
[157] B. Zieger, A. Retinò, R. Nakamura, W. Baumjohann, A. Vaivads, and Y. Khotyaintsev. Jet front-driven mirror modes and shocklets in the near-Earth flow-braking region. Geophys. Res. Lett., 38:22103, November 2011.
[158] H. S. Fu, Y. V. Khotyaintsev, M. André, and A. Vaivads. Fermi and betatron acceleration of suprathermal electrons behind dipolarization fronts. Geophys. Res. Lett., 381:L16104, August 2011.
[159] V. Angelopoulos, A. Runov, X. Z. Zhou, D. L. Turner, S. A. Kiehas, S. S. Li, and I. Shinohara. Electromagnetic Energy Conversion at Reconnection Fronts. Science, 341(6153):1478–1482, September 2013.
[160] R. Bruno and V. Carbone. The solar wind as a turbulence laboratory. LivRevSolPhys, 2:4–+, September 2005.
[161] E. Quataert. Radiatively inefficient accretion flow models of sgr a*. Astron. Nachr., 324:435, 2003.
[162] L. A. Fisk and G. Gloeckler. Acceleration and Composition of Solar Wind Suprathermal Tails. Space Sci. Rev., 130:153–160, June 2007.
[163] D. Perrone, S. Bourouaine, F. Valentini, E. Marsch, and P. Veltri. Generation of temperature anisotropy for alpha particle velocity distributions in solar wind at 0.3 AU: Vlasov simulations and Helios observations. J. Geophys. Res., 119:2400–2410, April 2014.
[164] H. U. Auster, K. H. Glassmeier, W. Magnes, O. Aydogar, W. Baumjohann, D. Constantinescu, D. Fischer, K. H. Fornacon, E. Georgescu, P. Harvey, O. Hillenmaier, R. Kroth, M. Ludlam, Y. Narita, R. Nakamura, K. Okrafka, F. Plaschke, I. Richter, H. Schwarzl, B. Stoll, A. Valavanoglou, and M. Wiedemann. The THEMIS fluxgate magnetometer. Space Sci. Rev., 141:235–264, December 2008.
[165] J. Šafránková, Z. Němeček, L. Přech, G. Zastenker, I. Čermák, L. Chesalin, A. Komárek, J. Vaverka, M. Beránek, J. Pavlů, E. Gavrilova, B. Karimov, and A. Leibov. Fast Solar Wind Monitor (BMSW): Description and First Results. Space Sci. Rev., 175:165–182, June 2013.
[166] A. B. Galvin, L. M. Kistler, M. A. Popecki, C. J. Farrugia, K. D. C. Simunac, L. Ellis, E. Möbius, M. A. Lee, M. Boehm, J. Carroll, A. Crawshaw, M. Conti, P. Demaine, S. Ellis, J. A. Gaidos, J. Googins, M. Granoff, A. Gustafson, D. Heirtzler, B. King, U. Knauss, J. Levasseur, S. Longworth, K. Singer, S. Turco, P. Vachon, M. Vosbury, M. Widholm, L. M. Blush, R. Karrer, P. Bochsler, H. Daoudi, A. Etter, J. Fischer, J. Jost, A. Opitz, M. Sigrist, P. Wurz, B. Klecker, M. Ertl, E. Seidenschwang, R. F. Wimmer-Schweingruber, M. Koeten, B. Thompson, and D. Steinfeld. The Plasma and Suprathermal Ion Composition (PLASTIC) Investigation on the STEREO Observatories. Space Sci. Rev., 136:437–486, April 2008.
[167] H. Hasegawa, B. U. Ã.-. Sonnerup, M. Fujimoto, Y. Saito, and T. Mukai. Recovery of streamlines in the flank low-latitude boundary layer. J. Geophys. Res., 112:4213, April 2007.
[168] B. U. Ã.-. Sonnerup and W.-L. Teh. Reconstruction of two-dimensional coherent MHD structures in a space plasma: The theory. J. Geophys. Res., 113:5202, May 2008.
[169] W.-L. Teh, R. Nakamura, B. U. Ö. Sonnerup, J. P. Eastwood, M. Volwerk, A. N. Fazakerley, and W. Baumjohann. Evidence of the origin of the Hall magnetic field for reconnection: Hall MHD reconstruction results from Cluster observations. J. Geophys. Res., 116:11218, November 2011.
[170] C. Norgren, A. Vaivads, Y. V. Khotyaintsev, and M. André. Lower Hybrid Drift Waves: Space Observations. Phys. Rev. Lett., 109(5):055001, August 2012.
[171] M. Farge, Y. Guezennec, C. M. Ho, and C. Meneveau. Continuous wavelet analysis of coherent structures. In D. Spinks, ed-

itor, Studying Turbulence Using Numerical Simulation Databases. 3: Proceedings of the 1990 Summer Program, pages 331–348, December 1990.

[172] G. Paschmann and P. W. Daly. Analysis Methods for Multi-Spacecraft Data. ISSI Scientific Reports Series SR-001, ESA/ISSI, Vol. 1. ISBN 1608-280X, 1998. ISSI Scientific Reports Series, 1, 1998.

[173] G. Paschmann and P. W. Daly. Multi-Spacecraft Analysis Methods Revisited. February 2008.

[174] T. Dudok de Wit, O. Alexandrova, I. Furno, L. Sorriso-Valvo, and G. Zimbardo. Methods for Characterising Microphysical Processes in Plasmas. Space Sci. Rev., 178:665–693, October 2013.

A.2 Team members

Austria

IWF

Wolfgang Baumjohan
Mark Bentley
Maxim Khodachenko
Werner Magnes
Rumi Nakamura
Takuma Nakamura
Yasuhito Narita
Ferdinand Plaschke
Daniel Schmid
Martin Volwerk
Zoltan Vörös
Teimuraz Zaqarashvili

Belgium

Belgian Inst. for Space Aeron.

Johan De Keyser
Marius Echim
Hervé Lamy
Yuriy Voitenko

CPA, Katholieke Univ. Leuven

Gianni Lapenta
Yana Maneva

Canada

Univ. Alberta

Ian Mann

Univ. Calgary

Christopher Cully
Andrew Yau

Univ. New-Brunswick

Abdelhaq Hamza
Karim Meziane

China

Beihang Univ.

Huishan Fu

IGG/CAS

Aimin Du

Nanchang Univ.

Xiaohua Deng

NSSC/CAS

Xueshang Feng
Chao Shen

Peking Univ.

Qiugang Zong
Jiansen He

USTC

Quanming Lu

Czech Republic

ASI/CAS

Petr Hellinger

IAP/CAS

Jan Soucek
Ondrej Santolik
Benjamin Grison
Oksana Kruparova
Vratislav Krupar
Ivana Kolmasova

MFF, Charles Univ.

Zdenek Nemecek
Jana Safrankova Frantisek Nemec Lubomir Prech

Finland

FMI

Minna Palmroth
Natalia Ganushkina
Sebastian von Alfthan
Yann Kempf
Sanni Hoilijoki

Univ. Turku

Rami Vainio

France

LATMOS/IPSL/UVSQ/CNRS

Bertrand Lembege

LESIA/CNRS/Obs. Paris

Olga Alexandrova
Carine Briand
Milan Maksimovic
Denise Perrone
Arnauld Zaslavsky

LPC2E/CNRS, Univ. Orléans

Thierry Dudok de Wit
Pierre Henri
Vladimir Krasnosselskikh
Matthieu Kretzschmar
Jean-Louis Pinçon

LPP/CNRS/Ecole Polytechnique/UPMC

Nicolas Aunai
Gerard Belmont
Dominique Fontaine
Sebastien Galtier
Roland Grappin
Shiyong Huang
Khurom Kiyani
Catherine Krafft
Olivier Le Contel
Alessandro Retinò
Laurence Rezeau
Fouad Sahraoui
Philippe Savoini

Univ. de Nancy

Alain Ghizzo
Etienne Gravier
Daniele Del Sarto

IRAP/CNRS/Univ.P.Sabatier

Vincent Génot
Benoit Lavraud
Philippe Louarn
Christian Mazelle

Francois Rincon
Alexis Rouillard

Lab. Lagrange/CNRS Observatoire Côte d'Azur

Thierry Passot
Pierre-Louis Sulem

Germany

Max Planck Inst. f. Plasma Physics, Garching

Silvio Sergio Cerri
Daniel Told

Max Planck Inst. f. Solar System Research, Göttingen

Jörg Büchner
Markus Fränz
Stein Haaland
Elena Kronberg

IEAP, Univ. Kiel

Robert F. Wimmer-Schweingruber

Hungary

MTA CSFK GGI

Gabor Facsko
Arpad Kis

Italy

CNR-IPCF

Gaetano De Vita
Raffaele Marino
Luca Sorriso-Valvo

INAF-IAPS

Roberto Bruno
Giuseppe Consolini
Raffaella D'Amicis
Rossana De Marco
Monica Laurenza
Maria Federica Marcucci
Giuseppe Pallocchia

INGV

Antonio Vecchio

Univ. Calabria

Tommaso Alberti
Vincenco Carbone
Antonella Greco
Ersilia Leonardis
Fabio Lepreti
Francesco Malara
Giuseppina Nigro
Silvia Perri
Oreste Pezzi
Francesco Pucci
Leonardo Primavera
Sandra Savaglio
Sergio Servidio
Francesco Valentini
Christian Vasconez
Pierluigi Veltri
Gaetano Zimbardo

Univ. L'Aquila

Patrizia Francia
Massimo Vellante

Univ. Pisa

Francesco Califano

Japan

ISAS, JAXA

Hiroshi Hasegawa
Yoshifumi Saito
Iku Shinohara

Nagoya Univ.

Shinji Saito

Netherlands

CWI

Enrico Camporeale

Norway

Univ. Bergen

Kjellmar Oksavik

Poland

Card. Stefan Wyszynski Univ. Space Res. Centre

Wieslaw Macek
Hanna Rothkaehl
Marek Strumik

Russia

Space Res. Inst.

Elena Grigorenko
Anatoli Petrukovich

Sweden

Chalmers, Gothenburg

Tünde Fülöp

IRF, Uppsala

Mats André
Anders Eriksson
Daniel Graham
Yuri Khotyaintsev
Cecilia Norgren
Hermann Opgenoorth
Andris Vaivads
Jan-Erik Wahlund
Emilia Yordanova

IRF, Kiruna

Masatoshi Yamauchi

KTH, Sweden

Nickolay Ivchenko
Tomas Karlsson
Per-Arne Lindqvist
Stefano Markidis
Göran Marklund

NORDITA

Axel Brandenburg

Univ. Umeå

Maria Hamrin

Switzerland

EPFL

Ivo Furno
Paolo Ricci

UK

Imperial College London

Christopher M Carr
Christopher Chen
Jonathan Eastwood
Lorenzo Matteini
Steve Schwartz

MSSL

Dhiren Kataria
Chris Owen

QMUL

David Burgess

RAL

Yulia Bogdanova
Malcolm Dunlop
Mike Hapgood
Jackie Davies

Univ. Sheffield

Michael Balikhin
Keith Yearby
Simon Walker

Univ. Oxford

Alexander Schekochihin

Univ. Southampton

Lorenzo Trenchi

Univ. Warwick

Sandra Chapman
Kareem Osman

Ukraine

Main Astronomical Observatory, Kyiv

Vyacheslav Olshevsky

USA

Harvard-Smith. Center Astrophys.

Justin Kasper

Jet Prop. Lab.

Marco Velli

LANL

Takuma Nakamura

LASP

Stefan Eriksson
Karlheinz Trattner

NASA-GSFC

Melvyn L. Goldstein
Craig J. Pollock
Thomas E. Moore
Marilia Samara

NASA-GSFC/Catholic Univ. America

Glyn A. Collinson

NASA-GSFC/Univ. Maryland

Robert T. Wicks

Princeton Univ.

Damiano Caprioli

Princeton Plasma Phys. Lab.

Hantao Ji

SSL, Univ. California, Berkeley

Stuart Bale
John Bonnell
Christopher Chaston
David Sundkvist

Univ. California, LA

Vassilis Angelopoulos
Drew Turner
Frank Jenko

Univ. California, San Diego

Homa Karimabadi

Univ. Iowa

Gregory Howes

Univ. Maryland

Jason TenBarge

Univ. New Hamsphire

Lynn Kistler
Harald Kucharek

Univ. Wisconsin

Alexander Lazarian

Center Space Phys., Boston Univ.

Merav Opher
Bertalan Zieger

A.3 Letters of endorsement

Attached are Letters of Endorsement from all the national agencies contributing to the payload hardware.

Nation	LoE issue data
Austria	2015-01-09
Belgium	2015-01-12
Czech Republic	2015-01-13
CNES	2015-01-12
DLR	2015-01-12
Finland	2015-01-12
Italy	2014-12-22
NASA	2014-12-17
Poland	2015-01-14
Swedend	2015-01-08
UK	2014-12-16